

MAGNETIC PROPERTIES OF NANO-COMPOSITE PARTICLES

by

XIA XU

ALAN M. LANE COMMITTEE CHAIR

YUPING BAO

DAVID E. NIKLES

JOHN W. VAN ZEE

MARK L. WEAVER

TAKAO SUZUKI

A DISSERTATION

Submitted in partial fulfillment of the requirements
for the degree of Doctor of Philosophy
in the Department of Chemical and Biological Engineering
in the Graduate School of
The University of Alabama

TUSCALOOSA, ALABAMA

2015

Copyright Xia Xu 2015
ALL RIGHTS RESERVED

ABSTRACT

Chemical synthesis routes for hollow spherical $\text{BaFe}_{12}\text{O}_{19}$, hollow mesoporous spherical $\text{BaFe}_{12}\text{O}_{19}$, worm-shape $\text{BaFe}_{12}\text{O}_{19}$ and FeCo particles were developed. These structured particles have great potentials for the applications including magnetic recording medium, catalyst support, and energy storage. Magnetically exchange coupled hard/soft $\text{SrFe}_{12}\text{O}_{19}/\text{FeCo}$ and MnBi/FeCo composites were synthesized through a newly proposed process of magnetic self-assembly. These exchange coupled composites can be potentially used as rare-earth free permanent magnets.

Hollow spherical $\text{BaFe}_{12}\text{O}_{19}$ particles (shell thickness ~ 5 nm) were synthesized from ethylene glycol assisted spray pyrolysis. Hollow mesoporous spherical $\text{BaFe}_{12}\text{O}_{19}$ particles (shell thickness ~ 100 nm) were synthesized from ethanol assisted spray pyrolysis, followed by alkaline ethylene glycol etching at 185 °C. An $\alpha\text{-Fe}_2\text{O}_3$ and BaCO_3 nanoparticle mixture was synthesized with reverse microemulsion, followed by annealing at 900 °C for 2 hours to get worm-shape $\text{BaFe}_{12}\text{O}_{19}$ particles, which consisted of 3-7 stacked hexagonal plates. FeCo nanoparticles were synthesized by reducing FeCl_2 and CoCl_2 in diphenyl ether with n-butyllithium at 200 °C in an inert gas environment. The surfactant of oleic acid was used in the synthesis to make particles well dispersed in nonpolar solvents (such as hexane).

$\text{SrFe}_{12}\text{O}_{19}/\text{FeCo}$ core/shell particles were prepared through a magnetic self-assembly process. The as-synthesized soft FeCo nanoparticles were magnetically attracted by hard $\text{SrFe}_{12}\text{O}_{19}$ particles, forming a $\text{SrFe}_{12}\text{O}_{19}/\text{FeCo}$ core/shell structure. The magnetic self-assembly mechanism

was confirmed by applying alternating-current demagnetization to the core/shell particles, which resulted in a separation of $\text{SrFe}_{12}\text{O}_{19}$ and FeCo particles.

MnBi/FeCo composites were synthesized, and the exchange coupling between MnBi and FeCo phases was demonstrated by smooth magnetic hysteresis loop of MnBi/FeCo composites. The thermal stability of MnBi/FeCo composites was investigated by annealing at 250 °C for 2 hours in N_2 environment. The results showed that FeCo nanoparticles were sintered and agglomerated during the annealing, and exchange coupling between MnBi and FeCo was destroyed.

Future work was proposed in three aspects: chemical synthesis of MnBi particles; decreasing the particle size of MnBi particles and maintaining their stability; improving the thermal stability of MnBi/FeCo composites.

DEDICATION

This dissertation is dedicated to my family and friends who stood by me through this dissertation journey.

LIST OF ABBREVIATIONS AND SYMBOLS

BaM	Barium ferrite
EG	Ethylene glycol
TEM	Transmitting electron microscopy
SEM	Scanning electron microscopy
VSM	Vibrating sample magnetometry
XRD	X-ray diffraction
Mr	Remanent magnetization
Ms	Saturation magnetization
EDX	Energy dispersive X-ray spectrum
Hc	Covercivity
ΔM	Delta M
M_d	Normalized demagnetization remanence
M_r	Normalized isothermal magnetization remanence
H	Applied magnetic field
$(BH)_{max}$	Maximum energy products
SAED	Selected area electron diffraction
EDTA	Ethylene diamine tetra acetic acid
PEG	Polyethylene glycol
RE	Rare-earth
TM	Transition-metal

CTAB	Cetyltrimethyl ammonium bromide
T_c	Curie temperature
H_c	Intrinsic coercivity
M_{ex}	Magnetization of exchange coupled product
H_{ex}	Covercivity of exchange coupled product
K_h	Anisotropy constant of hard phase
K_s	Anisotropy constant of soft phase
f_h	Volume fraction of hard phase
f_s	Volume fraction of soft phase
M_s	Magnetization of soft phase
H_h	Covercivity of hard phase
H_s	Coercivity of soft phase
M_h	Magnetization of hard phase
n-BuLi	n-Butyllithium
BCC	Body centered cubic
AC	Alternating current
Oe	Oersted, unit of magnetic field strength in Gaussian units
MRI	Magnetic resonance imaging
LTP	Low temperature phase

ACKNOWLEDGEMENTS

First of all, I would like to thank my advisor, Dr. Alan M. Lane, for bringing me to his group. His patient guidance and continuous encouragement make me produce new ideas and broaden my horizons. The numerous discussions with him help me solve research problems and walk to the end of this dissertation. His wisdom also helps me deal with puzzles in life. He is not only an advisor of my research, but also a friend and mentor of my life and future career.

I would also like to thank all of my committee members, Dr. Yuping Bao, Dr. David E. Nikles, Dr. John W. Wan Zee, Dr. Mark L. Weaver and Dr. Takao Suzuki, for their inspiring questions and invaluable suggestions for my academic research and dissertation.

Thanks extend to all members of Magnetic Materials and Devices Laboratory (MMDL): Dr. Yang-Ki Hong (director), Mr. Jaejin Lee, Mr. Jihoon Park, Mr. Woncheol Lee and Mr. Gatlin LaRochello, for their help on my research. Especially, I would like to appreciate Dr. Yang-Ki Hong for his tremendous guidance on my research, and Mr. Jihoon Park who stands with me for both happy and tough time in past three years.

I thank the members of Central Analytical Facility (CAF) of the University of Alabama: Mr. Johnny Goodwin, Mr. Rich Marten and Mr. Robot Holler, for their assistance on the training and usage of XRD, TEM and SEM. I am also deeply in debt to my family and friends, who give me tremendous love, encouragement and support.

The list is endless and I am expressing my appreciation to all of those who helped me in any respect during my research in past four years.

Lastly, I would like to thank funding agency of Advanced Research Projects Agency-Energy (ARPA-E), and the leadership of Pacific Northwest National Laboratory (PNNL) in this project.

CONTENTS

ABSTRACT.....	ii
DEDICATION.....	iv
LIST OF ABBREVIATIONS AND SYMBOLS.....	v
ACKNOWLEDGEMENTS.....	vii
LIST OF TABLES.....	xiii
LIST OF FIGURES.....	xiv
CHAPTER 1 INTRODUCTION.....	1
1.1. Classification of Magnetism.....	1
1.1.1. Diamagnetism.....	2
1.1.2. Paramagnetism.....	2
1.1.3. Ferromagnetism.....	3
1.1.4. Antiferromagnetism.....	3
1.1.5. Ferrimagnetism.....	3
1.2. Ferromagnetic Materials.....	3
1.2.1. Soft magnetic materials.....	4
1.2.2. Hard magnetic materials.....	5
1.3. Magnetic Exchange Coupling.....	7
1.3.1. Theory of magnetic exchange coupling.....	8
1.3.2. Experimental development of exchange coupling.....	11
1.3.3. Synthesis challenges of exchange coupled magnet.....	14
1.4. References.....	19

CHAPTER 2 EXPERIMENTAL.....	23
2.1. Chemical Synthesis Methods.....	23
2.1.1. Reduction of metal-containing compounds	23
2.1.2. Solid state synthesis	23
2.1.3. Spray pyrolysis.....	24
2.1.4. Reverse microemulsion.....	24
2.2. Characterization Techniques.....	25
2.2.1. X-ray Diffraction (XRD)	25
2.2.2. Scanning Electron Microscopy (SEM)	26
2.2.3. Transmission Electron Microscopy (TEM)	27
2.2.4. Vibrating Sample Magnetometry (VSM)	28
2.3. References.....	29
CHAPTER 3 HARD MAGNETIC NANOPARTICLES	32
3.1. Synthesis and Characterization of Hollow Mesoporous BaFe ₁₂ O ₁₉ Spheres.....	32
3.1.1. Introduction.....	32
3.1.2. Experimental	33
3.1.3. Results and discussion	35
3.1.4. Conclusions.....	41
3.2. EG Assisted Spray Pyrolysis for the Synthesis of Hollow BaFe ₁₂ O ₁₉ Spheres	41
3.2.1. Introduction.....	41
3.2.2. Experimental	42
3.2.3. Results and discussion	43
3.2.4. Conclusions.....	47
3.3. Synthesis and Characterization of Worm-shape BaFe ₁₂ O ₁₉ Nanoparticles	47
3.3.1. Introduction.....	47

3.3.2.	Experimental	48
3.3.3.	Results and discussion	49
3.3.4.	Conclusions	52
3.4.	References	52
CHAPTER 4 FeCo NANOPARTICLES		58
4.1.	Introduction	58
4.2.	Experimental	59
4.3.	Results and discussion	60
4.4.	Conclusions	62
4.5.	References	62
CHAPTER 5 SrFe ₁₂ O ₁₉ /FeCo CORE/SHELL PARTICLES		64
5.1.	SrFe ₁₂ O ₁₉ /pSiO ₂ /Co Particles	64
5.1.1.	Introduction	64
5.1.2.	Experimental	65
5.1.3.	Results and discussion	66
5.1.4.	Conclusions	70
5.2.	SrFe ₁₂ O ₁₉ /FeCo Core/shell Particles	70
5.2.1.	Introduction	70
5.2.2.	Experimental	71
5.2.3.	Results and discussion	71
5.2.4.	Conclusions	85
5.3.	References	86
CHAPTER 6 MnBi/FeCo COMPOSITES		90
6.1.	MnBi/FeCo Composites	90
6.1.1.	Introduction	90

6.1.2.	Experimental	91
6.1.3.	Results and discussion	91
6.1.4.	Conclusions	99
6.2.	Thermal Stability of MnBi/FeCo Composites	99
6.2.1.	Introduction	99
6.2.2.	Experimental	100
6.2.3.	Results and discussion	100
6.2.4.	Conclusions	104
6.3.	References	105
CHAPTER 7 UNDERSTANDING OF EXCHANGE COUPLING		107
7.1.	Introduction	107
7.2.	Experimental	108
7.3.	Results and discussion	109
7.4.	Conclusions	112
7.5.	References	112
CHAPTER 8 CONCLUSIONS AND FUTURE WORK		114
8.1.	Conclusions	114
8.2.	Future work	115
8.3.	References	117
APPENDIX I: ΔM Calculation		118
APPENDIX II: The Composition of FeCo Nanoparticles		119
APPENDIX III: The Prediction of the Size of Superparamagnetic FeCo Nanoparticles		121
APPENDIX IV: The Prediction of the Size of Superparamagnetic SrFe ₁₂ O ₁₉ and BaFe ₁₂ O ₁₉ Nanoparticles		122
APPENDIX V: The Repeatability of Experiments		123
APPENDIX VI: List of Publications and Patents		124

LIST OF TABLES

Table 5.1 Four concentrations of Fe and Co precursors in synthesis of SrM/FeCo core/shell nanoparticles.	79
---	----

LIST OF FIGURES

Figure 1.1 Magnetization curves and spin configurations of diamagnetism, paramagnetism and antiferromagnetism.	2
Figure 1.2 Magnetization curves and spin configurations of ferromagnetism and ferrimagnetism.	2
Figure 1.3 A typical magnetic hysteresis loop of soft magnetic materials.	4
Figure 1.4 A typical magnetic hysteresis loop of hard magnetic materials.	6
Figure 1.5 Development in the energy product $(BH)_{max}$ at room temperature of hard magnetic materials (each magnet is designed so that at a reference point 5 mm from the surface of the pole, a field of 100 mT is produced) [12].	7
Figure 1.6 Schematic of hysteresis loops of the exchange-coupled magnets [17].	8
Figure 1.7 Nucleation fields of soft magnetic spherical inclusions in a hard matrix [19].	10
Figure 1.8 Magnetic hysteresis loops for NdFeB single phase and NdFeB/nano-Fe composite powders synthesized by two processes and tuning the concentrations of metal ions, where A and B indicate the process of adding FeSO ₄ solution to NaBH ₄ solution with NdFeB powders and adding NaBH ₄ solution to FeSO ₄ solutions with NdFeB powders, respectively [27].	12
Figure 1.9 Room temperature magnetic hysteresis loops of nanocrystalline SmCo ₅ and SmCo ₅ /Fe nanocomposites [29].	12
Figure 1.10 (a) Dark field TEM image of SmCo ₅ /Fe nanocomposites (inset: SAED of the nanocomposites); (b) HRTEM image of a single aggregate of the SmCo ₅ /Fe nanocomposites with the dashed lines circling the nanocrystalline grains of either SmCo ₅ or Fe [30].	13
Figure 1.11 A typical HRTEM image for a sintered FePt–Fe ₃ Pt particle. The FePt and Fe ₃ Pt phases exist as different domains within the particle, with each domain having a dimension of about 5 nm, showing a modulated FePt–Fe ₃ Pt spatial distribution [31].	14
Figure 1.12 (a) Bright field TEM image of Sm ₂ Co ₇ + 40 wt% Fe ₆₅ Co ₃₅ and EFTEM elemental mapping for the same areas showing the distribution of (b) Sm, (c) Fe and (d) Co [35].	15
Figure 1.13 Schematic illustration of Frank-van der Merwe mode [42].	16
Figure 1.14 Schematic illustration of Volmer-Weber mode [42].	17
Figure 1.15 Schematic illustration of Stranski-Krastanov mode [42].	17

Figure 1.16 The relationship between volume percentage of soft phase (f_h) and magnetization and coercivity of exchange coupled composites in an exchange coupling system.....	18
Figure 1.17 Co shell-thickness-dependent M_s and H_c for the FePt/Co core/shell nanoparticles [40].....	18
Figure 2.1 Schematic of spray pyrolysis system.....	24
Figure 2.2 Reverse micelles in a microemulsion [14].	25
Figure 2.3 Bragg's law [16].....	26
Figure 2.4 Schematic of Scanning Electron Microscope (SEM) system [17].	27
Figure 2.5 Schematic of Transmission Electron Microscope (TEM) system [19].	28
Figure 2.6 Schematic of Vibrating Sample Magnetometer (VSM) system [20].	29
Figure 3.1 The reaction system of spray pyrolysis.	34
Figure 3.2 SEM and TEM images: (a) SEM image of as-synthesized hollow $BaFe_{12}O_{19}$ particles (inset: a broken hollow structured particle); (b) SEM image of hollow mesoporous $BaFe_{12}O_{19}$ particles; (c) TEM image of as-synthesized hollow $BaFe_{12}O_{19}$ particles; (d) TEM image of hollow mesoporous $BaFe_{12}O_{19}$ particles.	36
Figure 3.3 (a) High resolution TEM of hollow mesoporous $BaFe_{12}O_{19}$ spheres; (b) SAED pattern of hollow mesoporous $BaFe_{12}O_{19}$ spheres	37
Figure 3.4 Magnetic properties characterization: (a) Magnetic hysteresis loop of as-synthesized hollow $BaFe_{12}O_{19}$ particles (before etching); (b) magnetic hysteresis loop of hollow mesoporous $BaFe_{12}O_{19}$ particles (after etching).....	38
Figure 3.5 Powder XRD patterns. (a) XRD patterns of as-synthesized hollow $BaFe_{12}O_{19}$ particles (before etching); (b) XRD patterns of hollow mesoporous $BaFe_{12}O_{19}$ particles (after etching). ..	39
Figure 3.6 The size and size distribution of crystalline in hollow mesoporous BaM spheres.....	39
Figure 3.7 The step-by-step EG etching process on an individual hollow BaM sphere: (a) 0 min etching; (b) 5 min etching; (c) 7 min etching; (d) a schematic of step etching.....	40
Figure 3.8 TEM images of hollow $BaFe_{12}O_{19}$ spheres. (a), (b), (c): synthesized from 10 vol% EG; (d), (e), (f): synthesized from 20 vol% EG; (g), (h), (i): synthesized from 30 vol% EG.....	44
Figure 3.9 X-ray diffraction patterns of hollow $BaFe_{12}O_{19}$ spheres synthesized from different concentrations of EG.....	45
Figure 3.10 Magnetic hysteresis loops of hollow $BaFe_{12}O_{19}$ spheres synthesized from different concentration of EG.	46

Figure 3.11 SEM images (a, b, c) and their corresponding carbon EDX spectroscopy (d, e and f) of hollow BaFe ₁₂ O ₁₉ spheres synthesized from 10 vol%, 20 vol% and 30 vol% EG.....	47
Figure 3.12 Preparation procedures for worm-shape BaM particles by reverse microemulsion technique.....	49
Figure 3.13 TEM images of worm-shape BaM nanoparticles: (a) low magnification; (b) high magnification.	50
Figure 3.14 Proposed self-assembly process for the formation of worm-shape BaM nanoparticles.	50
Figure 3.15 X-ray diffraction patterns of worm-shape BaM nanoparticles.....	51
Figure 3.16 Magnetic hysteresis loop of worm-shape BaM nanoparticles.....	51
Figure 4.1 (a) TEM image and (b) Particle size distribution, of FeCo nanoparticles.....	61
Figure 4.2 Magnetic hysteresis loop of FeCo nanoparticles.....	61
Figure 4.3 Power XRD patterns of FeCo nanoparticles.	62
Figure 5.1 TEM of particle surface: (a) S-SrFe ₁₂ O ₁₉ particle; (b) S-SrFe ₁₂ O ₁₉ /SiO ₂ particle; (c) S-SrFe ₁₂ O ₁₉ /pSiO ₂ particle; (d) S-SrFe ₁₂ O ₁₉ /SiO ₂ /Co particle.....	67
Figure 5.2 A schematic of PVP protected SiO ₂ surface etching [19].	68
Figure 5.3 A schematic of SiO ₂ surface decoration of PEI and Co ²⁺ ions and Co ²⁺ reduction.	68
Figure 5.4 The VSM loops of S-SrM, S-SrM/pSiO ₂ and S-SrM/pSiO ₂ /Co particles.....	69
Figure 5.5 The XRD patterns of S-SrM, S-SrM/pSiO ₂ core/shell and S-SrM/pSiO ₂ /Co core/shell/shell particles.....	69
Figure 5.6 TEM images of SrM and SrM/FeCo core/shell and FeCo particle: (a) as-prepared SrM particle; (b) SrM/FeCo core/shell particle; (c) SrM particle (after demagnetization of core/shell particles); (d) FeCo nanoclusters (after demagnetization of core/shell particles).	73
Figure 5.7 TEM image of SrM/FeCo core/shell nanoparticle.	73
Figure 5.8 Tilt-angle TEM images. (a) $\theta = 0^\circ$. (b) $\theta = 30^\circ$. (c) $\theta = 60^\circ$	74
Figure 5.9 The line scan of energy dispersive X-ray (EDX) spectrometry for SrM/FeCo core/shell particles: (a) Scanning transmission electron microscopy (STEM) image (the line shows the scanning area, and the square is located to prevent electron beam shifting); (b) Elemental analysis for the EDX line scan.....	74
Figure 5.10 The schematic of the formation process of SrFe ₁₂ O ₁₉ /FeCo core/shell nanoparticles by magnetic self-assembly.....	75

Figure 5.11 Powder X-ray diffraction patterns of SrM core and SrM/FeCo core/shell particles: (a) XRD pattern of SrM particles; (b) XRD pattern of SrM/FeCo core/shell particles.	76
Figure 5.12 (a) M-H curves and (b) B-H curves of SrM core and SrM/FeCo core/shell particles.	77
Figure 5.13 TEM images of (a) SrM/FeCo core/shell particles; (b) SrM/FeCo/SiO ₂ core/shell/shell nanoparticles.	78
Figure 5.14 (a) The VSM loops of SrM, SrM/FeCo core/shell and SrM/FeCo/SiO ₂ core/shell/shell particles; (b) The XRD patterns of SrM/FeCo and SrM/FeCo/SiO ₂ particles.....	78
Figure 5.15 (a) the VSM loops of SrM/FeCo core/shell particles in as-prepared state and exposed in air for 2 hours; (b) the VSM loops of SrM/FeCo/SiO ₂ core/shell/shell particles in as-prepared state and exposed in air for 2 hours.	79
Figure 5.16 The TEM images of SrM/FeCo core/shell particles with different concentration of FeCo precursors: (1) FeCl ₂ ·4H ₂ O: 0.5 mmol, CoCl ₂ ·6H ₂ O: 0.25 mmol; (2) FeCl ₂ ·4H ₂ O: 1 mmol, CoCl ₂ ·6H ₂ O: 0.5 mmol; (3) FeCl ₂ ·4H ₂ O: 1.5 mmol, CoCl ₂ ·6H ₂ O: 0.75 mmol; (4) FeCl ₂ ·4H ₂ O: 2 mmol, CoCl ₂ ·6H ₂ O: 1 mmol.	80
Figure 5.17 The VSM loops of SrM particles and SrM/FeCo core/shell particles with different concentrations of Fe and Co precursors.	81
Figure 5.18 The XRD patterns of SrM/FeCo core/shell particles with different concentration of FeCo precursors.	82
Figure 5.19 FeCo nanoparticles: (a) VSM loop, inset: XRD patterns; (b) TEM image.	83
Figure 5.20 (a) the VSM loops of SrM particles, SrM/FeCo core/shell particles and SrM/FeCo particles mixture; (b) derivative curve of SrM/FeCo core/shell particles and SrM/FeCo particles mixture.	84
Figure 5.21 TEM image of SrFe ₁₂ O ₁₉ /FeCo nanoparticle mixture.	85
Figure 6.1 XRD patterns of as-received MnBi particles.	92
Figure 6.2 SEM images of (a) as received MnBi; (b) 5 min; (c) 7 min; (d) and 10 min grinding of the MnBi particles.	93
Figure 6.3 Magnetic hysteresis loops of as-received MnBi, 5 min ground MnBi, 7 min ground MnBi and 10 min ground MnBi particles. These particles were aligned in a 16 kOe magnetic field before VSM characterization.	93
Figure 6.4 Hysteresis loop of the FeCo nanoparticles. The top inset shows TEM image, and bottom inset shows XRD patterns.	94
Figure 6.5 (a) M-H curves and (b) B-H curves of MnBi particles and MnBi/FeCo (95/5 wt% and 90/10 wt%) composites.	95

Figure 6.6 ΔM curves of MnBi particles and MnBi/FeCo (95/5 wt% and 90/10 wt%) composites.....	96
Figure 6.7 Powder XRD patterns of MnBi particles and MnBi/FeCo(95/5 wt% and 90/10 wt%) composites.....	96
Figure 6.8 (a) SEM and (b) TEM images, and elemental mappings of (c) Bi, (d) Mn, (e) Co and (f) Fe for MnBi/FeCo (95/5 wt%) composites.....	98
Figure 6.9 Virgin curves of MnBi particles and MnBi/FeCo (95/5 wt%) composites.	99
Figure 6.10 TEM images of FeCo nanoparticles: (a) As synthesized; (b) Annealed at 250 °C for 2 hours.....	101
Figure 6.11 Powder XRD patterns of FeCo nanoparticles: (a) as synthesized; (b) annealed at 250 °C for 2 hours.	101
Figure 6.12 Magnetic hysteresis loops of FeCo nanoparticles: (a) as synthesized; (b) annealed at 250 °C for 2 hours.	102
Figure 6.13 TEM images of MnBi/FeCo composites: (a) as synthesized; (b) annealed at 250 °C for 2 hours.	103
Figure 6.14 Powder XRD patterns of MnBi/FeCo composites: (a) as-synthesized; (b) annealed at 250 °C for 2 hours.	103
Figure 6.15 Magnetic hysteresis loops of MnBi/FeCo composites: (a) as-synthesized; (b) annealed at 250 °C for 2 hours.	104
Figure 7.1 Magnetic hysteresis loop of as-synthesized FeCo particles. Inset: TEM image of FeCo particles.	109
Figure 7.2 The magnetic hysteresis loop of MnBi particles, FeCo particles and Composite A. Inset: VSM sample of Composite A.	110
Figure 7.3 The magnetic hysteresis loop of MnBi particles, FeCo particles and Composite B. .	111
Figure 7.4 Derive curves of magnetic hysterics loops in Fig. 7.2.	111
Figure 7.5 Derive curves of magnetic hysterics loops in Fig. 7.3.	111
Appendix Figure 1. Normalized demagnetization remanence (M_d) and isothermal magnetization remanence (M_r) curves of MnBi/FeCo: 95/5 wt% composites.....	118
Appendix Figure 2. ΔM curve of of MnBi/FeCo: 95/5 wt% composites.	118
Appendix Figure 3. Power XRD patterns of Fe-Co nanoparticles in Fig. 4.3.....	119
Appendix Figure 4. Fe-Co ally lattice constant [1].....	120

CHAPTER 1 INTRODUCTION

Rare-earth permanent magnets have been widely used for both power generation and consumption in modern society. However, rare-earth elements have limited accessibility, relatively high cost, and serious environmental pollutions in the extraction processes. In response to these issues, this dissertation research focuses on magnetic exchange coupling between magnetically hard and soft phases, which makes use of high magnetization of magnetically soft phase and high coercivity of magnetically hard phase. Specifically, M-type hexagonal strontium ferrite ($\text{SrFe}_{12}\text{O}_{19}$) and manganese bismuth alloy (Mn-Bi) are used as magnetically hard phases, and iron cobalt alloy (Fe-Co) is used as magnetically soft phase. When the two magnetic phases materials are well distributed at nano scale and exchange coupled, the maximum energy product ($(BH)_{max}$) of the composites can be improved from the single hard phase. To make the concept and process clearer, this part will give a brief introduction about magnetic materials (both hard and soft) and exchange coupling.

1.1. Classification of Magnetism

Magnetism originates from the orbital and spin motions of electrons, and the interactions among electrons. Scientifically, all of the materials can be defined as magnetic materials, and the difference is that some materials behavior more magnetically than others. Based on the specific magnetic behaviors, magnetism can be classified into diamagnetism, paramagnetism, ferromagnetism, antiferromagnetism, and ferrimagnetism [1]. The corresponding magnetization curves and spin configurations are shown in Fig. 1.1 and Fig. 1.2.

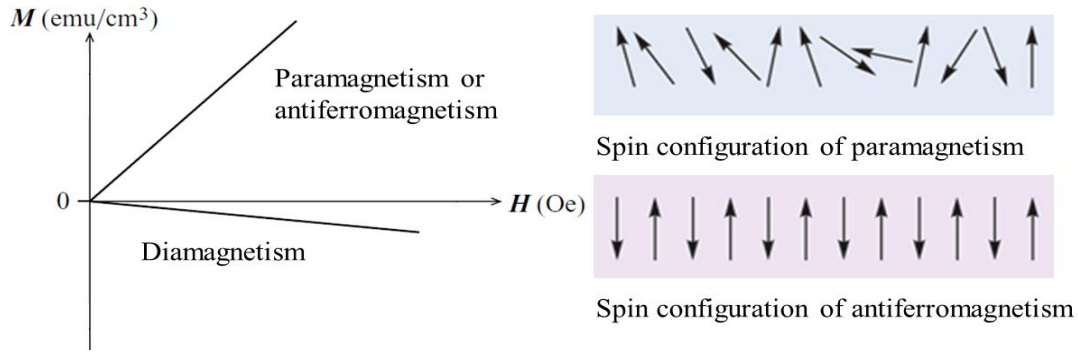


Figure 1.1 Magnetization curves and spin configurations of diamagnetism, paramagnetism and antiferromagnetism.

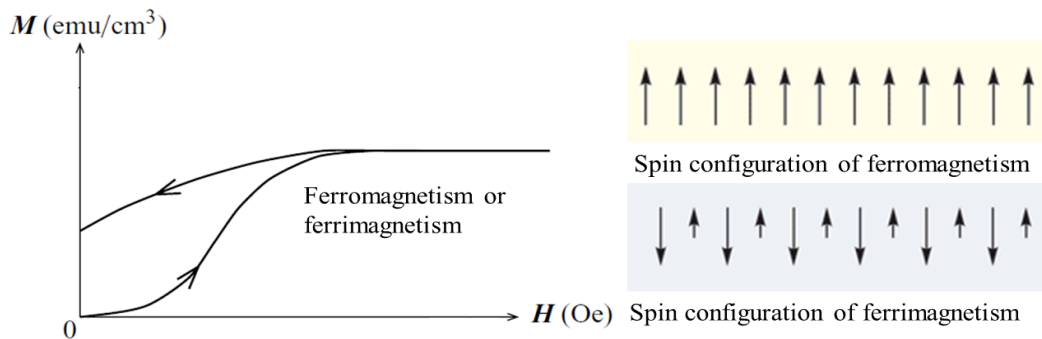


Figure 1.2 Magnetization curves and spin configurations of ferromagnetism and ferrimagnetism.

1.1.1. Diamagnetism

Diamagnetism is a basic property of all materials. It is due to the non-cooperative behavior of orbiting electrons when materials are exposed to an external applied magnetic field. In these materials, all the orbital shells are filled without unpaired electrons. Therefore, the net magnetic moment is zero at zero applied field. If exposed to an external field, the field on a single electron orbit is to reduce the effective current of the orbit, resulting in a magnetic moment opposing the applied field, as shown in Fig. 1.1.

1.1.2. Paramagnetism

Paramagnetism originates from unpaired electrons in partially filled orbitals and produces a net magnetic moment. The individual spin does not behavior magnetically without an applied

field. However, in the presence of an applied field, the atomic magnetic moments are partially aligned along the direction of the field, and produce positive magnetization, as shown in Fig. 1.1.

1.1.3. Ferromagnetism

Ferromagnetism originates from strong atomic moment interactions inside the materials. These interactions are produced from electronic exchange forces, and lead to an antiparallel or parallel alignment of atomic moments. Ferromagnetic materials usually show a large net magnetization even without an applied magnetic field, as shown in Fig. 1.2. The elements of Fe, Ni, Co and their alloys are typical ferromagnetic materials.

1.1.4. Antiferromagnetism

Different from ferromagnetism that all of the spin moments are aligned towards one direction, the spin moment alignment of neighboring atoms is in opposite directions in antiferromagnetism. The opposite magnetic moment direction cancels with each other, and results in a zero magnetization, as shown in Fig. 1.1. Some typical examples are iron oxide (FeO) and manganese sulfide (MnS).

1.1.5. Ferrimagnetism

In ferromagnetic materials, the magnetic moment direction of adjacent atoms is in antiparallel, the net magnetic moment can not be cancelled, as the magnitude of magnetic moments from adjacent atoms is different, as shown in Fig. 1.2.

1.2. Ferromagnetic Materials

Most of magnetic materials with industrial and academic interests are ferromagnetic materials. Based on different coercivity of ferromagnetic materials, two categories can be defined. One is soft magnetic materials with low coercivity and the other is hard magnetic materials with high coercivity.

1.2.1. Soft magnetic materials

Soft magnetic materials can be easily magnetized and demagnetized by a low magnetic field. When an applied field is removed, soft magnetic materials will return to a state of relatively low residual magnetization. Soft magnetic materials are used primarily to enhance or channel the flux produced by an electric current. The main parameter, which is often used as a figure of merit for soft magnetic materials, is the relative permeability, which shows how fast the material responds to an applied magnetic field. The other main parameters of interest also include coercivity, saturation magnetization and electrical conductivity. Typical soft materials have very low intrinsic coercivity (H_c) (usually less than 1000 Oe), high saturation magnetization (M_s) and low ramanent magnetization (M_r), as shown in Fig. 1.3. The highest magnetization of soft material discovered so far is iron cobalt alloy with molar ratio of 65 to 35 ($\text{Fe}_{65}\text{Co}_{35}$), and the theoretical magnetization can be as high as 242 emu/g [1].

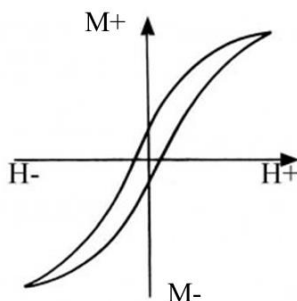


Figure 1.3 A typical magnetic hysteresis loop of soft magnetic materials.

Soft magnetic materials, especially nanoparticles, are widely used for the application of catalysis, biotechnology and drug delivery [2,3]. To recycle catalysts from liquid-phase reaction with magnetic separation is much more effective than filtration or centrifugation, especially when the catalysts are in the size range of sub-micron to nano meters. Ge et al. synthesized $\text{Fe}_3\text{O}_4/\text{Au}$ core/shell catalyst for liquid-phase reduction of 4-nitrophenol (4-NP) by NaBH_4 reduc-

tion [4]. Due to the high magnetization of Fe_3O_4 , the Au catalysts are easily recycled by magnetic separation after the reaction.

In biotechnology and biomedicine, the capture of specific proteins or biomolecules can be more efficient by using magnetic separation. Most soft magnetic nanoparticles used for these applications are in nano size with superparamagnetism, which means they show magnetic behaviors with external magnetic field, and can be immediately redispersed as soon as the magnetic field is removed [5]. Xu et al. used dopamine grafted iron oxide nanoparticles for protein separation [6]. Another promising application of soft magnetic nanoparticles is used as drug carrier for drug delivery, which was proposed in 1970s by Widder and his coworkers [7]. The magnetic drug carriers can potentially carry a large dose of drug to a specific area, achieving large local concentration and avoiding toxicity or other side effects to other organisms [8]. The application of soft magnetic nanoparticles in biotechnology can also be extended to hyperthermia treatment, which can be potentially used for cancer therapy besides chemotherapy, radiotherapy and surgery [9]. The mechanism of using magnetic induction hyperthermia is that when magnetic nanoparticles are exposed to a varying magnetic field, heat can be produced because of hysteresis loss, Brown-relaxation and Neel-relaxation [10].

1.2.2. Hard magnetic materials

Hard magnets, also called permanent magnets, are magnetic materials that can retain their magnetization after removing the external magnetic field. The term “hard” is used to describe the materials persisting sufficiently high resistance to resist demagnetization field. Coercivity is an important parameter to distinguish hard magnetic materials from and soft ones. Usually, the magnetic materials with H_c higher than 1000 Oe are called hard magnetic materials. As shown in

Fig. 1.4, hard magnetic materials have a high H_c , relatively high M_r and M_s . Such materials usually have large $(BH)_{max}$, which is the figure of merit of permanent magnet.

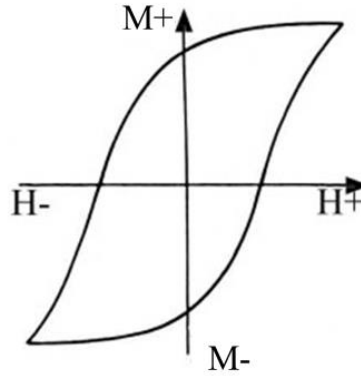


Figure 1.4 A typical magnetic hysteresis loop of hard magnetic materials.

In the past century, several important permanent magnets were discovered, and the techniques for large scale magnets manufacture were also established [11]. The $(BH)_{max}$ has been enhanced, from around 1 MGOe on steels discovered in the early 20th century, to around 3 MGOe on hexagonal ferrites in the middle of 20th century, and finally to around 57 MGOe on neodymium iron boron magnets (Nd-Fe-B) nowadays. The historical evolution of permanent magnetic materials is shown in Fig. 1.5 [12]. The great development of permanent magnets in the second half of the 20th century is attributed to application of rare earth elements (mainly Nd and Sm).

The most famous high performance permanent magnets at present are based on rare-earth (RE) and transition-metal (TM) intermetallic (Fe–Nd–B, Co–Sm) [13]. In RE-TM intermetallic, the high saturation magnetization and Curie temperature of the TM metals (Fe and Co) are combined with the high anisotropy constant of the RE metals (Nd, Pr and Sm) to provide large $(BH)_{max}$ value of the magnets [13].

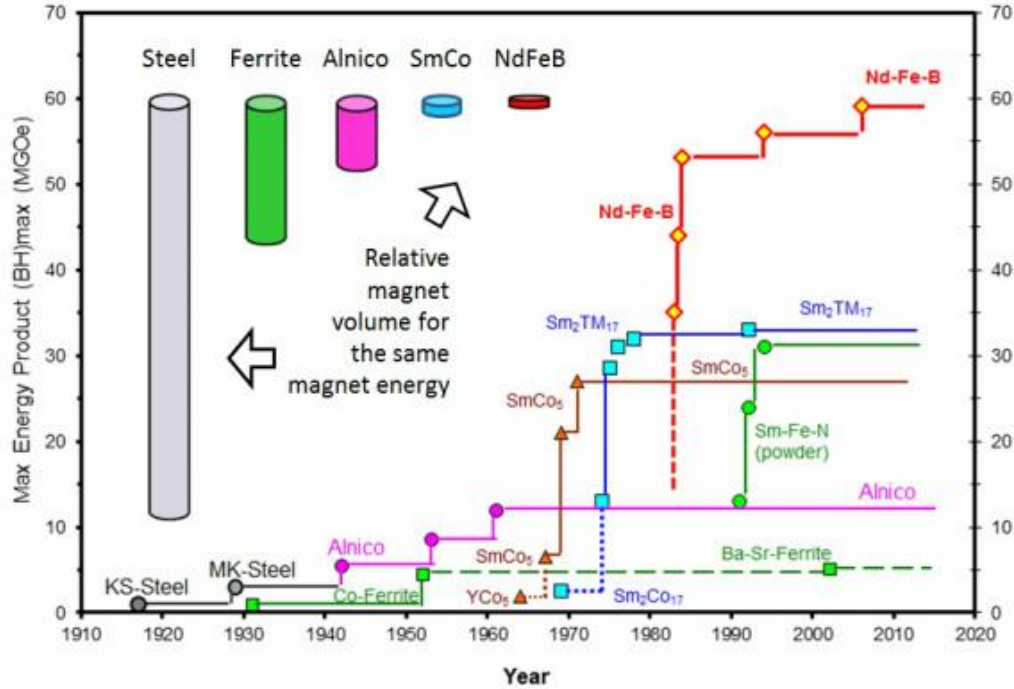


Figure 1.5 Development in the energy product $(BH)_{max}$ at room temperature of hard magnetic materials (each magnet is designed so that at a reference point 5 mm from the surface of the pole, a field of 100 mT is produced) [12].

1.3. Magnetic Exchange Coupling

The large-scale applications of RE permanent magnets in electric vehicles and wind turbines lead to a large consumption of RE elements, while RE elements are not sustainably supplied. Therefore, to design and develop new types of permanent magnets containing no RE elements but with large $(BH)_{max}$ has become extremely important and urgent [14]. Different from the permanent magnets discovered in the 20th century that only containing single-phase magnetic alloy or compound, the new generation of permanent magnets may be a composite material consisting of both hard and soft magnetic phases with required morphology at nano scale. This composite will make use of high coercivity of the hard phase, and high magnetization of soft phase [15]. If these two phases are well magnetically exchange coupled with each other, the composites will behave like a single-phase magnet, and the $(BH)_{max}$ of composites can be improved from the pure hard phase. Therefore, exchange coupled magnets have the potentials to be the next genera-

tion of permanent magnets [16]. A schematic of magnetic exchange coupling process is given in Fig. 1.6 [17]. A typical example could be that magnetically hard FePt (low M_s and high H_c) is exchange coupled with magnetically soft Fe₃Pt (high M_s and low H_c). The $(BH)_{max}$ of exchange coupled FePt/Fe₃Pt composites is improved from their either single phase [31].

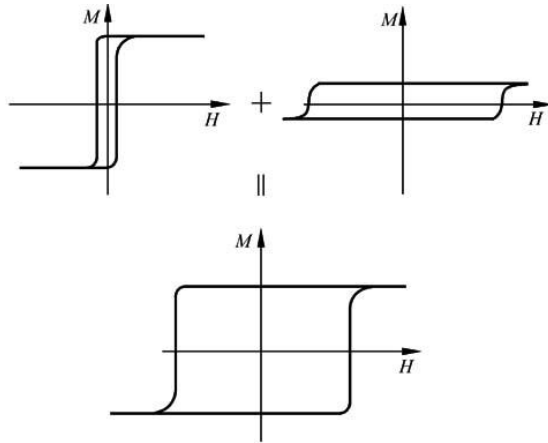


Figure 1.6 Schematic of hysteresis loops of the exchange-coupled magnets [17].

1.3.1. Theory of magnetic exchange coupling

The magnetic exchange coupling was firstly discovered by Coehoorn and his coworkers in 1989 from their experiments in a nanostructured Nd-Fe-B magnet [18]. They found that there was an interphase exchange coupling between the hard phase of Nd₂Fe₁₄B and the soft phase of Fe₃B, which resulted in an enhanced remanent magnetization of the system over the pure hard phase. Kneller et al. gave a detailed theoretic analysis and explanation on magnetic exchange coupling in 1991 [15]. Skomski and Coey further theoretically explained exchange coupling from the points of nucleation field, and the interactions between hard and soft regions [19]. The following is the derivation of the topological condition for the interphase exchange coupling in hard/soft phase composites [19-22]. A ferromagnetic system can be described by its energy state in equation 1.1:

$$E = \int [A(r) \left(\frac{\nabla M}{M_0} \right)^2 - K_1(r) \frac{(n \cdot M)^2}{M_0^2} - \mu_0 M \cdot H] dr \quad (1.1)$$

where H denotes the internal field, which is the sum of the externally applied field and the magnetostatic “demagnetizing” field. $A(r)$ is the exchange stiffness, $M(r)$ with $|M(r)| = M_0$ is the local magnetization, and $K_1(r)$ is the first anisotropy constant, and n is the unit vector in the easy-axis direction. Inside the bracket, the first term is the energy of magnetic exchange interaction, the second term is the anisotropy energy, and the third term is the magnetostatic energy. Magnetic moment configuration is determined by competition among these terms. Exchange interaction favors parallel spin alignment, whereas the random anisotropy, supported by random magnetostatic fields, tends to misalign the spins. If we consider an ideally aligned (n is parallel with easy direction) situation and only take m_x into account (it is sufficient because of the degeneracy), and then minimize the energy with respect to the small magnetization component m_x , the equation can be shown as 1.2:

$$-A\nabla^2 m_x + K_1 m_x = \frac{\mu_0}{2} M_0(r) H_n m_x \quad (1.2)$$

where H_n is a critical field. If the considered system is inhomogeneous in morphological structure, the magnetic reversal is caused by nucleation of opposite domains. In this case, the critical field is called nucleation field.

Equation (1.2) has been solved for a number of cases. A simple example is a spherical soft inclusion of radius R_0 in a hard matrix. Putting $K_1 = 0$ inside the sphere and solving (1.2) for $m_x(R_0) = 0$ yields the nucleation field $H_n = 2\pi^2 A/\mu_0 M_s R_0^2$. If this is written in terms of the anisotropy field H_a of the hard matrix, equation (1.3) can be obtained:

$$H_n = H_a \frac{\delta_h^2}{R_0^2} \quad (1.3)$$

where δ_h is the domain-wall thickness of the magnetic hard phase. The validity of (1.3) is restricted to $H_n \ll H_a$, because $m_x(R_0) = 0$ is only approximately true for finite H_a . If H_n is comparable to H_a , equation (1.3) slightly overestimates the nucleation field. The R_0 dependence of the

nucleation field is shown in Fig. 1.7. Note that boundary conditions have been applied. Smooth transitions between the hard and soft phases yield a $1/R_0$ rather than a $1/R_0^2$ dependence of H_n [22]. Grain size of the soft phase in exchange coupled nanocomposites should not be bigger than twice domain wall thickness of the hard phase, as shown in Fig. 1.7.

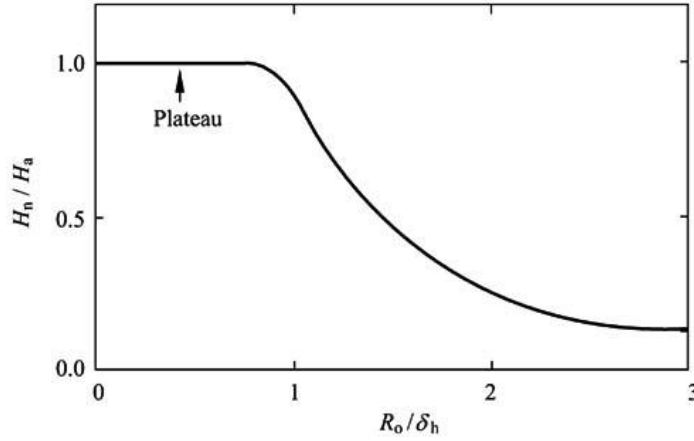


Figure 1.7 Nucleation fields of soft magnetic spherical inclusions in a hard matrix [19].

Sabiryanov et al. [23,24] obtained the theoretical values of energy products of fully exchange coupled FePt-Fe and SmCo-Co layered thin film systems with first principle calculations. They found that the energy products for these two composites can reach 90 MGOe and 65 MGOe, respectively. Kronmüller et al. [25] had carried out a systematic study in simulating the exchange coupled nanocomposite systems.

In a given hard/soft magnetically exchange coupled system, if the volume percent of the hard phase and soft phase is fixed, the magnetization and coercivity of the composites can be calculated based on the following equations [19].

$$M_{ex} = M_h f_h + M_s f_s \quad (1.4)$$

$$H_{ex} = 2 \frac{K_h f_h + K_s f_s}{M_h f_h + M_s f_s} = \frac{M_h f_h H_h + M_s f_s H_s}{M_h f_h + M_s f_s} \quad (1.5)$$

where

M_{ex} : magnetization of exchange coupled product M_h : magnetization of hard phase

M_s : magnetization of soft phase

H_s : coercivity of soft phase

H_{ex} : covercivity of exchange coupled product

H_h : covercivity of hard phase

f_s : volume fraction of soft phase

f_h : volume fraction of hard phase

K_s : anisotropy constant of soft phase

K_h : anisotropy constant of hard phase

1.3.2. Experimental development of exchange coupling

Since Coehoorn and his coworkers experimentally discovered enhanced remanent magnetization in exchange coupled hard/soft $\text{Nd}_2\text{Fe}_{14}\text{B}/\text{Fe}_3\text{B}$ composites over pure $\text{Nd}_2\text{Fe}_{14}\text{B}$ in 1989 [18], exchange coupling in NdFeB based system has been extensively investigated. Panagiotopoulos et al. [26] synthesized thin film $\text{Nd}_2\text{Fe}_{14}\text{B}/\alpha\text{-Fe}$ nanocomposites with sputtering from cast alloy targets and then annealed ex-situ in a high vacuum. Enhanced remanent magnetization in the hard/soft thin film indicated the exchange coupling between hard and soft phases. Su et al. [27] synthesized NdFeB/FeCo(Fe) composites by depositing soft magnetic FeCo(Fe) nanoparticles on the melt spun NdFeB powders by a chemical reduction. The intergrain exchange coupling between hard and soft phases was demonstrated by the smooth demagnetization curve and enhanced remanent magnetization, as shown in Fig. 1.8. The synthesis method for enhanced magnetic remanence bulk magnets was also extended to spark plasma sintering in this research.

Sawatzki et al. [28] achieved the magnetic exchange coupling in the multilayer thin film system of SmCo_5/Fe and enhanced its energy product to 39 MGOe, which is higher than the theoretical value (31MGOe) of anisotropic single phase SmCo_5 magnet. Chaubey et al. [29] synthesized exchange coupled SmCo_5/Fe nanocomposite powders with controlled composition and grain size by polyol reduction of metal precursors and subsequent calcium reductive annealing. Room temperature hysteresis loops of the SmCo_5 nanoparticles, $\text{SmCo}_{5.5}/\text{Fe}_{0.6}$ and $\text{SmCo}_{6.5}/\text{Fe}_{1.2}$ nanocomposites are shown in Fig. 1.9. The energy products of SmCo_5 , $\text{SmCo}_{5.5}/\text{Fe}_{0.6}$ and

$\text{SmCo}_{6.5}/\text{Fe}_{1.2}$ were calculated to be 6.0, 7.1 and 7.8 MGOe, respectively. The smooth hysteresis loops, enhanced remanent magnetization and energy products indicate an effective exchange coupling between hard and soft phases.

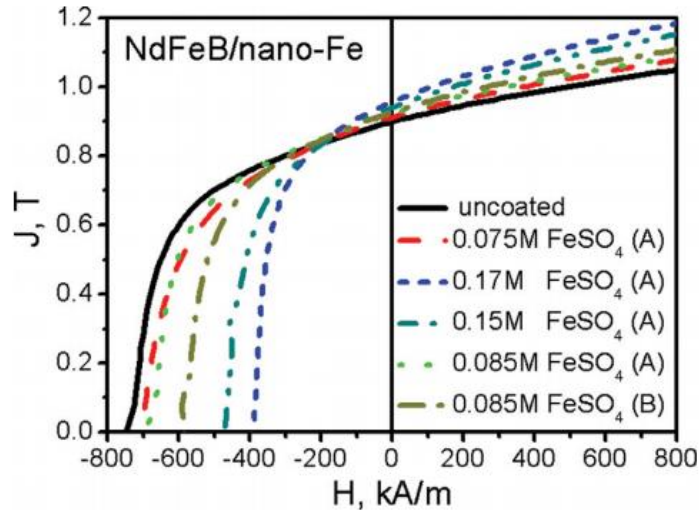


Figure 1.8 Magnetic hysteresis loops for NdFeB single phase and NdFeB/nano-Fe composite powders synthesized by two processes and tuning the concentrations of metal ions, where A and B indicate the process of adding FeSO_4 solution to NaBH_4 solution with NdFeB powders and adding NaBH_4 solution to FeSO_4 solution with NdFeB powders, respectively [27].

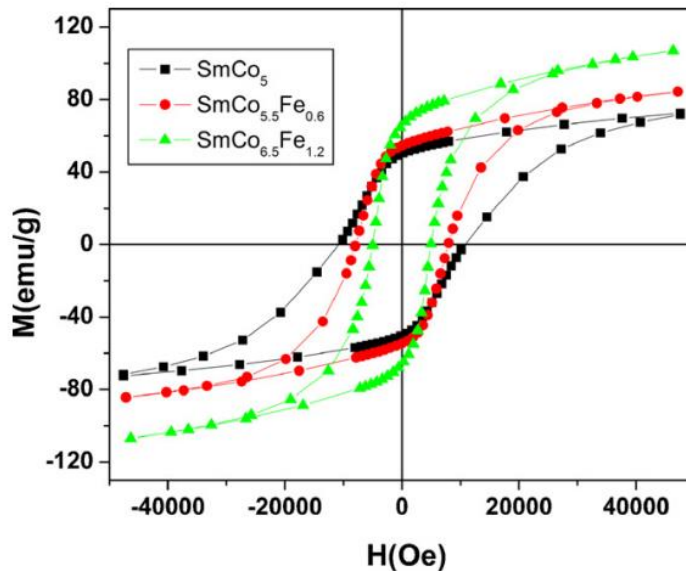


Figure 1.9 Room temperature magnetic hysteresis loops of nanocrystalline SmCo_5 and SmCo_5/Fe nanocomposites [29].

Hou et al.[30] synthesized nanocomposites of $\text{SmCo}_5/\text{Fe}_x$ ($x=0-2.9$) by a simultaneous calcium reduction of Sm-Co-O and Fe_3O_4 nanoparticles. The composites consisted of well crystallized SmCo_5 and Fe nanocrystal with average grain size of 29 nm and 8 nm, respectively, and both of them were well distributed with each other, as shown in Fig. 1.10. The magnetic properties of the composites can be tuned by regulating Fe mass percentage. $\text{SmCo}_5/\text{Fe}_{1.5}$ shows an enhanced remanent magnetization of 56 emu/g over 45 emu/g in pure hard phase of SmCo_5 .

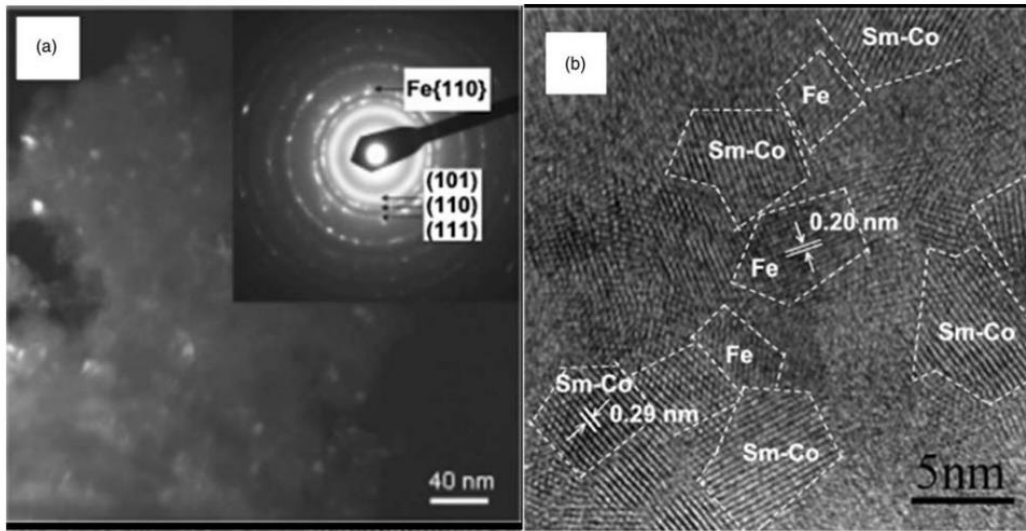


Figure 1.10 (a) Dark field TEM image of SmCo_5/Fe nanocomposites (inset: SAED of the nanocomposites); (b) HRTEM image of a single aggregate of the SmCo/Fe nanocomposites with the dashed lines circling the nanocrystalline grains of either SmCo_5 or Fe [30].

FePt nanoparticles synthesized by wet chemistry methods can be ideal building blocks for exchange-coupled nanocomposite bulk magnets [31-34]. The biggest challenge for the bottom-up approach is how to produce bulk nanostructured magnets without losing the homogeneous nanoscale morphology. Zeng and his coworkers [31] used bottom-up approaches and synthesized exchange coupled nanocomposite magnets using magnetic nanoparticles as building blocks. They reduced FePt/ Fe_3O_4 nanoparticle mixture in a H_2/N_2 environment at 650 °C. These nanoparticles were reduced and self-assembled into hard/soft FePt/ Fe_3Pt composites, with grain size

limited to a few nanometers, as shown in Fig. 1.11. Over 50% energy product enhancement was achieved in the exchange coupled composites.

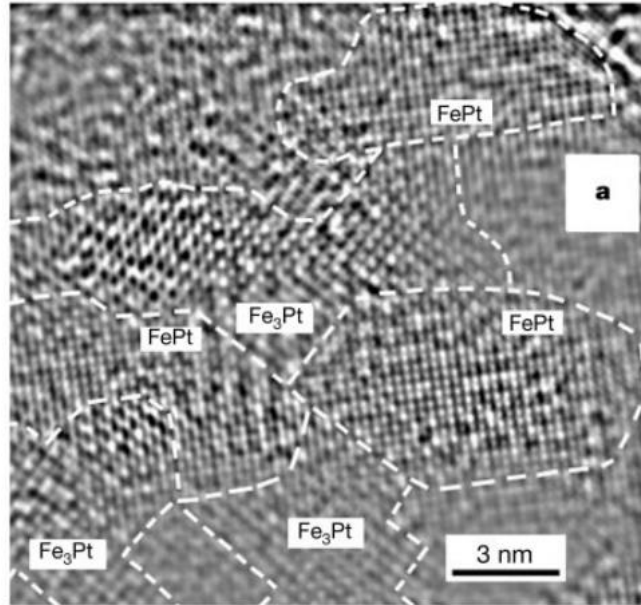


Figure 1.11 A typical HRTEM image for a sintered FePt–Fe₃Pt particle. The FePt and Fe₃Pt phases exist as different domains within the particle, with each domain having a dimension of about 5 nm, showing a modulated FePt–Fe₃Pt spatial distribution [31].

1.3.3. Synthesis challenges of exchange coupled magnet

Even though magnetic exchange coupling has been investigated for more than 20 years [15,18,19], challenges still remain in the synthesis of exchange coupled magnets.

1.3.3.1. Size control of hard phase

Effective exchange coupling requires the soft phase to be uniformly distributed within the hard phase at nano scale. This brings challenges to the materials synthesis. Mechanical milling [35-37] is one of popular methods to achieve a uniform distribution between hard and soft phases because of its low cost and easy operation. Ideally, the hard phase is preferred to be around single domain size (~300-500 nm) for maximum coercivity [1], and the soft phase should be no larger than twice single domain wall thickness of hard phase (usually < 20 nm) [19]. In milling process, both hard and soft phases are strongly milled and well mixed at nanoscale, and effective

exchange coupling is achieved. However, to decrease the size of soft phase to less than 20 nm, the hard phase is inevitably over milled and shows low coercivity because of over reduced size.

Poudyal et al. [35] synthesized exchange coupled $\text{Sm}_2\text{Co}_7/\text{Fe}_{65}\text{Co}_{35}$ composites with mechanical milling. The TEM image and EFTEM elemental mappings of as-synthesized composites are shown in Fig. 1.12. The mapping results show that the size of $\text{Fe}_{65}\text{Co}_{35}$ nanoparticles is less than 20 nm, and homogeneously mixed with hard phase. However, the size of Sm_2Co_7 is similar to FeCo, much less than single domain size of ~ 400 nm [38]. The low coercivity of ~ 8 kOe in $\text{Sm}_2\text{Co}_7/40$ wt% $\text{Fe}_{65}\text{Co}_{35}$ composites could be attributed to the small size of Sm_2Co_7 , while the coercivity of single domain size Sm_2Co_7 is ~ 40 kOe [38].

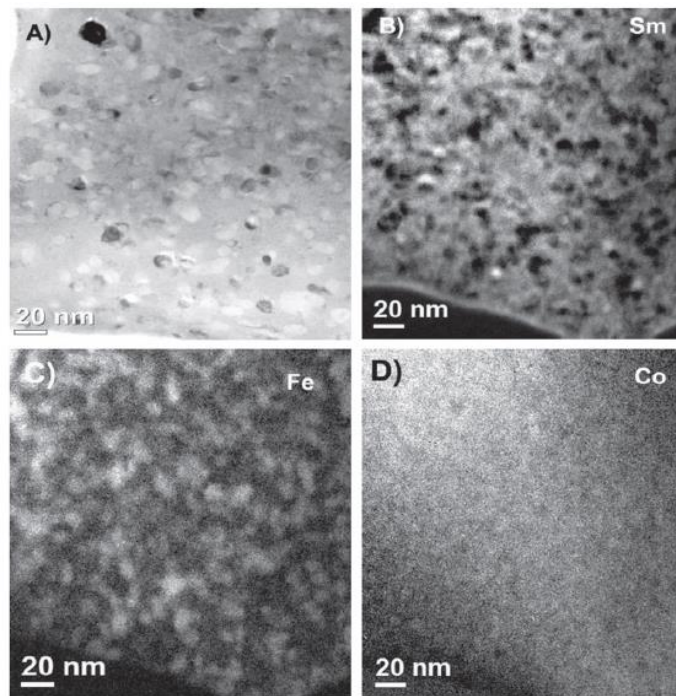


Figure 1.12 (a) Bright field TEM image of $\text{Sm}_2\text{Co}_7 + 40$ wt% $\text{Fe}_{65}\text{Co}_{35}$ and EFTEM elemental mapping for the same areas showing the distribution of (b) Sm, (c) Fe and (d) Co [35].

1.3.3.2. Lattice mismatch between hard/soft phases

Core/shell structured hard/soft particles provide a promising solution to achieve effective exchange coupling [39-41]. Compared with the method mentioned above, the size of hard and

soft phases can be separately controlled in core/shell particles synthesis processes. Epitaxial growth is a common method to synthesize core/shell structured particles. Generally, three types of modes are summarized for epitaxial growth of core/shell particles [42]. If the lattice mismatch between two materials is small, the shell material will precipitate on the surface of core by epitaxial growth and form a continuous and homogenous layer. This growth process is called Frank-van der Merwe (FM) mode, as shown in Fig. 1.13. If the lattice mismatch between two materials is very large, the shell material will grow on those high energy sites of core particles to minimize strain energy, and finally a few islands are formed on the surface of core. This growth mode is called Volmer-Weber (VW), as shown in Fig. 1.14. If the lattice mismatch between two materials is relatively large, growth of shell will change between layer-by-layer growth and island growth on the surface of core, to release strain energy. This growth process is called Stranski-Krastanov (SK) mode, as shown in Fig. 1.15. These three growth modes can be used to understand the formation of a hybrid nanostructures synthesis in wet chemistry, including core/shell, dumbbell and particle-on-particles structures [43-50], even though the surface capping agent and solvents polarization can significantly influence the energy of substrate surface, active sites and growth kinetics.

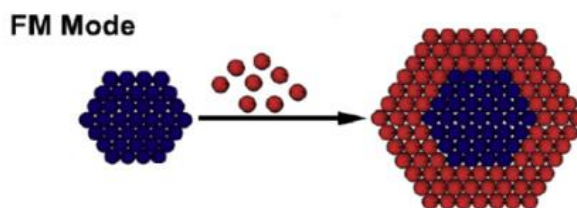


Figure 1.13 Schematic illustration of Frank-van der Merwe mode [42].

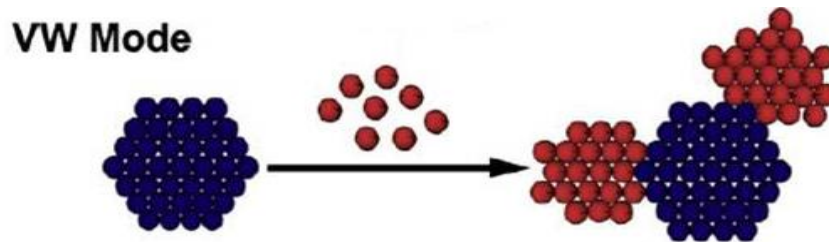


Figure 1.14 Schematic illustration of Volmer-Weber mode [42].

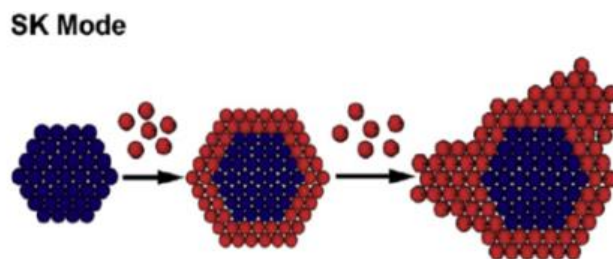


Figure 1.15 Schematic illustration of Stranski-Krastanov mode [42].

Large lattice mismatch is common between magnetically hard and soft magnets and this limits the application of epitaxial growth to synthesize hard/soft core/shell magnetic particles for exchange coupling [51-53]. The failure of epitaxial growth for core/shell structured materials has stimulated the discovery of other alternative methods, such as non-epitaxial growth [54] and anion coordination [55]. However, there is still no general method reported for effective synthesis of core/shell structured materials.

1.3.3.3. Hard and soft phase diffusion

In most cases, high temperature is necessary to reduce the metal oxides and/or crystallize the materials during the synthesis of hard/soft exchange coupled nanocomposites. High temperature may lead to mass diffusion between hard and soft phases as nanomaterials show low thermal stability. The diffusion may result in crystal structure damage and magnetization and coercivity loss. According to theoretical model [19], the relationship between the volume of soft phase and coercivity and magnetization in an exchange coupling system can be described as Fig. 1.16. It

can be observed that both coercivity and magnetization response gradually with soft phase volume changing. However, if the mass diffusion happens between hard and soft phases, the results can be different. Liu et al. synthesized FePt/Co core/shell exchange coupled magnetic nanoparticles [40]. The relationship between cobalt layer thickness and magnetization and coercivity in FePt/Co nanoparticles is shown in Fig. 1.17. It can be seen that when the cobalt shell thickness increases from 0 to 4 nm, the magnetization increases ~100%, however, the coercivity decreases ~300%. This unbalanced magnetization increasing and coercivity decreasing could be attributed to the mass diffusion between FePt and Co during the high temperature (250 °C) synthesis.

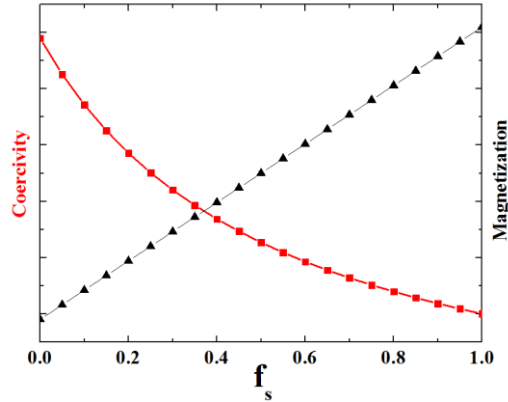


Figure 1.16 The relationship between volume percentage of soft phase (f_h) and magnetization and coercivity of exchange coupled composites in an exchange coupling system.

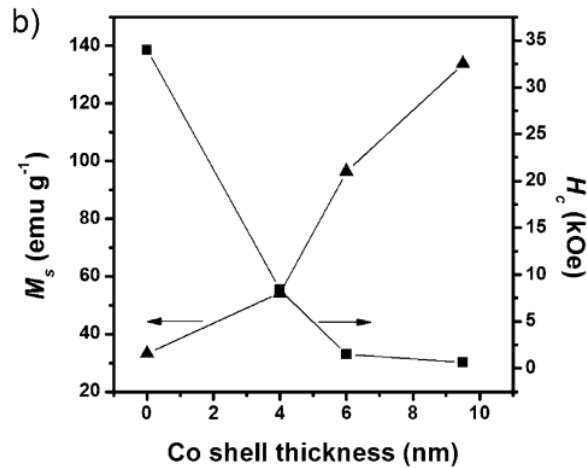


Figure 1.17 Co shell-thickness-dependent M_s and H_c for the FePt/Co core/shell nanoparticles [40].

1.4. References

1. Cullity, B. D. & Graham, C. D. *Introduction to Magnetic Materials*. (Wiley, 2009).
2. Giri, S., Trewyn, B. G., Stellmaker, M. P. & Lin, V. S. Y. Stimuli-Responsive Controlled-Release Delivery System Based on Mesoporous Silica Nanorods Capped with Magnetic Nanoparticles. *Angewandte Chemie-International Edition*, **44**, 5038-5044 (2005).
3. Nunez, L. & Kaminski, M. D. Transuranic Separation Using Organophosphorus Extractants Adsorbed onto Superparamagnetic Carriers. *Journal of Magnetism and Magnetic Materials*, **194**, 102-107 (1999).
4. Ge, J. P., Zhang, Q., Zhang, T. R. & Yin, Y. D. Core-Satellite Nanocomposite Catalysts Protected by a Porous Silica Shell: Controllable Reactivity, High Stability, and Magnetic Recyclability. *Angewandte Chemie-International Edition*, **47**, 8924-8928 (2008).
5. Lu, A. H., Salabas, E. L. & Schuth, F. Magnetic Nanoparticles: Synthesis, Protection, Functionalization, and Application. *Angewandte Chemie-International Edition*, **46**, 1222-1244 (2007).
6. Xu, C. J. *et al.* Dopamine as a Robust Anchor to Immobilize Functional Molecules on the Iron Oxide Shell of Magnetic Nanoparticles. *Journal of the American Chemical Society*, **126**, 9938-9939 (2004).
7. Widder, K. J., Senyei, A. E. & Scarpelli, D. G. Magnetic Microspheres: A Model System for Site Specific Drug Delivery in Vivo. *Experimental Biology and Medicine*, **158**, 141-146 (1978).
8. Gupta, A. K. & Gupta, M. Synthesis and Surface Engineering of Iron Oxide Nanoparticles for Biomedical Applications. *Biomaterials*, **26**, 3995-4021 (2005).
9. Berry, C. C. & Curtis, A. S. G. Functionalisation of Magnetic Nanoparticles for Applications in Biomedicine. *Journal of Physics D-Applied Physics*, **36**, R198-R206 (2003).
10. Hiergeist, R. *et al.* Application of Magnetite Ferrofluids for Hyperthermia. *Journal of Magnetism and Magnetic Materials*, **201**, 420-422 (1999).
11. Gutfleisch, O. Controlling the Properties of High Energy Density Permanent Magnetic Materials by Different Processing Routes. *Journal of Physics D-Applied Physics*, **33**, R157-R172 (2000).
12. Gutfleisch, O. *et al.* Magnetic Materials and Devices for the 21st Century: Stronger, Lighter, and More Energy Efficient. *Advanced Materials*, **23**, 821-842 (2011).
13. Buschow, K. H. J., Feijen, F. H. & Dekort, K. Rare-Earth Permanent-Magnets. *Journal of Magnetism and Magnetic Materials*, **140**, 9-12 (1995).
14. Poudyal, N. & Liu, J. P. Advances in Nanostructured Permanent Magnets Research. *Journal of Physics D-Applied Physics*, **46** (2013).
15. Kneller, E. F. & Hawig, R. The Exchange-Spring Magnet - A New Material Principle for Permanent-Magnets. *IEEE Transactions on Magnetics*, **27**, 3588-3600 (1991).

16. Bader, S. D. Colloquium: Opportunities in Nanomagnetism. *Reviews of Modern Physics*, **78**, 1-15 (2006).
17. Hernando, A. & Gonzalez, J. M. Soft and Hard Nanostructured Magnetic Materials. *Hyperfine Interactions*, **130**, 221-240 (2000).
18. Coehoorn, R., Demooij, D. B. & Dewaard, C. Meltspun Permanent-Magnet Materials Containing Fe₃B as the Main Phase. *Journal of Magnetism and Magnetic Materials*, **80**, 101-104 (1989).
19. Skomski, R. & Coey, J. M. D. Giant Energy Product in Nanostructured 2-Phase Magnets. *Physical Review B*, **48**, 15812-15816 (1993).
20. Skomski, R. & Coey, J. M. D. *Permanent Magnetism*. (Institute of Physics Publishing, 1999).
21. Straubel, H. Magnetostatic Principles in Ferromagnetism. *Zeitschrift Fur Angewandte Physik*, **19**, 83-92 (1965).
22. Kronmuller, H. Theory of Nucleation Fields in Inhomogeneous Ferromagnets. *Physica Status Solidi B-Basic Research*, **144**, 385-396 (1987).
23. Sabiryanov, R. F. & Jaswal, S. S. Electronic Structure and Magnetic Properties of Hard/Soft Multilayers. *Journal of Magnetism and Magnetic Materials*, **177**, 989-990 (1998).
24. Sabiryanov, R. F. & Jaswal, S. S. Magnetic Properties of Hard/Soft Composites: SmCo₅/Co_{1-x}Fe_x. *Physical Review B*, **58**, 12071-12074 (1998).
25. Kronmuller, H., Fischer, R., Bachmann, M. & Leineweber, T. Magnetization Processes in Small Particles and Nanocrystalline Materials. *Journal of Magnetism and Magnetic Materials*, **203**, 12-17 (1999).
26. Panagiotopoulos, I. & Hadjipanayis, G. C. Thin Film Nanocomposite Nd₂Fe₁₄B/Alpha-Fe Magnets. *Nanostructured Materials*, **10**, 1013-1022 (1998).
27. Su, K. P. *et al.* A Feasible Approach for Preparing Remanence Enhanced NdFeB Based Permanent Magnetic Composites. *Journal of Applied Physics*, **109** (2011).
28. Sawatzki, S. *et al.* Largely Enhanced Energy Density in Epitaxial SmCo₅/Fe/SmCo₅ Exchange Spring Trilayers. *Journal of Applied Physics*, **109** (2011).
29. Chaubey, G. S., Poudyal, N., Liu, Y. Z., Rong, C. B. & Liu, J. P. Synthesis of Sm-Co and Sm-Co/Fe Nanocrystals by Reductive Annealing of Nanoparticles. *Journal of Alloys and Compounds*, **509**, 2132-2136 (2011).
30. Hou, Y., Sun, S., Rong, C. & Liu, J. P. SmCo₅/Fe Nanocomposites Synthesized from Reductive Annealing of Oxide Nanoparticles. *Applied Physics Letters*, **91** (2007).
31. Zeng, H., Li, J., Liu, J. P., Wang, Z. L. & Sun, S. H. Exchange-Coupled Nanocomposite Magnets by Nanoparticle Self-Assembly. *Nature*, **420**, 395-398 (2002).
32. Rong, C. B. *et al.* Bulk FePt-Based Nanocomposite Magnets with Enhanced Exchange Coupling. *Journal of Applied Physics*, **102** (2007).

33. Sun, S. H., Murray, C. B., Weller, D., Folks, L. & Moser, A. Monodisperse FePt Nanoparticles and Ferromagnetic FePt Nanocrystal Superlattices. *Science*, **287**, 1989-1992 (2000).
34. Chen, M., Liu, J. P. & Sun, S. H. One-Step Synthesis of FePt Nanoparticles with Tunable Size. *Journal of the American Chemical Society*, **126**, 8394-8395 (2004).
35. Poudyal, N., Rong, C., Nguyen, V. V. & Liu, J. P. Hard-Phase Engineering in Hard/Soft Nanocomposite Magnets. *Materials Research Express*, **1**, 016103 (2014).
36. Wang, D. P. *et al.* Exchange-Coupled Nanoscale SmCo/NdFeB Hybrid Magnets. *Journal of Magnetism and Magnetic Materials*, **324**, 2836-2839 (2012).
37. Ma, Y. L. *et al.* Preparation and Magnetic Properties of MnBi-Based Hard/Soft Composite Magnets. *Journal of Applied Physics*, **115** (2014).
38. Wecker, J., Katter, M. & Schultz, L. Mechanically Alloyed Sm-Co Materials. *Journal of Applied Physics*, **69**, 6058-6060 (1991).
39. Song, Q. & Zhang, Z. J. Controlled Synthesis and Magnetic Properties of Bimagnetic Spinel Ferrite CoFe_2O_4 and MnFe_2O_4 Nanocrystals with Core-Shell Architecture. *Journal Of The American Chemical Society*, **134**, 10182-10190 (2012).
40. Liu, F. *et al.* Building Nanocomposite Magnets by Coating a Hard Magnetic Core with a Soft Magnetic Shell. *Angewandte Chemie-International Edition*, **53**, 2176-2180 (2014).
41. Zeng, H., Sun, S. H., Li, J., Wang, Z. L. & Liu, J. P. Tailoring Magnetic Properties of Core/Shell Nanoparticles. *Applied Physics Letters*, **85**, 792-794 (2004).
42. Chambers, S. A. Epitaxial Growth and Properties of Thin Film Oxides. *Surface Science Reports*, **39**, 105-180 (2000).
43. Zhao, D. & Xu, B. Q. Platinum Covering of Gold Nanoparticles for Utilization Enhancement of Pt in Electrocatalysts. *Physical Chemistry Chemical Physics*, **8**, 5106-5114 (2006).
44. Zhao, D. & Xu, B. Q. Enhancement of Pt Utilization in Electrocatalysts by Using Gold Nanoparticles. *Angewandte Chemie-International Edition*, **45**, 4955-4959 (2006).
45. Park, I. S., Lee, K. S., Jung, D. S., Park, H. Y. & Sung, Y. E. Electrocatalytic Activity of Carbon-Supported Pt-Au Nanoparticles for Methanol Electro-Oxidation. *Electrochimica Acta*, **52**, 5599-5605 (2007).
46. Zhou, S. G., McIlwrath, K., Jackson, G. & Eichhorn, B. Enhanced Co Tolerance for Hydrogen Activation in Au-Pt Dendritic Heteroaggregate Nanostructures. *Journal of the American Chemical Society*, **128**, 1780-1781 (2006).
47. Wang, D. S., Zhao, P. & Li, Y. D. General Preparation for Pt-Based Alloy Nanoporous Nanoparticles as Potential Nanocatalysts. *Scientific Reports*, **1** (2011).
48. Pellegrino, T. *et al.* Heterodimers Based on CoPt_3 -Au Nanocrystals with Tunable Domain Size. *Journal of the American Chemical Society*, **128**, 6690-6698 (2006).
49. Habas, S. E., Lee, H., Radmilovic, V., Somorjai, G. A. & Yang, P. Shaping Binary Metal Nanocrystals through Epitaxial Seeded Growth. *Nature Materials*, **6**, 692-697 (2007).

50. Yu, H. *et al.* Dumbbell-Like Bifunctional Au-Fe₃O₄ Nanoparticles. *Nano Letters*, **5**, 379-382 (2005).
51. Fan, F. R. *et al.* Epitaxial Growth of Heterogeneous Metal Nanocrystals: From Gold Nano-Octahedra to Palladium and Silver Nanocubes. *Journal of the American Chemical Society*, **130**, 6949-6455 (2008).
52. Wang, Z. L. Transmission Electron Microscopy of Shape-Controlled Nanocrystals and Their Assemblies. *Journal of Physical Chemistry B*, **104**, 1153-1175 (2000).
53. Palmstrom, C. J. Epitaxy of Dissimilar Materials. *Annual Review of Materials Science*, **25**, 389-415 (1995).
54. Zhang, J. T., Tang, Y., Lee, K. & Min, O. Y. Nonepitaxial Growth of Hybrid Core-Shell Nanostructures with Large Lattice Mismatches. *Science*, **327**, 1634-1638 (2010).
55. Serpell, C. J., Cookson, J., Ozkaya, D. & Beer, P. D. Core@Shell Bimetallic Nanoparticle Synthesis Via Anion Coordination. *Nature Chemistry*, **3**, 478-483 (2011).

CHAPTER 2 EXPERIMENTAL

2.1. Chemical Synthesis Methods

Most materials used in this dissertation research are synthesized with chemistry methods, in which materials' size and morphology can be better controlled than physics methods. Specifically, four different kinds of chemistry methods are used for materials synthesis. They are reduction of metal-containing compounds, solid state synthesis, spray pyrolysis and reverse micro-emulsion. The characteristics and details of these methods are discussed below.

2.1.1. Reduction of metal-containing compounds

Fe-Co alloy nanoparticles are synthesized from iron and cobalt salts with strong reducing agents, such as NaBH_4 , ethylene glycol and n-butyllithium. The iron and cobalt salts can be either organic (such as $\text{Fe}(\text{acac})_3$ and $\text{Co}(\text{acac})_2$) or inorganic (such as FeCl_3 (or FeCl_2) and CoCl_2). Even though thermal decomposition of $\text{Fe}(\text{CO})_5$ and $\text{Co}_2(\text{CO})_8$ is an effective method to synthesize FeCo nanoparticles with uniform size and high magnetization [1], it is not used in this research, as metal-carbonyl is very flammable and toxic [2].

2.1.2. Solid state synthesis

Solid state synthesis technique involves annealing mixtures of two or more solids to form a solid phase product [3]. Different from gas phase or liquid phase reactions, the mass diffusion is important factor that limits the solid-solid reactions. The reaction rate is controlled by three factors: 1) contacting area between solid precursors; 2) diffusion rate during the reaction; 3) nucleation rate of product phase. Hexagonal strontium ferrite ($\text{SrFe}_{12}\text{O}_{19}$) is synthesized with solid state

reaction by annealing Fe_3O_4 and SrCO_3 nanoparticles at $900\text{ }^\circ\text{C}$ for 4 hours at atmospheric environment.

2.1.3. Spray pyrolysis

Spray pyrolysis is a popular method to produce spherical metal oxide particles by thermal decomposition of precursors at high temperature [4-7]. Generally, there are three components in a spray pyrolysis system, as shown in Fig. 2.1, an ultrasonic nebulizer to generate droplets containing precursors, a tubular furnace to thermally decompose precursors, and a particle collector to gather the products [4]. The droplets are flowed through the furnace with carried gas. Solid spherical particles can be obtained if the precursor solution does not contain organics. The hollowness of products can be controlled by adding water soluble organics in precursor solutions [8,9]. Within a certain range, the shell thickness decreases with increasing organics concentration. However, if the concentration of organics is too high, it will lead to an over high pressure inside the particle during the combustion, and break the hollow structure, forming smaller crystal pieces.

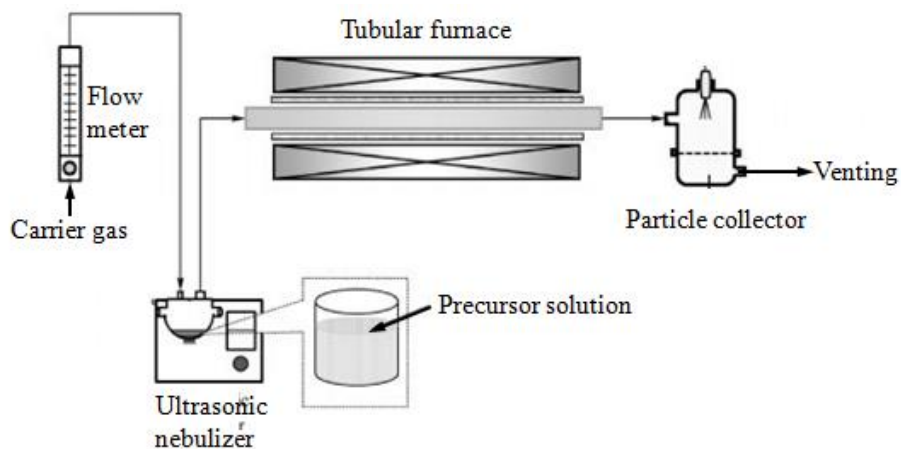


Figure 2.1 Schematic of spray pyrolysis system.

2.1.4. Reverse microemulsion

The technique of chemical reactions in reverse microemulsion to produce nanoparticles has been developed for more than 20 years [10-14]. Microemulsions are thermodynamically stable

system composed of two immiscible liquids and a surfactant[15]. The surfactant is used to disperse oil in water by dividing oil phase into small droplets. The opposite process of dispersing water in oil is called reverse microemulsion, as shown in Fig. 2.2. The droplet size can be controlled by changing the molar ratio of water or oil to surfactant. These nanodroplets can be used as nanoreactors to carry out chemical reactions. In this research, the nano size iron oxide and strontium carbonate are synthesized from reverse microemulsion, followed by annealing the nanoparticle mixture to get worm-shape strontium ferrite. The experimental details will be shown in Chapter 3.3.

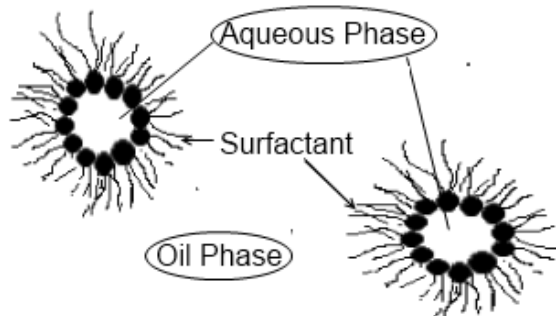


Figure 2.2 Reverse micelles in a microemulsion [14].

2.2. Characterization Techniques

2.2.1. X-ray Diffraction (XRD)

Bruker D8X-ray diffractometers with Cu-K α (wavelength $\lambda=1.541 \text{ \AA}$) and Co-K α (wavelength $\lambda=1.789 \text{ \AA}$) radiation were used to characterize materials' crystalline structure. The range of 2θ was typically controlled to $20-90^\circ$.

The incident X-ray follows Bragg's law as described in Fig. 2.3 and the following formula[16]:

$$n\lambda = 2d \sin\theta \quad (2.1)$$

where n is an integer, λ is the wavelength of incident wave, d is the spacing between the planes in the atomic lattice, and θ is the angle between the incident X-ray and the scattering planes. By changing the angle θ , the conditions of Bragg's Law can be satisfied by different d -spacing in materials. A pattern with sample characteristics can be produced by plotting the angular positions and intensities of the resultant diffracted peaks. If equation (2.1) is rearranged to the following form considering a first order reflection:

$$\theta = \arcsin(\lambda/2d) \quad (2.2)$$

The distance between lattice planes can be calculated using the following formula:

$$d = a / (h^2 + k^2 + l^2)^{1/2} \quad (2.3)$$

Since the lower order Miller indices result in a larger inter-planar spacing in equation (2.3), the diffraction angle in equation (2.2) will be lower. Therefore, as the Miller indices increase, the diffraction angles will also increase.

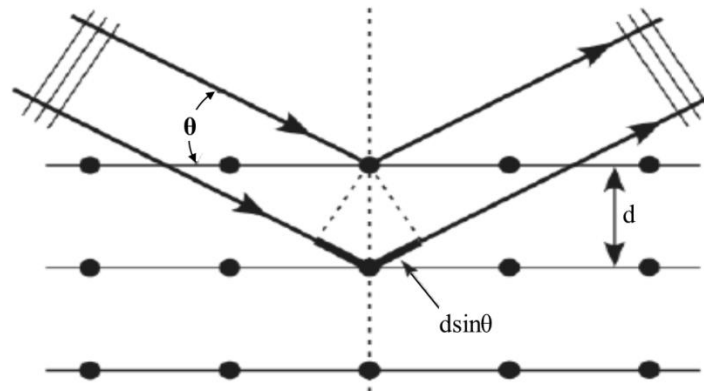


Figure 2.3 Bragg's law [16].

2.2.2. Scanning Electron Microscopy (SEM)

A JEOL 7000 of scanning electron microscope (SEM) was used to characterize samples in this research, and a schematic of SEM system is shown in Fig. 2.4. Different from Transmission Electron Microscope (TEM) that requires samples to be very thin for high resolution image,

SEM prefers larger samples. The sample information of morphology, surface topology, and composition can be obtained through this technique.

A basic requirement for SEM samples is that samples, at least sample surface, should be electrically conductive to prevent the charge accumulation. Nonconductive samples tend to accumulate electrons on sample surface when scanned by the electron beam, leading to image shifting. To make nonconductive sample conductive, samples are usually coated with a thin layer of gold or carbon on surface by low-vacuum sputter coating or high vacuum evaporation.

Different electron detectors can capture different types of scattered electrons and provide different information of the samples. For example, backscattered electron can be captured to analyze sample compositions, and secondary electrons can be captured to analyze topography. If an Energy Dispersive X-ray (EDX) detector is connected, elemental composition of samples can be analyzed in both quality and quantity.

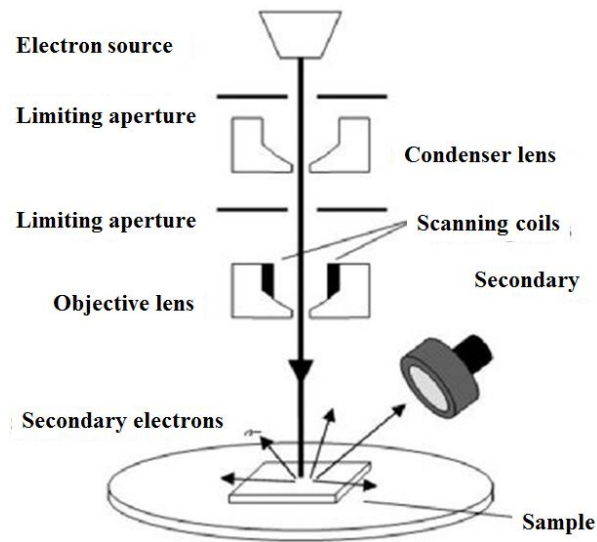


Figure 2.4 Schematic of Scanning Electron Microscope (SEM) system [17].

2.2.3. Transmission Electron Microscopy (TEM)

Transmission Electron Microscopy (TEM) (in Fig. 2.5) is currently the only characterization technique to directly visualize the nanoparticles for their particle size, size distribution and

morphology. The TEM used in this research is TECNAI FEI 20. TEM with an Energy-dispersive X-ray detector can also be used to determine the composition of samples. It requires samples to be thin enough so that electrons can transmit through them and arrive at detector.

There are two modes of TEM image, bright field imaging and dark field imaging [18]. Bright field imaging mode is the most common TEM operation mode. In this mode, the image contrast is formed by electrons occlusion and absorption in the sample. For example, samples regions with thicker thickness or higher atomic number will show dark in the image, as the electrons lose more energy when transmitting these areas, and show weak signal intensity when they reach the detector. A dark field image is formed with only diffraction beams. The crystallographic information can be obtained from this type of image.

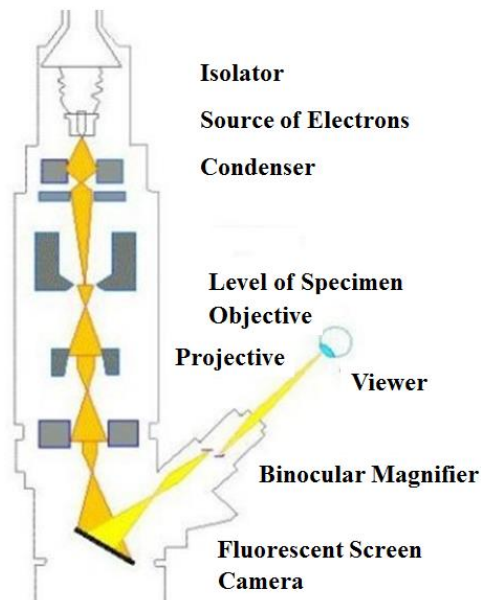


Figure 2.5 Schematic of Transmission Electron Microscope (TEM) system [19].

2.2.4. Vibrating Sample Magnetometry (VSM)

A vibrating sample magnetometer (VSM) is used to measure the $M-H$ loops of the magnetic particles, from which the saturation magnetization, remanent magnetization and coercivity can

be determined [20-23]. The VSM used in this research is Microsense 3473-70, with applied field up to 2.0 T. This method of measurement is fast and accurate as it usually has a low noise level. In the measurement, the sample is loaded into a glass VSM sample holder, which is then mounted on the tip of a vertical extension rod, as shown in Fig. 2.6. The gradient coils apply an AC gradient field which exerts an oscillatory force on the magnetized sample. This causes the bending of the transducer and produces a voltage proportional to the amplitude of the oscillation, which is proportional to the magnetic moment of the sample. The signal is optimized when the vibrating frequency of the sample reaches the resonance frequency of the cantilever system. The system needs to be periodically calibrated with a standard magnet with known magnetic moment for accurate measurements. We used a standard Nickel sample (0.0707 g) with a magnetic moment of 54.9 emu/g at 1000 Oe magnetic field for the calibration.

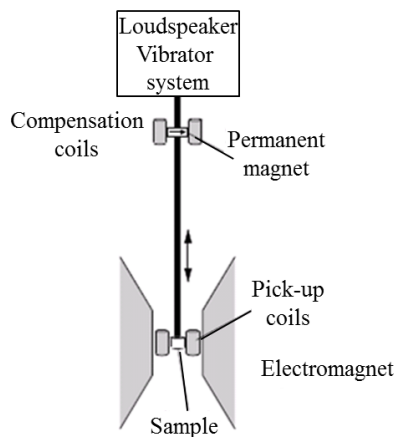


Figure 2.6 Schematic of Vibrating Sample Magnetometer (VSM) system [20].

2.3. References

1. Wang, C., Peng, S., Lacroix, L. M. & Sun, S. H. Synthesis of High Magnetic Moment CoFe Nanoparticles Via Interfacial Diffusion in Core/Shell Structured Co/Fe Nanoparticles. *Nano Research*, **2**, 380-385 (2009).
2. Chaubey, G. S. *et al.* Synthesis and Stabilization of Feco Nanoparticles. *Journal of the American Chemical Society*, **129**, 7214-7210 (2007).

3. Liu, J. P., Fullerton, E., Gutfleisch, O. & Sellmyer, D. J. *Nanoscale Magnetic Materials and Applications*. (Springer US, 2009).
4. Jung, D. S., Bin Park, S. & Kang, Y. C. Design of Particles by Spray Pyrolysis and Recent Progress in Its Application. *Korean Journal Of Chemical Engineering*, **27**, 1621-1645 (2010).
5. Messing, G. L., Zhang, S. C. & Jayanthi, G. V. Ceramic Powder Synthesis by Spray-Pyrolysis. *Journal of the American Ceramic Society*, **76**, 2707-2726 (1993).
6. Senzaki, Y., Caruso, J., Hampdensmith, M. J., Kodas, T. T. & Wang, L. M. Preparation of Strontium Ferrite Particles by Spray-Pyrolysis. *Journal of the American Ceramic Society*, **78**, 2973-2976 (1995).
7. Ren, P., Guan, J. G. & Cheng, X. D. Influence of Heat Treatment Conditions on the Structure and Magnetic Properties of Barium Ferrite BaFe₁₂O₁₉ Hollow Microspheres of Low Density. *Materials Chemistry and Physics*, **98**, 90-94 (2006).
8. Kang, H. S., Sohn, J. R., Kang, Y. C., Jung, K. Y. & Park, S. B. The Characteristics of Nano-Sized Gd-Doped CeO₂ Particles Prepared by Spray Pyrolysis. *Journal of Alloys and Compounds*, **398**, 240-244 (2005).
9. Zhong, K., Peabody, G., Glicksman, H. & Ehrman, S. Particle Generation by Cosolvent Spray Pyrolysis: Effects of Ethanol and Ethylene Glycol. *Journal of Materials Research*, **27**, 2540-2550 (2012).
10. Palla, B. J., Shah, D. O., Garcia-Casillas, P. & Matutes-Aquino, J. Preparation of Nanoparticles of Barium Ferrite from Precipitation in Microemulsions. *Journal of Nanoparticle Research*, **1**, 215-221 (1999).
11. Bellusci, M. *et al.* Preparation of Albumin-Ferrite Superparamagnetic Nanoparticles Using Reverse Micelles. *Polymer International*, **58**, 1142-1147 (2009).
12. Gao, X., Du, Y., Liu, X., Xu, P. & Han, X. Synthesis and Characterization of Co-Sn Substituted Barium Ferrite Particles by a Reverse Microemulsion Technique. *Materials Research Bulletin*, **46**, 643-648 (2011).
13. Jotania, R. B., Khomane, R. B., Chauhan, C. C., Menon, S. K. & Kulkarni, B. D. Synthesis and Magnetic Properties of Barium-Calcium Hexaferrite Particles Prepared by Sol-Gel and Microemulsion Techniques. *Journal of Magnetism and Magnetic Materials*, **320**, 1095-1101 (2008).
14. Mittal, K. L., Kumar, P. & NetLibrary Inc. (Marcel Dekker, New York, 1999).
15. Xu, P., Han, X. J. & Wang, M. J. Synthesis and Magnetic Properties of BaFe₁₂O₁₉ Hexaferrite Nanoparticles by a Reverse Microemulsion Technique. *Journal of Physical Chemistry C*, **111**, 5866-5870 (2007).
16. Warren, B. E. *X-Ray Diffraction*. (Addison-Wesley Pub. Co., 1969).
17. Hayat, M. A. *Principles and Techniques of Scanning Electron Microscopy*. (Van Nostrand Reinhold Co., 1974).
18. Keyse, R. J. & Royal Microscopical Society (Great Britain). *Introduction to Scanning Transmission Electron Microscopy*. (BIOS Scientific Publishers, Springer, 1998).

19. Zhang, X.-F. & Zhang, Z. *Progress in Transmission Electron Microscopy*. (Springer, Tsinghua University Press, 2001).
20. Noakes, J. E., Arrott, A. & Haakana, C. Vibrating Sample Magnetometers. *Review of Scientific Instruments*, **39**, 1436-1442 (1968).
21. Foner, S. The Vibrating Sample Magnetometer: Experiences of a Volunteer. *Journal of Applied Physics*, **79**, 4740-4745 (1996).
22. Foner, S. Vibrating Sample Magnetometer. *Review of Scientific Instruments*, **27**, 548-548 (1956).
23. Jahn, L., Scholl, R. & Eckert, D. Vibrating Sample Vector Magnetometer Coils. *Journal of Magnetism and Magnetic Materials*, **101**, 389-391 (1991).

CHAPTER 3 HARD MAGNETIC NANOPARTICLES

3.1. Synthesis and Characterization of Hollow Mesoporous BaFe₁₂O₁₉ Spheres

3.1.1. Introduction

It is well known that the morphology of inorganic particles is related to the physical and chemical properties of materials [1]. Micro/nano size hollow/porous materials have been of great interest because of their novel properties [2-4], such as low density, large surface area, and high permeability, compared with condensed materials. Therefore, they can be widely used for catalyst supports, drug delivery, energy storage, gas sensors and environmental protection [5-9]. Three typical methods are proposed to synthesize this structured material: hard-templating [10-13], soft-templating [14-16], and template-free [17,18] methods. Various porous/hollow optical, thermal, electrochemical, mechanical, biochemical and magnetic materials have been synthesized by these methods [16,19-24].

Among these different materials, porous structured ferrite materials are excellent candidates for applications, such as catalysis, information storage, electronic device and energy storage. Even though mesoporous spinel ferrite has been successfully synthesized with the hydrothermal method [25-30,32], the synthesis of mesoporous hexagonal ferrite (higher coercivity, chemical and physical stability than spinel ferrite) has never been reported. The porous structure can not sustain its high synthesis temperature (> 800 °C) because of sintering.

In this part, we report a template-free chemical etching process to synthesize hollow mesoporous hexagonal barium ferrite (BaFe₁₂O₁₉ or BaM) spheres. Two steps are involved in the synthesis process. First, hollow BaM spheres are synthesized by traditional spray pyrolysis. Second,

the as-synthesized particles are exposed to high temperature alkaline ethylene glycol (EG). Compared with the hydrothermal method in which product porosity can not be controlled, the porosity in this method can be regulated by controlling the reaction time of the EG etching process. Its novel structure should bring novel applications of this material. For example, considering its high chemical and physical stability, it would be an excellent candidate as catalyst support in the high temperature reactions, and its high magnetization provides an effective way to recycle the catalyst after the reactions.

3.1.2. Experimental

3.1.2.1. The synthesis of hollow spherical $\text{BaFe}_{12}\text{O}_{19}$ spheres

The synthesis of hollow BaM spheres is based on a typical spray pyrolysis [33] with little modification. The whole system is shown in Fig. 3.1. Specifically, $\text{Fe}(\text{NO}_3)_3 \cdot 9\text{H}_2\text{O}$ (2.424 g) and $\text{Ba}(\text{NO}_3)_2$ (0.131 g) were dissolved in a solvent consisting of 80 mL deionized water (DI H_2O) and 20 mL ethanol (99% vol.). The solution was then transferred to an ultrasonic nebulizer to generate fine and uniform liquid droplets. In air drawn by building vacuum at the end of the system, the liquid droplets flowed through a tube furnace (Length: 1.0 m; Diameter: 0.08 m) at 1000 °C to thermally decompose the precursors and produce hollow $\text{BaFe}_{12}\text{O}_{19}$ spheres. The mechanism is well understood and described in references [33, 34]. The flow rate was controlled at 5 L/min. The products were then cooled down by a heat exchanger, and finally collected by a fiber filter.

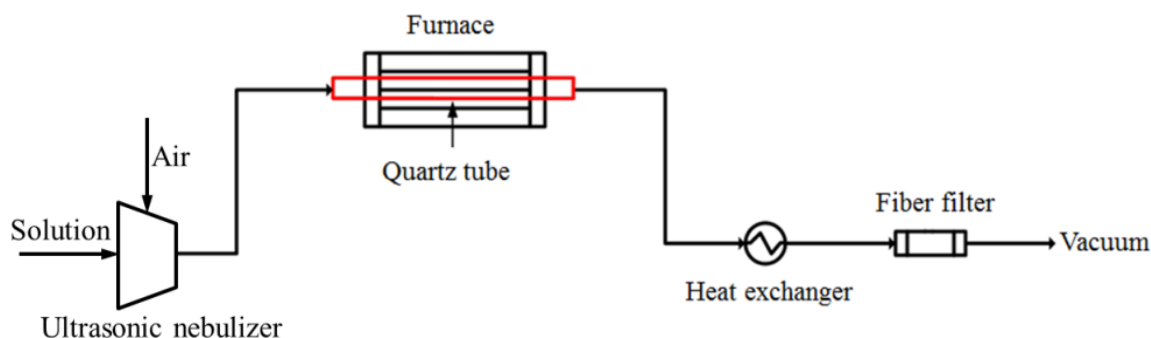


Figure 3.1 The reaction system of spray pyrolysis.

3.1.2.2. The synthesis of hollow mesoporous BaFe₁₂O₁₉ spheres

The hollow mesoporous BaM spheres were obtained by chemically etching the as-synthesized hollow spherical BaM particles. Simply, the as-synthesized BaM particles were dispersed into 60 mL EG under ultrasonication for 30 mins. The as-obtained gel and 2.0 g NaOH were then transferred to a 100 mL three-neck flask. The flask was heated from room temperature, at a heating rate of 10 °C/min, to 185 °C and held for a few minutes. Different heating times lead to different porosities, and the details will be discussed below. After heating, the suspension was finally cooled down to room temperature by removing the heating source, washed with ethanol and dried for the following characterizations.

3.1.2.3. Characterization

The powder X-ray diffraction patterns were recorded by a Bruker D8 diffractometer using Co-K α radiation ($\lambda = 1.789 \text{ \AA}$). TEM (TECNAI FEI 20) and SEM (JEOL 7000) were used to analyze the particle size and morphology. Magnetic properties were checked at room temperature with a VSM (Microsense 3473-70) in an applied field up to 2 T.

Nitrogen (N₂) physisorption measurements were taken using a Quantachrome Nova 2200e pore size analyzer (Boynton Beach, FL) at -197 °C in the He mode to determine surface

areas of both hollow and mesoporous hollow particles. Interpretation of the isotherms was carried out with Quantachrome's Nova Win software (version: 10.01).

3.1.3. Results and discussion

Figure 3.2 shows the SEM and TEM images of hollow BaM particles before and after EG etching. Figures 3.2a and c show that the as-synthesized particles are spherical with a smooth surface and in the size range of 200 - 500 nm. A broken BaM particle in the Fig. 3.2a inset illustrates the hollow structure. The shell thickness is too thick to be penetrated by a TEM electron beam. Therefore, the contrast on the TEM image of Fig. 3.2c is high, obscuring the hollow structure. We found that alkaline EG can dissolve BaM particles at elevated temperature. By controlling the solvent temperature and heating time, fine hollow mesoporous structured BaM spheres could be obtained. After alkaline EG etching at 185 °C for 7 min, the SEM image of Fig. 3.2b shows that the particle surface becomes rough and holes are detected. The different contrast in every individual particle in the TEM image of Fig. 3.2d shows that a hollow mesoporous structure is well formed after etching, and each spherical particle comprises many primary crystallites. N₂ physisorption measurements show that the surface area of the particles before and after etching is 4.96 m²/g and 20.75 m²/g, respectively. The increased surface area after chemical etching further confirms its porous structure.

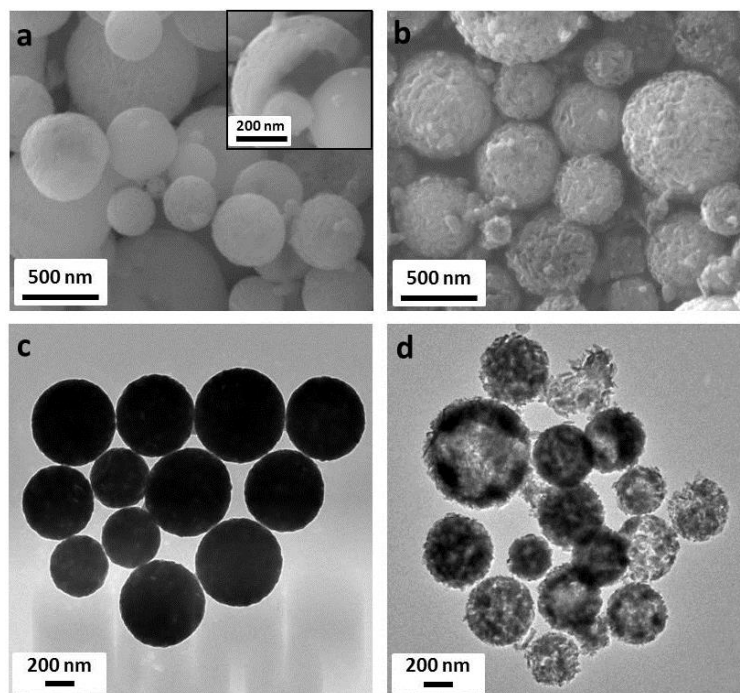


Figure 3.2 SEM and TEM images: (a) SEM image of as-synthesized hollow $\text{BaFe}_{12}\text{O}_{19}$ particles (inset: a broken hollow structured particle); (b) SEM image of hollow mesoporous $\text{BaFe}_{12}\text{O}_{19}$ particles; (c) TEM image of as-synthesized hollow $\text{BaFe}_{12}\text{O}_{19}$ particles; (d) TEM image of hollow mesoporous $\text{BaFe}_{12}\text{O}_{19}$ particles.

The lattice fringes corresponding to the crystallographic plane (110) ($d = 2.98 \text{ \AA}$) of the BaM phase in hollow mesoporous BaM spheres are shown in the high resolution TEM image of Fig. 3.3a. It is well established that crystalline nature is supported by the multiple spot in its diffraction patterns. The corresponding selected area electron diffraction (SAED) pattern (Fig. 3.3b) of the ferrite is dominated by the discrete diffraction spots originating from the crystalline hexagonal BaM phase.

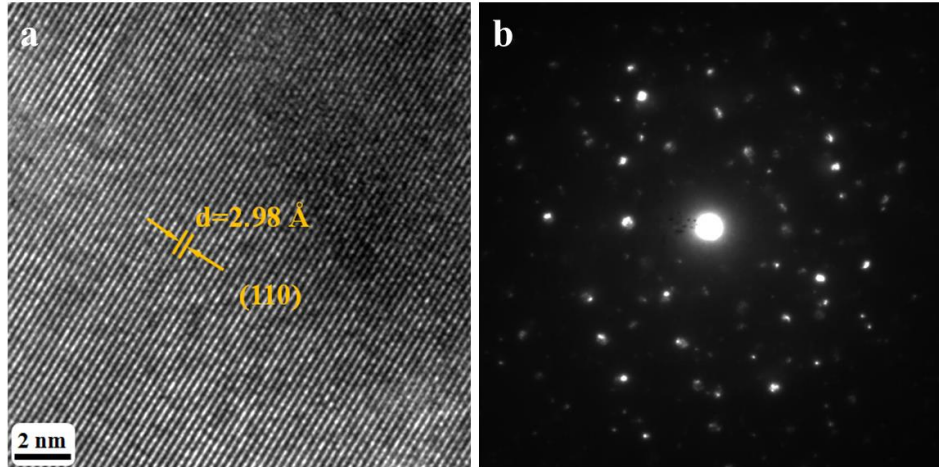


Figure 3.3 (a) High resolution TEM of hollow mesoporous $\text{BaFe}_{12}\text{O}_{19}$ spheres; (b) SAED pattern of hollow mesoporous $\text{BaFe}_{12}\text{O}_{19}$ spheres

Figure 3.4 shows the VSM hysteresis loops of hollow BaM particles before and after EG etching. The samples were measured at room temperature under a magnetic field up to 2 T. The magnetization at 2T of hollow mesoporous BaM particles increases from 50.5 emu/g for the as-synthesized state to 52.5 emu/g for the etched material. This difference could be attributed to balance (for mass weighting) and VSM error. The magnetic coercivity of etched particles decreased from 3800 Oe of before etching to 3600 Oe. These loops indicate that the chemical etching process had little effects on the particles' magnetic properties. The reported magnetic properties match well with BaM synthesized using spray pyrolysis by Ren et al. [35].

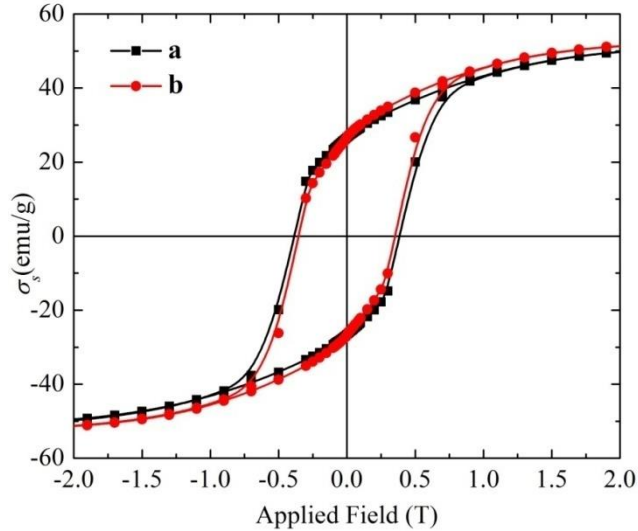


Figure 3.4 Magnetic properties characterization: (a) Magnetic hysteresis loop of as-synthesized hollow $\text{BaFe}_{12}\text{O}_{19}$ particles (before etching); (b) magnetic hysteresis loop of hollow mesoporous $\text{BaFe}_{12}\text{O}_{19}$ particles (after etching).

Crystal structure properties before and after chemical etching were investigated by XRD and the results are shown in Fig. 3.5. There is negligible difference in the XRD patterns of as-synthesized hollow BaM particles in Fig. 3.5a and EG etched hollow mesoporous BaM particles in Fig. 3.5b. Both present a clear pattern corresponding to standard hexagonal phase $\text{BaFe}_{12}\text{O}_{19}$ listed in JCPDS card (NO. 39-1433). Therefore, EG etching has little effect on the crystal structure of the BaM particles. The broad peak widths confirm the crystallite has a small size. The mean primary crystallite size of both BaM particles before and after EG etching was calculated from the X-ray peak width of the (114) plane in 3 pairs of XRD patterns using the Scherrer Equation to be 43.2 nm. The crystallite size and its distribution are also counted and calculated based on TEM images. The corresponding results based on 200 crystallites are shown in Fig. 3.6. The average primary crystallite size is 47.6 nm, and the size distribution is relatively narrow. The average crystallite size from the TEM images accounting (47.6 nm) matches well with the XRD peak width calculation (43.2 nm).

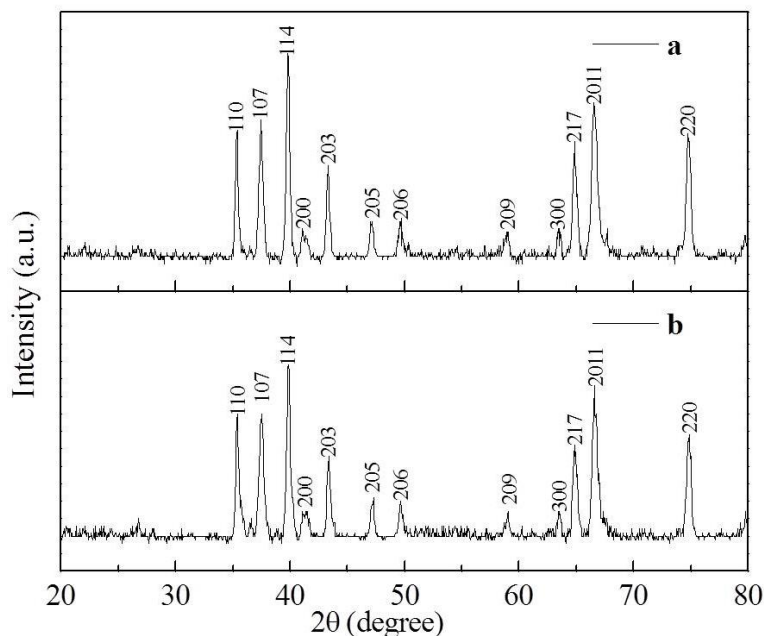


Figure 3.5 Powder XRD patterns. (a) XRD patterns of as-synthesized hollow BaFe₁₂O₁₉ particles (before etching); (b) XRD patterns of hollow mesoporous BaFe₁₂O₁₉ particles (after etching).

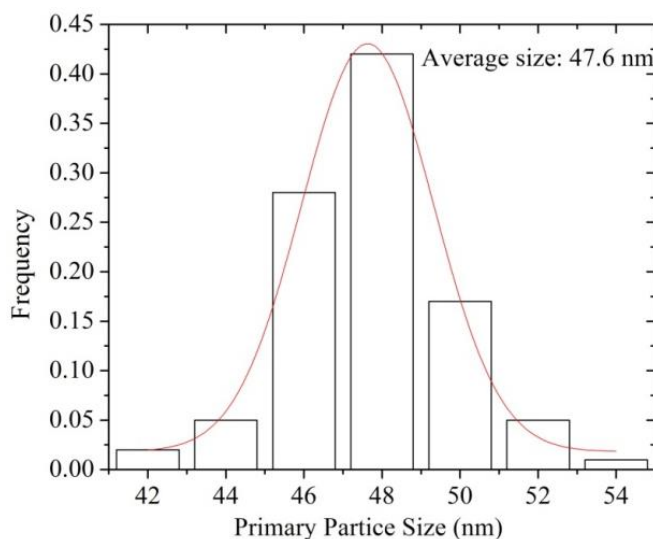


Figure 3.6 The size and size distribution of crystalline in hollow mesoporous BaM spheres.

Based on these characterization results, a formation mechanism for synthesizing hollow mesoporous BaM spheres by alkaline EG etching is proposed. During spray pyrolysis, hollow spherical BaM particles are formed that consist of many small individual crystals [36] with interfaces of mismatched atomic arrangement and lower atomic density. This arrangement leads to a

less efficient atomic packing and less ordered structure, and reduces the stability of the grain boundaries [37]. At the same time, lower density at the atomic scale leads to bigger open space through which atoms can be easily removed by external force [37]. Therefore, when these particles are exposed to alkaline EG at elevated temperature, the grain boundary is etched and removed at first, and small groove are left between grains. These grooves allow EG to diffuse inside to further etch grains. As the grain size gets smaller, gaps appear on the particle surfaces. If the etching process on grain boundaries and crystals is well controlled, hollow mesoporous structure can be formed, and at the same time the spherical shape can be maintained. Figs. 3.7a, b and c show an individual BaM particle after different etching time, and the process can be illustrated as shown in Fig. 3.7d. The particle heated for 7 min (Fig. 3.7c) has higher porosity than the particle heated for 5 min (Fig. 3.7b). Therefore, the particle porosity can be controlled by the heating time. Longer heating time leads to higher porosity.

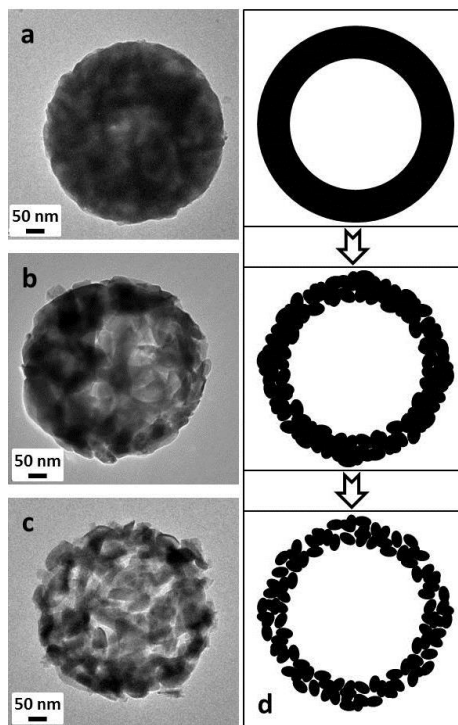


Figure 3.7 The step-by-step EG etching process on an individual hollow BaM sphere: (a) 0 min etching; (b) 5 min etching; (c) 7 min etching; d) a schematic of step etching.

Besides porosity, the particle size is another factor to determine the etching time. Larger particles require a longer etching time. Because of the wide size distribution, some smaller particles (< 200 nm) can be over-etched in this process, and the spherical shape could be destroyed, as shown in Fig. 3.2d. However, most of the particles are well etched with a hollow mesoporous structure.

3.1.4. Conclusions

In summary, this presented facile method has successfully demonstrated the fabrication of hollow mesoporous BaM spheres by a template-free chemical etching process. The hollow particles are synthesized by spray pyrolysis. The mesoporous structure is obtained by exposing hollow BaM spheres to alkaline EG at 185 °C. The porosity can be regulated by heating time, and the magnetic properties and crystal structure are little affected in the etching process. The mechanism is explained by grain boundary etching. The present method and mechanism may be also extended to synthesize a mesoporous structure of other metal ferrites.

3.2. EG Assisted Spray Pyrolysis for the Synthesis of Hollow $\text{BaFe}_{12}\text{O}_{19}$ Spheres

3.2.1. Introduction

Hexagonal barium ferrite ($\text{BaFe}_{12}\text{O}_{19}$) has been of a great interest because of its high magnetic anisotropy, low cost, and high chemical and physical stability. Various preparation methods have been proposed to synthesize $\text{BaFe}_{12}\text{O}_{19}$ particles, such as ceramic [38-40], co-precipitation [41-43] and spray pyrolysis [33,34] methods. Compared with other synthesis techniques, spray pyrolysis has several advantages including simple operation, high purity, excellent control of chemical uniformity and stoichiometry in mixed oxide systems, and continuous operation [44]. The product properties are affected by factors such as carrier gas type and flow rate, pyrolysis temperature, concentration of the spray solution and types of organic additives [45].

An organic additive is well known to produce a large amount of gas inside the droplet while flowing through the high temperature reactor and makes the products hollow [45]. Citric acid, ethylene diaminetetraacetic acid (EDTA), ethylene glycol (EG), polyethylene glycol (PEG) and ethanol alone or in combination have been used in organic-assisted spray pyrolysis to synthesize metal oxides, and different organics lead to different morphologies of the products [8,34,46-52]. EG-assisted spray pyrolysis has never been applied to BaM synthesis, and previous research of organic-assisted spray pyrolysis mainly focuses on different reaction temperatures [8,34,46-52]; the effects of organic concentration are rarely investigated. In this study, we applied EG-assisted spray pyrolysis to BaFe₁₂O₁₉ particle synthesis and studied the effects of EG concentration in the precursor solution on product morphology, crystallization and magnetic properties.

3.2.2. Experimental

3.2.2.1. Synthesis of hollow BaFe₁₂O₁₉ spheres

The synthesis of spherical BaFe₁₂O₁₉ particles is based on a previous report with little modification [53]. Generally, precursors of Fe(NO₃)₃·9H₂O (4.84g) and Ba(NO₃)₂ (0.27 g) were dissolved in 100 mL solvent consisting of DI H₂O and ethylene glycol (EG). The volume percentage of EG was controlled to 10, 20 and 30%. The solution was then transferred to an ultrasonic nebulizer (Intertek, 1.7 MHz) to generate fine and uniform liquid droplets. In air pulled by building vacuum at the end of the system, the droplets flowed through a tube furnace (Length: 1.0 m; Inner diameter: 0.08 m) at 1000 °C to thermally decompose the precursors and produce BaFe₁₂O₁₉ particles. The flow rate was controlled to 5 L/min. The product was then cooled down by a heat exchanger, and finally collected by a fiber filter.

3.2.2.2. Powder Characterization

The measurement of X-ray diffraction (XRD) patterns was carried out by a Bruker D8 diffractometer using Cu-K α radiation ($\lambda=1.541 \text{ \AA}$). Transmission electron microscopy (TEM, TECNAI FEI 20) was used to analyze the particle size and morphology. Magnetic properties were checked at room temperature with a vibrating sample magnetometer (VSM, Microsense 3473-70) in an applied field up to 2 T.

3.2.3. Results and discussion

Figure 3.8 shows TEM images of BaFe₁₂O₁₉ particles synthesized from 10, 20 and 30 vol% EG solutions. The low contrast of the particle surface indicates that most of the TEM electron beam passed through the particles, and confirms their hollow structure with a thin shell. The formation of a hollow structure can be explained by the temperature and concentration gradient along the radial direction of spray droplets in the pyrolysis process. Higher temperature on the droplet surface results in evaporation of the solvent and precursor concentration increasing within the droplet. Once the concentration is higher than the saturation concentration, the precursors precipitate on the droplet surface, thereby, forming a hollow structure [50]. Low magnification TEM images of Figs. 3.8a, d and f show that the particles are submicron size, and the size distribution is wide. EG concentration does not have an obvious effect on particle size, however, it does have obvious effects on particle morphology. All of the particles are hollow spheres at 10 vol% EG. When the concentration increases to 20 and 30 vol%, crystal pieces are mixed with hollow spheres in the products and higher EG concentration leads to a bigger amount of crystal pieces. During the pyrolysis process, high EG concentrations will burn and lead to too much pressure inside the droplet that we assume breaks the structure. Particles from different EG concentrations in Figs. 3.8b, e and h are spherical and hollow, and consist of many primary particles.

The primary particles bridge with each other and form condensed hollow structured particles, as shown in Figs. 3.8c, f and i. Furthermore, the primary particle size from 10 vol% EG (Fig. 3.8c, ~ 20 nm) is smaller than those from 20 and 30 vol% EG (Figs. 3.8f and i, ~40 nm), and the reason is still unknown.

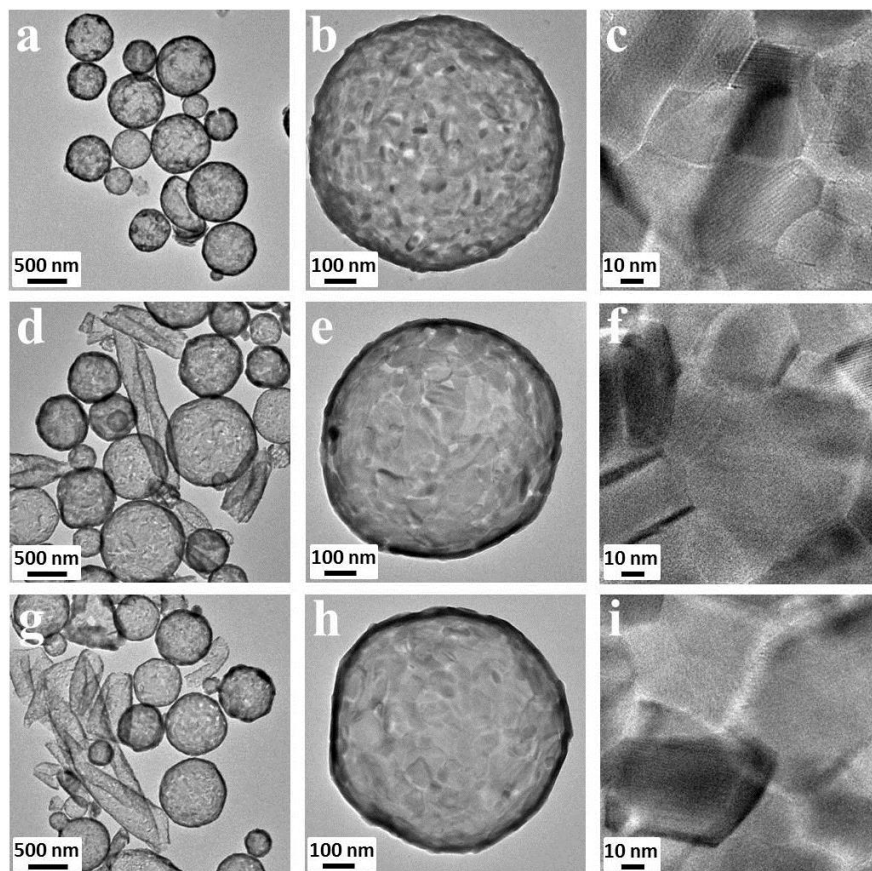


Figure 3.8 TEM images of hollow $\text{BaFe}_{12}\text{O}_{19}$ spheres. (a), (b), (c): synthesized from 10 vol% EG; (d), (e), (f): synthesized from 20 vol% EG; (g), (h), (i): synthesized from 30 vol% EG.

Figure 3.9 shows the X-ray diffraction patterns of the hollow $\text{BaFe}_{12}\text{O}_{19}$ spheres synthesized from different EG concentrations. All the samples present a clear pattern corresponding to standard hexagonal phase $\text{BaFe}_{12}\text{O}_{19}$ listed in JCPDS card (NO. 39-1433). The mean primary crystallite size of these three samples was calculated from Figs. 3.9a, b and c using the Scherrer Equation to be 25.3 nm, 42.7 nm and 46.1 nm, matching well with the TEM images of Figs. 3.8c, f and i. It is known that post annealing is necessary to further crystallize the products from spray

pyrolysis, since the residence time inside the furnace is too short to achieve a complete crystallization [34,46,48]. Interestingly, the particles produced in this research are well crystallized, especially at higher EG concentration. This could be attributed to the heat produced from the combustion of EG inside the furnace. At higher EG concentration, more heat is produced and the products are better crystallized. Therefore, the peak intensity becomes higher with increased EG concentration, as shown in XRD patterns in Fig. 2.

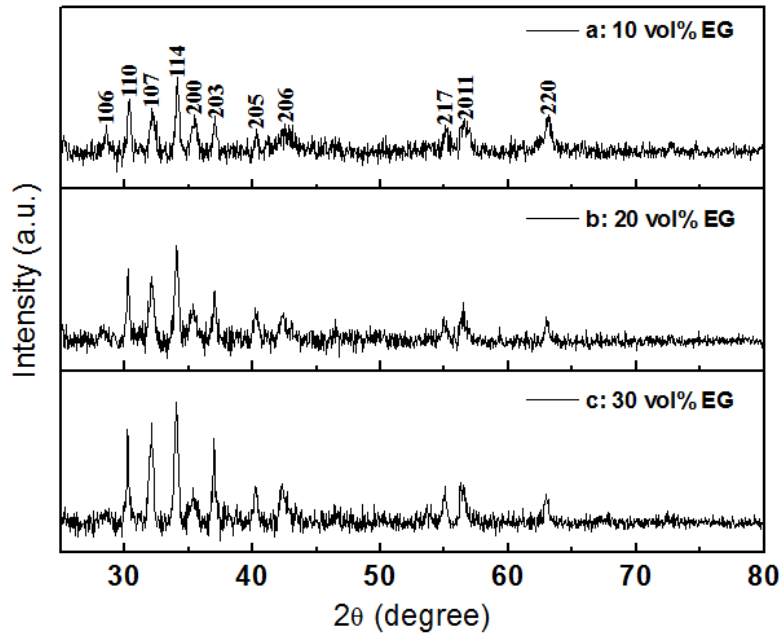


Figure 3.9 X-ray diffraction patterns of hollow $\text{BaFe}_{12}\text{O}_{19}$ spheres synthesized from different concentrations of EG.

The magnetic hysteresis loops of hollow $\text{BaFe}_{12}\text{O}_{19}$ spheres synthesized from different EG concentrations are shown in Fig. 3.10. The typical hard magnetic properties match well with pure hexagonal phase $\text{BaFe}_{12}\text{O}_{19}$ in XRD patterns of Fig. 3.9. The saturation magnetization is 62 emu/g and coercivity is 3155 Oe when the EG is 10 vol%. With concentration increasing, the saturation magnetization decreases while the magnetic coercivity increases, arriving at 49 emu/g and 4284 Oe when the EG is 30 vol%. A short residence time usually leads to incomplete combustion of organics, leaving carbon in the products [54]. Higher EG concentration also leaves a

larger amount of carbon in the products, contributing as a non-magnetic phase to the particles, leading to decreased magnetization. Figures. 3.11a, b and c show the SEM images of hollow $\text{BaFe}_{12}\text{O}_{19}$ spheres synthesized from different EG concentrations. The residual carbon and its quantity are confirmed by EDX spectroscopy, as shown in Figs. 3.11d, e and f, and the scanning time of all samples is controlled to one minute. The red dots confirm the existence of carbon, and the dot density represents the quantity. With increasing EG concentration, the density of the red dots increases, indicating a larger amount of residual carbon. The increased coercivity in Fig. 3.10 is due to better crystallization, which is in good agreement with the increased XRD peak intensity Fig. 3.9.

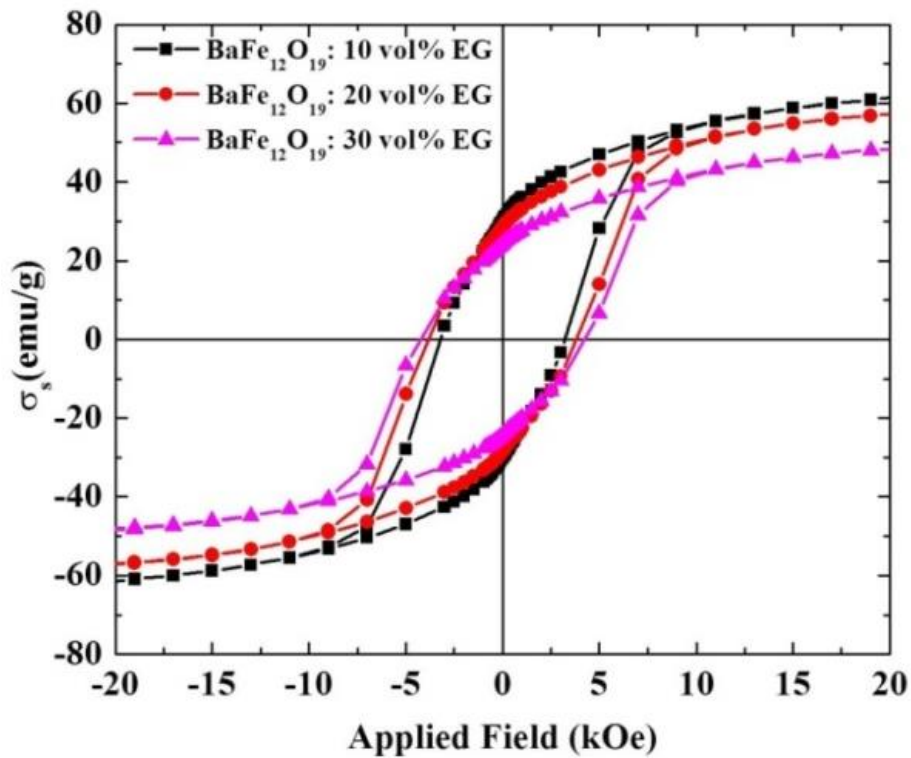


Figure 3.10 Magnetic hysteresis loops of hollow $\text{BaFe}_{12}\text{O}_{19}$ spheres synthesized from different concentration of EG.

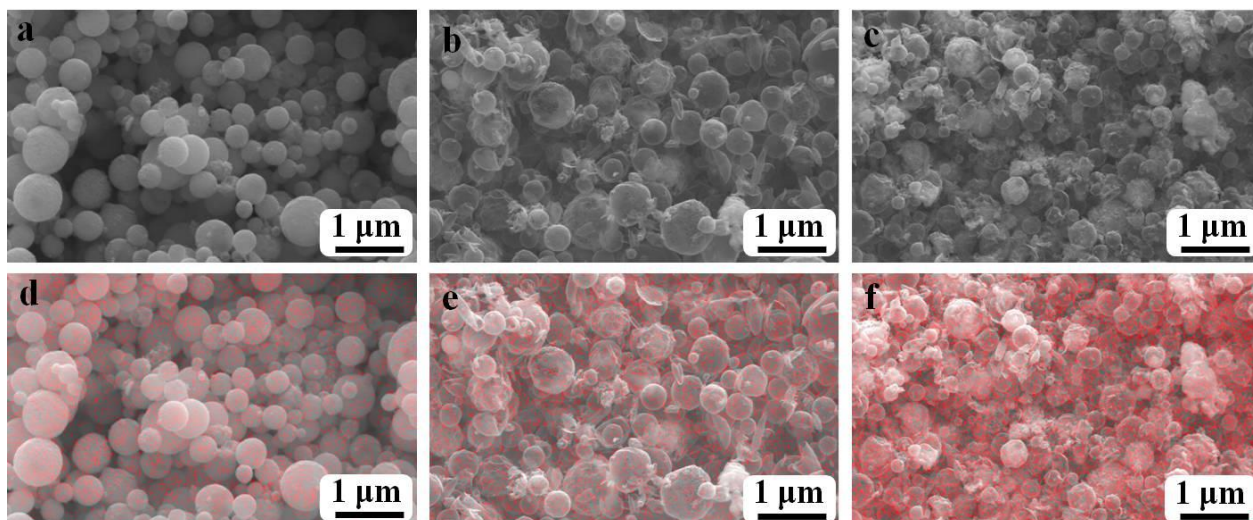


Figure 3.11 SEM images (a, b, c) and their corresponding carbon EDX spectroscopy (d, e and f) of hollow BaFe₁₂O₁₉ spheres synthesized from 10 vol%, 20 vol% and 30 vol% EG.

3.2.4. Conclusions

Hollow spherical BaFe₁₂O₁₉ particles were synthesized by spray pyrolysis from different volume concentration of EG in DI H₂O. Increasing EG concentration leads to bigger primary particle size and more broken particles. Also, the degree of crystallinity and coercivity increase, while the saturation magnetization decreases.

3.3. Synthesis and Characterization of Worm-shape BaFe₁₂O₁₉ Nanoparticles

3.3.1. Introduction

Barium hexagonal ferrite (BaFe₁₂O₁₉ or BaM) is a popular hard magnetic material and has been widely used as permanent magnets, microwaves absorbers [55-57], recording mediums [58,59] and floppy disks [60,61]. These wide applications are not only because of its promising magnetic properties such as high Curie temperature (T_c), high coercive force (H_c) and high magnetic anisotropy constant (K), but also due to its low production cost and high chemical and physical stability.

Several methods have been proposed and developed to synthesize BaM particles. The commonly used methods include sol-gel [62-66], coprecipitation [67-70], spray pyrolysis

[48,71,72], ceramic method [38,73,74], and reverse microemulsion [65,75,76]. Different shape of BaM particles can be obtained from different methods. For example, spherical shape of BaM particles can be synthesized from spray pyrolysis, and hexagonal shape can be synthesized from ceramic method. Irregular shape of BaM nanoparticles was synthesized through reverse microemulsion by Xu et al. [77]. However, in this report, we used a similar method of reverse microemulsion, and synthesize worm-shape BaM nanoparticles. To the best of our survey, this shape of BaM nanoparticles is never reported before. Considering their uniform size and shape, worm-shape BaM nanoparticles show great potentials as a magnetic recording medium.

3.3.2. Experimental

3.3.2.1. Materials synthesis

The synthesis procedures can be simplified as Fig. 3.12. In the microemulsion system, cetyltrimethylammonium bromide (CTAB) is used as surfactant, n-butanol is used as co-surfactant, and cyclohexene as solvent. In a typical experiment, microemulsion I consisted of 10 mL 1-butanol, 100 mL cyclohexane and 10 mL of 0.4 g/mL $\text{Fe}(\text{NO}_3)_3$ and 0.022 g/mL $\text{Ba}(\text{NO}_3)_2$ with $R = V(\text{aqueous}) : V(\text{oil}) = 1:11$. With the same value of R, microemulsion II contained 10 mL 1-butanol, 100 mL cyclohexane and 10 mL of 0.15 g/mL NaOH and 0.016 g/mL NaCO_3 , stirring for 10 min to form a homogenous emulsion. Microemulsion I and II were then mixed and magnetically stirred for 2 hours. The products were separated with centrifuge and washed with ethanol for 3 times to remove the residual surfactant and solvents. The washed particles were dried in oven at 80 °C for 5 hours, followed by thoroughly grinding. These ground fine particles were pre-annealed at 400 °C for 2 hours, with heating rate of 5 °C/min, and finally annealed at 760 °C for 2 hours with same heating rate. The annealing process was conducted in atmospheric

environment. The finally products were washed with diluted acid to remove secondary phases and dried for characterization.

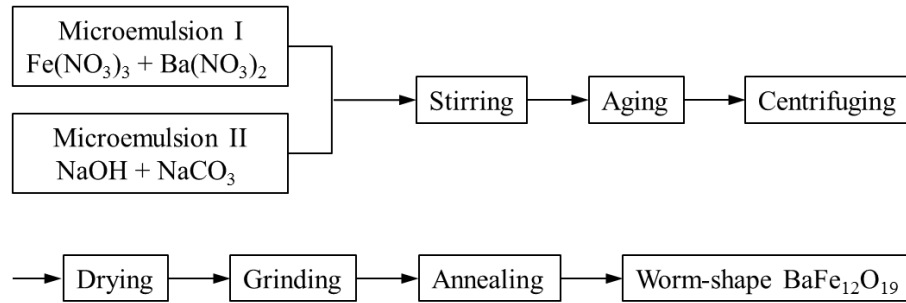


Figure 3.12 Preparation procedures for worm-shape BaM particles by reverse microemulsion technique.

3.3.2.2. Characterization

The measurement of X-ray diffraction (XRD) patterns was carried out by Bruker D8 diffractometer using Cu-K α radiation ($\lambda=1.5406 \text{ \AA}$). Transmission electron microscopy (TEM, TECNAI FEI 20) was used to analyze the particle size and morphology. Magnetic properties were checked at room temperature with a vibrating sample magnetometer (VSM, Microsense 3473-70) in an applied field up 2 T.

3.3.3. Results and discussion

TEM images in Fig. 3.13 show worm-shape BaM nanoparticles under low and high magnification. It can be observed from Fig. 3.13a that the shape of particles is uniform, and particles are agglomerated. Each single particle is consisted of a few smaller units, ranging from 3 to 7, with thickness of $\sim 10 \text{ nm}$. These single units stack together and form a worm-shape particle, as shown in Fig. 3.13b.

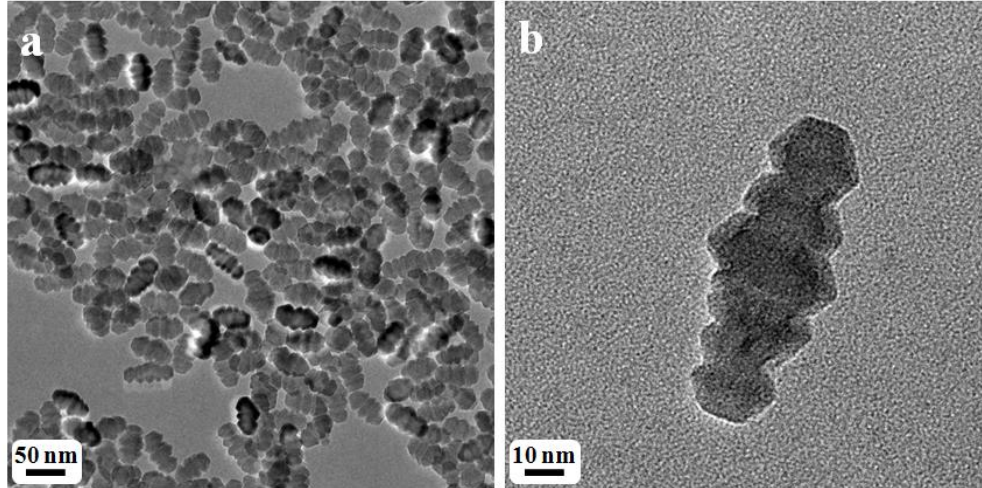


Figure 3.13 TEM images of worm-shape BaM nanoparticles: (a) low magnification; (b) high magnification.

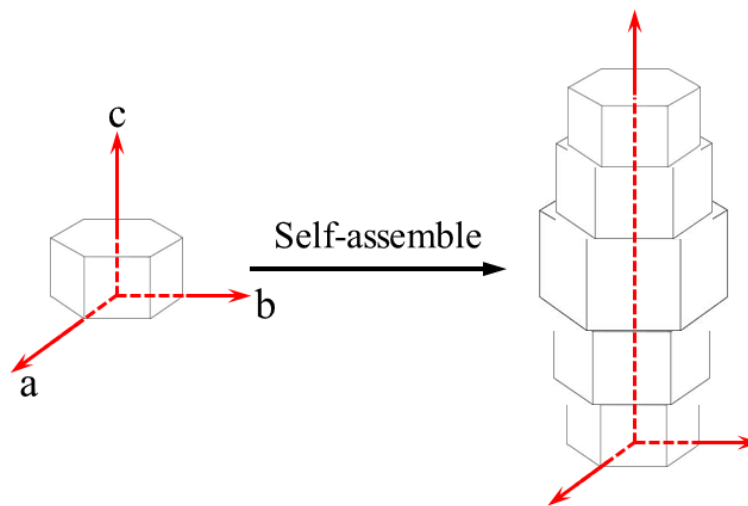


Figure 3.14 Proposed self-assembly process for the formation of worm-shape BaM nanoparticles.

To better explain the formation mechanism of worm-shape BaM nanoparticles, a self-assembly process is proposed, as shown in Fig. 3.14. It is well known that the barium ferrite has hexagonal crystal structure with hexagonal shape as its thermally stable state. In a hexagonal shape BaM particle, the c axis is magnetically easy axis. When these single particles are formed, they tend to be stacked along the c axis. These stacks are further annealed at high temperature and form a worm-shape particle.

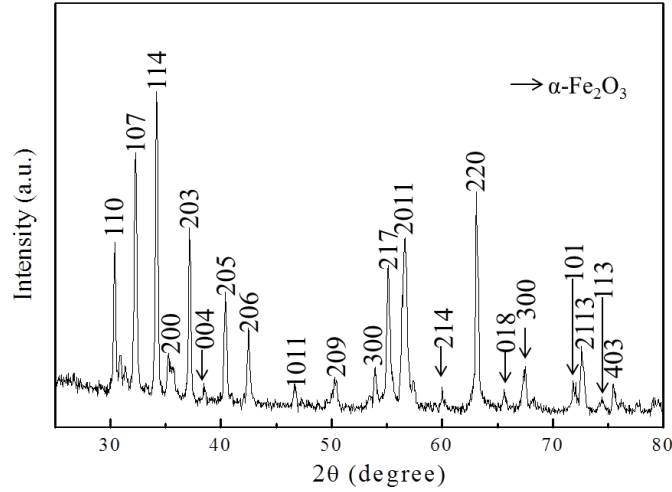


Figure 3.15 X-ray diffraction patterns of worm-shape BaM nanoparticles.

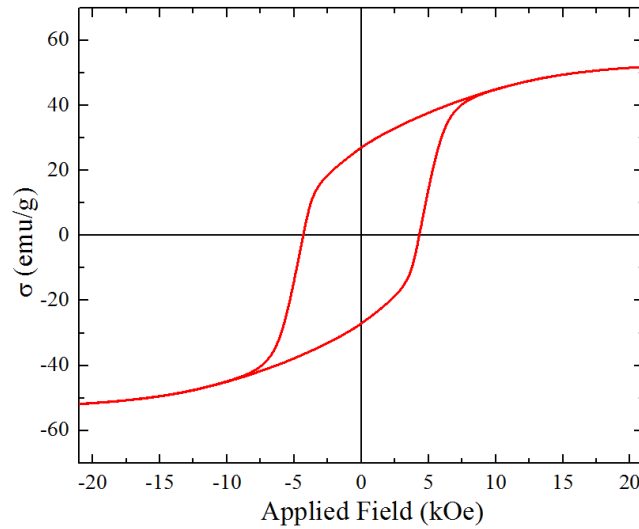


Figure 3.16 Magnetic hysteresis loop of worm-shape BaM nanoparticles.

Figure 3.15 shows the XRD patterns of worm-shape BaM nanoparticles. Hexagonal barium ferrite phase is well formed, and hematite ($\alpha\text{-Fe}_2\text{O}_3$) phase mixed inside. Figure 3.16 shows the magnetic hysteresis loop of worm-shape BaM nanoparticles with the magnetization of 52 emu/g and coercivity of 4735 Oe. This magnetization is lower than typical hexagonal barium ferrite of 60 emu/g, which could be attributed to $\alpha\text{-Fe}_2\text{O}_3$ mixed in the BaM nanoparticles.

3.3.4. Conclusions

Worm-shape hexagonal barium ferrite is synthesized by a reverse microemulsion method and a post-annealing. Each single worm-shape particle is consisted of 3 to 7 small units. The formation mechanism is explained with self-assembly process. The magnetization is lower than normal case because of containing α -Fe₂O₃, which is confirmed by XRD patterns. This product can be potentially used for solid-state device applications [79-82].

3.4. References

1. Yu, J. G., Yu, X. X., Huang, B. B., Zhang, X. Y. & Dai, Y. Hydrothermal Synthesis and Visible-Light Photocatalytic Activity of Novel Cage-Like Ferric Oxide Hollow Spheres. *Crystal Growth & Design*, **9**, 1474-1480 (2009).
2. Guo, F. Q., Zhang, Z. F., Li, H. F., Meng, S. L. & Li, D. Q. A Solvent Extraction Route for CaF₂ Hollow Spheres. *Chemical Communications*, **46**, 8237-8239 (2010).
3. Yin, Y. D. *et al.* Formation of Hollow Nanocrystals through the Nanoscale Kirkendall Effect. *Science*, **304**, 711-714 (2004).
4. Liu, J., Liu, F., Gao, K., Wu, J. S. & Xue, D. F. Recent Developments in the Chemical Synthesis of Inorganic Porous Capsules. *Journal of Materials Chemistry*, **19**, 6073-6084 (2009).
5. Sharma, M., Das, D., Baruah, A., Jain, A. & Ganguli, A. K. *Design of Porous Silica Supported Tantalum Oxide Hollow Spheres Showing Enhanced Photocatalytic Activity*. (2014).
6. Cao, S. W., Zhu, Y. J., Ma, M. Y., Li, L. & Zhang, L. Hierarchically Nanostructured Magnetic Hollow Spheres of Fe₃O₄ and Gamma-Fe₂O₃: Preparation and Potential Application in Drug Delivery. *Journal of Physical Chemistry C*, **112**, 1851-1856 (2008).
7. Lou, X. W., Wang, Y., Yuan, C. L., Lee, J. Y. & Archer, L. A. Template-Free Synthesis of SnO₂ Hollow Nanostructures with High Lithium Storage Capacity. *Advanced Materials*, **18**, 2325- (2006).
8. Yin, X. M. *et al.* SnO₂ Monolayer Porous Hollow Spheres as a Gas Sensor. *Nanotechnology*, **20** (2009).
9. Fei, J. B. *et al.* Controlled Preparation of MnO₂ Hierarchical Hollow Nanostructures and Their Application in Water Treatment. *Advanced Materials*, **20**, 452-458 (2008).
10. Caruso, F., Caruso, R. A. & Mohwald, H. Nanoengineering of Inorganic and Hybrid Hollow Spheres by Colloidal Templating. *Science*, **282**, 1111-1114 (1998).
11. Iler, R. K. Multilayers of Colloidal Particles. *Journal of Colloid and Interface Science*, **21**, 569-577 (1966).

12. Eerenstein, W., Mathur, N. D. & Scott, J. F. Multiferroic and Magnetoelectric Materials. *Nature*, **442**, 759-765 (2006).
13. Ma, M. Y., Zhu, Y. J., Li, L. & Cao, S. W. Nanostructured Porous Hollow Ellipsoidal Capsules of Hydroxyapatite and Calcium Silicate: Preparation and Application in Drug Delivery. *Journal of Materials Chemistry*, **18**, 2722-2727 (2008).
14. Buchold, D. H. M. & Feldmann, C. Nanoscale Gamma-AlO(OH) Hollow Spheres: Synthesis and Container-Type Functionality. *Nano Letters*, **7**, 3489-3492 (2007).
15. Feng, Z. G. *et al.* A Facile Route to Hollow Nanospheres of Mesoporous Silica with Tunable Size. *Chemical Communications*, 2629-2631 (2008).
16. Yu, X. L. *et al.* Nanometer-Sized Copper Sulfide Hollow Spheres with Strong Optical-Limiting Properties. *Advanced Functional Materials*, **17**, 1397-1401 (2007).
17. Li, H. X. *et al.* Mesoporous Titania Spheres with Tunable Chamber Structure and Enhanced Photocatalytic Activity. *Journal of the American Chemical Society*, **129**, 8406-8410 (2007).
18. Liu, B. & Zeng, H. C. Mesoscale Organization of CuO Nanoribbons: Formation of "Dandelions". *Journal of the American Chemical Society*, **126**, 8124-8125 (2004).
19. Rogach, A. L. *et al.* Light-Emitting Diodes with Semiconductor Nanocrystals. *Angewandte Chemie-International Edition*, **47**, 6538-6549 (2008).
20. Skrabalak, S. E. *et al.* Gold Nanocages: Synthesis, Properties, and Applications. *Accounts of Chemical Research*, **41**, 1587-1595 (2008).
21. Sandberg, L. I. C., Gao, T., Jelle, B. P. & Gustavsen, A. Synthesis of Hollow Silica Nanospheres by Sacrificial Polystyrene Templates for Thermal Insulation Applications. *Advances in Materials Science and Engineering* (2013).
22. Ma, H. *et al.* Nest-Like Silicon Nanospheres for High-Capacity Lithium Storage. *Advanced Materials*, **19**, 4067-4072 (2007).
23. Shan, Z. W. *et al.* Ultrahigh Stress and Strain in Hierarchically Structured Hollow Nanoparticles. *Nature Materials*, **7**, 947-952 (2008).
24. Shin, J. M. *et al.* Hollow Manganese Oxide Nanoparticles as Multifunctional Agents for Magnetic Resonance Imaging and Drug Delivery. *Angewandte Chemie-International Edition*, **48**, 321-324 (2009).
25. Qing, X. T., Yue, X. X., Wang, B. & Lu, Y. Facile Synthesis of Size-Tunable, Multilevel Nanoporous Fe₃O₄ Microspheres for Application in Electromagnetic Wave Absorption. *Journal of Alloys and Compounds*, **595**, 131-137 (2014).
26. Xiong, Q. Q. *et al.* Ascorbic Acid-Assisted Synthesis of Cobalt Ferrite (CoFe₂O₄) Hierarchical Flower-Like Microspheres with Enhanced Lithium Storage Properties. *Journal of Power Sources*, **256**, 153-159 (2014).
27. Assar, S. T., Abosheiasha, H. F. & El Nimr, M. K. Comparison Study of the Magnetic Permeability and Dc Conductivity of Co-Ni-Li Ferrite Nanoparticles and Their Bulk Counterparts. *Journal of Magnetism and Magnetic Materials*, **354**, 1-6 (2014).

28. Hou, Y., Li, X. Y., Zhao, Q. D. & Chen, G. H. ZnFe₂O₄ Multi-Porous Microbricks/Graphene Hybrid Photocatalyst: Facile Synthesis, Improved Activity and Photocatalytic Mechanism. *Applied Catalysis B-Environmental*, **142**, 80-88 (2013).
29. Ji, K. M. *et al.* One-Pot Hydrothermal Preparation and Catalytic Performance of Porous Strontium Ferrite Hollow Spheres for the Combustion of Toluene. *Journal of Molecular Catalysis A-Chemical*, **370**, 189-196 (2013).
30. Li, Z. M. *et al.* General Synthesis of Homogeneous Hollow Core-Shell Ferrite Microspheres. *Journal of Physical Chemistry C*, **113**, 2792-2797 (2009).
31. Patterson, A. L. The Scherrer Formula for X-Ray Particle Size Determination. *Physical Review*, **56**, 978-982 (1939).
32. Li, S. *et al.* Hierarchical Porous Metal Ferrite Ball-in-Ball Hollow Spheres: General Synthesis, Formation Mechanism, and High Performance as Anode Materials for Li-ion Batteries. *Nano Research*, doi:10.1007/s12274-014-0474-3 (2014).
33. Cabanas, M. V., Gonzalezcalbet, J. M. & Valletregi, M. Synthesis of Barium Hexaferrite by Pyrolysis of an Aerosol. *Journal of Materials Research*, **9**, 712-716 (1994).
34. Gonzalez-Carreno, T., Morales, M. P. & Serna, C.J. Barium Ferrite Nanoparticles Prepared Directly by Aerosol Pyrolysis. *Materials Letters*, **43**, 97-101 (2000).
35. Ren, P., Guan, J. G. & Cheng, X. D. Influence of Heat Treatment Conditions on the Structure and Magnetic Properties of Barium Ferrite BaFe₁₂O₁₉ Hollow Microspheres of Low Density. *Materials Chemistry and Physics*, **98**, 90-94 (2006).
36. Senzaki, Y., Caruso, J., Hampdensmith, M. J., Kodas, T. T. & Wang, L. M. Preparation of Strontium Ferrite Particles by Spray-Pyrolysis. *Journal of the American Ceramic Society*, **78**, 2973-2976 (1995).
37. French, D. *Metallurgical Failures in Fossil Fired Boilers*. (Wiley, 1993).
38. Lisjak, D. The Low-Temperature Sintering of M-Type Hexaferrites. *Journal of the European Ceramic Society*, **32**, 3351-3360 (2012).
39. Zhang, H. J., Jia, X. L., Ya, X. & Zhang, L. Y. Preparation, Dielectric and Magnetic Properties of Barium-Ferrite-Containing Microcrystalline Glass Ceramic by Citrate Sol-Gel Process. *High-Performance Ceramics Iii, Pts 1 and 2*, **280-283**, 457-460 (2005).
40. Matutes-Aquino, J. A. *et al.* Synthesis and Characterization of Nickel Ferrite-Barium Titanate Ceramic Composites. *Integrated Ferroelectrics*, **101**, 22-28 (2008).
41. Janasi, S. R., Rodrigues, D., Landgraf, F. J. G. & Emura, M. Magnetic Properties of Coprecipitated Barium Ferrite Powders as a Function of Synthesis Conditions. *Ieee Transactions on Magnetics*, **36**, 3327-3329 (2000).
42. Janasi, S. R., Emura, M., Landgraf, F. J. G. & Rodrigues, D. The Effects of Synthesis Variables on the Magnetic Properties of Coprecipitated Barium Ferrite Powders. *Journal of Magnetism and Magnetic Materials*, **238**, 168-172 (2002).
43. Makled, M. H. *et al.* Effect of Particle Size and Its Distribution on the Fabrication and Magnetic Properties of Barium Ferrite Powders Prepared from Coprecipitated Precursors. *Journal of the Ceramic Society of Japan*, **112**, 200-203 (2004).

44. Kang, H. S., Kang, Y. C., Park, H. D. & Shul, Y. G. Morphology of Particles Prepared by Spray Pyrolysis from Organic Precursor Solution. *Materials Letters*, **57**, 1288-1294 (2003).
45. Jung, D. S., Bin Park, S. & Kang, Y. C. Design of Particles by Spray Pyrolysis and Recent Progress in Its Application. *Korean Journal of Chemical Engineering*, **27**, 1621-1645 (2010).
46. Kang, H. S., Sohn, J. R., Kang, Y. C., Jung, K. Y. & Park, S. B. The Characteristics of Nano-Sized Gd-Doped CeO₂ Particles Prepared by Spray Pyrolysis. *Journal of Alloys and Compounds*, **398**, 240-244 (2005).
47. Lee, K. K., Kang, Y. C., Jung, K. Y. & Kim, J. H. Preparation of Nano-Sized BaTiO₃ Particle by Citric Acid-Assisted Spray Pyrolysis. *Journal of Alloys and Compounds*, **395**, 280-285 (2005).
48. Kim, M. H., Jung, D. S., Kang, Y. C. & Choi, J. H. Nanosized Barium Ferrite Powders Prepared by Spray Pyrolysis from Citric Acid Solution. *Ceramics International*, **35**, 1933-1937 (2009).
49. Ju, S. H., Kim, D. Y., Jo, E. B. & Kang, Y. C. LiMn₂O₄ Particles Prepared by Spray Pyrolysis from Spray Solution with Citric Acid and Ethylene Glycol. *Journal of Materials Science*, **42**, 5369-5374 (2007).
50. Zhong, K., Peabody, G., Glicksman, H. & Ehrman, S. Particle Generation by Cosolvent Spray Pyrolysis: Effects of Ethanol and Ethylene Glycol. *Journal of Materials Research*, **27**, 2540-2550 (2012).
51. Choi, S. H., Ko, Y. N., Lee, J. K. & Kang, Y. C. Dielectric Properties of Nano-Sized Ba_{0.7}Sr_{0.3}TiO₃ Powders Prepared by Spray Pyrolysis. *Ceramics International*, **38**, 4029-4033 (2012).
52. Jung, D. S., Koo, H. Y., Han, J. M. & Kang, Y. C. Micrometre-Sized Zinc Silicate Phosphor Powders Prepared Using a Size-Controllable Droplet Generator from a Polyethylene Glycol Spray Solution. *Journal of Ceramic Processing Research*, **10**, 423-427 (2009).
53. Messing, G. L., Zhang, S. C. & Jayanthi, G. V. Ceramic Powder Synthesis by Spray-Pyrolysis. *Journal of the American Ceramic Society*, **76**, 2707-2726 (1993).
54. Cho, J. S. & Rhee, S. H. Formation Mechanism of Nano-Sized Hydroxyapatite Powders through Spray Pyrolysis of a Calcium Phosphate Solution Containing Polyethylene Glycol. *Journal of the European Ceramic Society*, **33**, 233-241 (2013).
55. Ozah, S. & Bhattacharyya, N. S. Nanosized Barium Hexaferrite in Novolac Phenolic Resin as Microwave Absorber for X-band Application. *Journal of Magnetism and Magnetic Materials*, **342**, 92-99(2013).
56. Singh, C., Bindra-Narang, S., Hudhara, I. S., Sudheendran, K. & Raju, K. C. J. Microwave and Electrical Behavior of Co²⁺ and Ru⁴⁺ Ions Substituted Ba-Sr Sintered Ferrite. *Journal of Electroceramics*, **27**, 120-125(2011).

57. Tehrani, M. K., Ghasemi, A., Moradi, M. & Alam, R. S. Wideband Electromagnetic Wave Absorber Using Doped Barium Hexaferrite in Ku-Band. *Journal of Alloys and Compounds*, **509**, 8398-8400(2011).
58. Jalli, J. *et al.* Conversion of Nano-Sized Spherical Magnetite to Spherical Barium Ferrite Nanoparticles for High Density Particulate Recording Media. *IEEE Transactions on Magnetics*, **45**, 3590-3593 (2009).
59. Lee, J. *et al.* Modeling of the Write and Read Back Performances of Hexagonal Ba-Ferrite Particulate Media for High Density Tape Recording. *Journal of Magnetism and Magnetic Materials*, **322**, 3869-3875(2010).
60. Imamura, M., Ito, T., Fujiki, M. & Kubota, H. Barium Ferrite Perpendicular Recording Floppy Disk. *Toshiba Review*, 18-22 (1985).
61. Ohtani, A. *et al.* Synthesis and Properties of High-Molecular-Weight Soluble Polyaniline and Its Application to the 4MB-Capacity Barium Ferrite Floppy Disks Antistatic Coating. *Synthetic Metals*, **57**, 3696-3701(1993).
62. Ali, I., Islam, M. U., Awan, M. S. & Ahmad, M. Effects of Ga-Cr Substitution on Structural and Magnetic Properties of Hexaferrite (BaFe₁₂O₁₉) Synthesized by Sol-Gel Auto-Combustion Route. *Journal of Alloys and Compounds*, **547**, 118-125(2013).
63. Ashiq, M. N., Ehsan, M. F., Iqbal, M. J. & Najam-ul-Haq, M. Role of Zr-Co Substitution at Iron Site on Structural, Magnetic and Electrical Properties of Sr-Hexaferrites Nanomaterials Synthesized by the Sol-Gel Combustion Method. *Journal of Magnetism and Magnetic Materials*, **332**, 93-97(2013).
64. Jazirehpour, M., Shams, M. H. & Khani, O. Modified Sol-Gel Synthesis of Nanosized Magnesium Titanium Substituted Barium Hexaferrite and Investigation of the Effect of High Substitution Levels on the Magnetic Properties. *Journal of Alloys and Compounds*, **545**, 32-40(2012).
65. Jotania, R. B., Khomane, R. B., Chauhan, C. C., Menon, S. K. & Kulkarni, B. D. Synthesis and Magnetic Properties of Barium-Calcium Hexaferrite Particles Prepared by Sol-Gel and Microemulsion Techniques. *Journal of Magnetism and Magnetic Materials*, **320**, 1095-1101(2008).
66. Liu, T. *et al.* Research on the Magnetic Properties of BaFe_xO₁₉(X=11 Similar to 13) Ferrites Prepared by Citrate Sol-Gel Process. *Rare Metal Materials and Engineering*, **41**, 536-539 (2012).
67. Hoseinkhani, E., Mehdipour, M. & Shokrollahi, H. Comparison of Direct and Indirect Measurements of the Saturation Magnetization of Barium Hexaferrite Synthesized by Coprecipitation. *Journal of Electronic Materials*, **42**, 739-744(2013).
68. Rashad, M. M. & Ibrahim, I. A. Structural, Microstructure and Magnetic Properties of Strontium Hexaferrite Particles Synthesised by Modified Coprecipitation Method. *Materials Technology*, **27**, 308-314(2012).
69. Yu, H.-F. BaFe₁₂O₁₉ Powder with High Magnetization Prepared by Acetone-Aided Coprecipitation. *Journal of Magnetism and Magnetic Materials*, **341**, 79-85 (2013).

70. Yu, M., Hu, J., Liu, J. & Li, S. Electromagnetic Properties of Multiferroic Magnetolectric BaTiO₃-Co_xFe_{3-x}O₄ Core-Shell Particles Obtained by Homogeneous Coprecipitation. *Journal of Magnetism and Magnetic Materials*, **326**, 31-34(2013).
71. Lee, H. M., Bae, S.-Y., Yu, J.-H. & Kim, Y.-J. Preparation of Unsintered Spherical BaFe₁₂O₁₉ Nanoparticles Via an Alcohol-Assisted Spray-pyrolysis Route. *Journal of the American Ceramic Society*, **91**, 2856-2861(2008).
72. Usovich, O. V., Trusov, L. A., Kazin, P. E. & Tret'yakov, Y. D. Preparation of SrFe₁₂O₁₉ Center Dot SrB₂O₄ Magnetic Composites by Spray Pyrolysis. *Inorganic Materials*, **46**, 1137-1142 (2010).
73. Abdel-Hameed, S. A. M. & Margha, F. H. Preparation, Crystallization Behavior and Magnetic Properties of Nanoparticles Magnetic Glass-Ceramics in the Systems Fe₂O₃-CoO-MnO₂, Fe₂O₃-NiO-MoO₃ and Fe₂O₃-CoO-V₂O₅. *Journal of Non-Crystalline Solids*, **358**, 832-838 (2012).
74. Dursun, S., Topkaya, R., Akdogan, N. & Alkoy, S. Comparison of the Structural and Magnetic Properties of Submicron Barium Hexaferrite Powders Prepared by Molten Salt and Solid State Calcination Routes. *Ceramics International*, **38**, 3801-3806 (2012).
75. Gao, X., Du, Y., Liu, X., Xu, P. & Han, X. Synthesis and Characterization of Co-Sn Substituted Barium Ferrite Particles by a Reverse Microemulsion Technique. *Materials Research Bulletin*, **46**, 643-648 (2011).
76. Palla, B. J., Shah, D. O., Garcia-Casillas, P. & Matutes-Aquino, J. Preparation of Nanoparticles of Barium Ferrite from Precipitation in Microemulsions. *Journal of Nanoparticle Research*, **1**, 215-221 (1999).
77. Xu, P., Han, X. J. & Wang, M. J. Synthesis and Magnetic Properties of BaFe₁₂O₁₉ Hexaferrite Nanoparticles by a Reverse Microemulsion Technique. *Journal of Physical Chemistry C*, **111**, 5866-5870 (2007).
78. Topal, U., Ozkan, H. & Dorosinskii, L. Finding Optimal Fe/Ba Ratio to Obtain Single Phase BaFe₁₂O₁₉ Prepared by Ammonium Nitrate Melt Technique. *Journal of Alloys and Compounds*, **428**, 17-21 (2007).
79. He, Z. R., Chen, J. H., Sun, Z. Z., Szulczewski, G. & Li, D. W. Air-flow navigated crystal growth for TIPS pentacene-based organic thin-film transistors. *Organic Electronics* **13**, 1819-1826, (2012).
80. He, Z. R. *et al.* Enhanced Performance Consistency in Nanoparticle/TIPS Pentacene-Based Organic Thin Film Transistors. *Advanced Functional Materials* **21**, 3617-3623, (2011).
81. He, Z. R., Lopez, N., Chi, X. L. & Li, D. W. Solution-based 5, 6, 11, 12-tetrachlorotetracene crystal growth for high-performance organic thin film transistors. *Organic Electronics* **22**, 191, (2015).
82. He, Z. R., Shaik, S., Bi, S., Chen, J. H. & Li, D. W. Air-stable solution-processed n-channel organic thin film transistors with polymer-enhanced morphology. *Applied Physics Letters* **106**, 183301, (2015).

CHAPTER 4 FeCo NANOPARTICLES

4.1. Introduction

High magnetization nanoparticles are showing great potential applications for magnetic energy storage and data storage [1-3], as well as contrast agent for high sensitivity magnetic resonance imaging (MRI) [4-8]. FeCo (with molar ratio of Fe/Co =70/30 [19]) alloy with body centered cubic (BCC) crystal structure has the highest saturation magnetization (~240 emu/g) among all of the discovered magnetic materials except for Fe₁₆N₂ [9]. Several synthesis methods have been proposed so far, however, each method has their own limitations.

Polyol reduction [10] and NaBH₄ reduction [11] are two popular methods to synthesize FeCo nanoparticles because of their low cost and easy operation. However, these surfactant-free synthesis processes always produce agglomerated nanoparticles. Furthermore, impurity phases (Fe_xB [12] and Co_xB [13]) and amorphous products [11] may be formed in NaBH₄ reduction method. Sun and his coworkers [14] successfully synthesized mono-dispersed and high magnetization FeCo nanoparticles by using oleic acid as surfactant. Fe(CO)₅ and Co₂(CO)₈, which are highly toxic [15], are used as iron and cobalt sources. Furthermore, the reaction temperature (250 °C) is much higher than the boiling point (103 °C) of Fe(CO)₅, which brings difficulty to control the composition of FeCo alloy. Liu and his coworkers [16] synthesized mono-dispersed FeCo nanoparticles by annealing CoFe₂O₄ nanoparticles dispersed salt-matrix (NaCl) in a reducing gas (93% Ar + 7% H₂) environment. The salt matrix is used as blocker to prevent CoFe₂O₄ nanoparticles sintering during the high temperature reduction process. The mass ratio of nanoparti-

cles to salt is controlled to 1:1000-1:2000. This brings much difficulty to separate products from the salt after reduction.

To overcome these limitations, we proposed a new method to synthesize FeCo nanoparticles. The FeCo nanoparticles were synthesized from oleic acid assisted reduction, a similar method as synthesis of air-stable Mn nanoparticles [17] by replacing the precursor of MnCl_2 with FeCl_2 and CoCl_2 , and the molar ratio of Fe to Co was controlled at 65/35. Specifically, $\text{FeCl}_2 \cdot 4\text{H}_2\text{O}$ and $\text{CoCl}_2 \cdot 6\text{H}_2\text{O}$ are used as metal precursors, diphenyl ether is solvent, n-Butyllithium (n-BuLi) is reducing agent and oleic acid is surfactant.

4.2. Experimental

Iron(ii) chloride (FeCl_2 , 0.1 g) and cobalt (ii) chloride (CoCl_2 , 0.05 g) were transferred to a 50 mL 3-neck bottle, followed by adding 20 mL diphenyl ether and 1.6 mmol of oleic acid. The 3-neck bottle was refluxed at 260 °C for 2 hours with N_2 protection to dissolve the metal salts, and then decreased to 200 °C. In an argon glove box, 10 mL of diphenyl ether and 5 mL of 2.5M n-BuLi (in hexane) was added to a 50 mL beaker. The hexane was removed by vacuum (glove box transition chamber) for 30 min to prevent overpressure during the injection. The n-BuLi/diphenyl solution was transferred to a syringe, and the needle was sealed with rubber and transferred to outside of the glove box. The n-BuLi/diphenyl solution was then injected to Co^{2+} and Fe^{2+} dispersed diphenyl ether solution by syringe injection with N_2 protection at 200 °C. The final mixture was heated for another 30 min at 200 °C, and finally the reaction was stopped by removing the heating source.

After cooling down, the final solution was transferred to glove box for product washing. The product was washed with hexane for 3 times, and precipitated with ethanol and connected with a rare-earth magnet.

The measurement of X-ray diffraction (XRD) patterns was carried out by a Bruker D8 diffractometer using Cu-K α ($\lambda = 0.154$ nm) radiation, Transmission Electron Microscope (TEM, TECNAI FEI 20) was used to analyze the particle size and morphology. Magnetic properties were checked at room temperature with a Vibrating Sample Magnetometer (VSM, Microsense 3473-70) in an applied field up to 2 T.

4.3. Results and discussion

Figure 4.1a shows the TEM image of as-synthesized FeCo nanoparticles. The TEM sample was prepared by dropping hexane dispersed FeCo nanoparticles onto a copper TEM sample grid with a carbon substrate. It can be seen that the particles are in quasi-spherical shape with mono-dispersion. The surfactant of oleic acid used in the synthesis process can adhere to the surface of the fine ferromagnetic nanoparticles by electrostatic attraction [18], making them well dispersed in hexane. The size distribution in Fig. 4.1b shows that these particles are in a relatively large size distribution, and the average size of is 8.9 nm based on counting 140 nanoparticles. Compared with the narrow size distribution of FeCo nanoparticles from the decomposition of Fe(CO)₅ and Co₂(CO)₈ [14], the broad size distribution in this report could be attributed to the strong reducing agent of n-BuLi that the reaction rate is too fast to control the crystal growth.

The magnetic hysteresis loop of FeCo nanoparticles is shown in Fig. 4.2. The magnetization is 151 emu/g and the coercivity is 41 Oe, showing typical soft magnetic behaviors. The XRD patterns of FeCo nanoparticles are shown in Fig. 4.3. The XRD patterns match well with the BCC structure FeCo nanoparticles. The mean crystallite size of the as-synthesized FeCo particles was calculated from Fig. 4.3 using Scherrer Equation to be 11.2 nm, close to the average size of 8.9 nm counted in TEM image of Fig 4.1a.

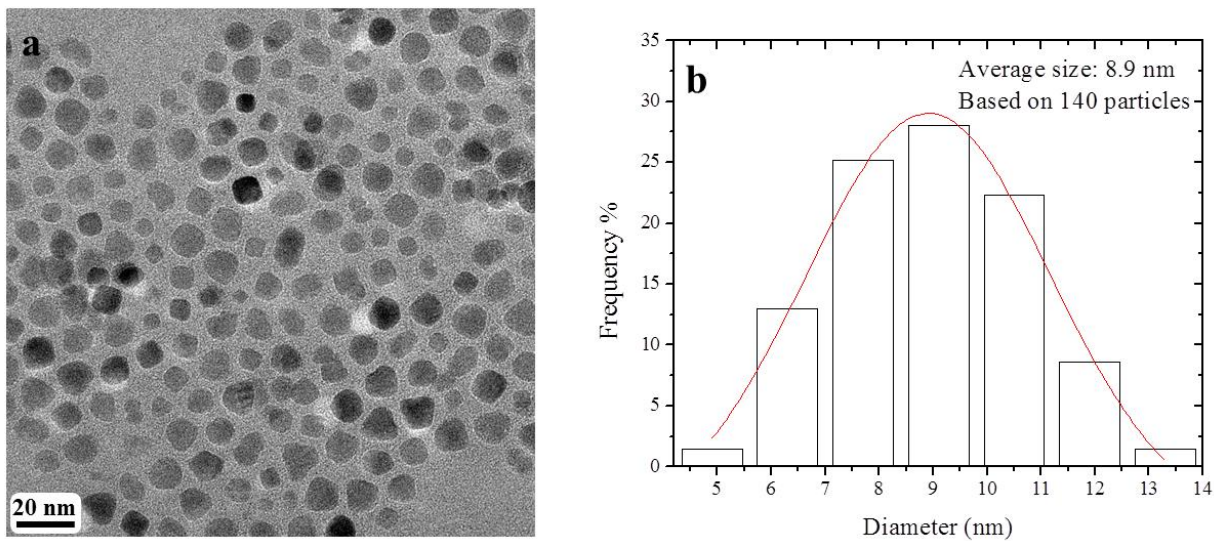


Figure 4.1 (a) TEM image and (b) Particle size distribution, of FeCo nanoparticles.

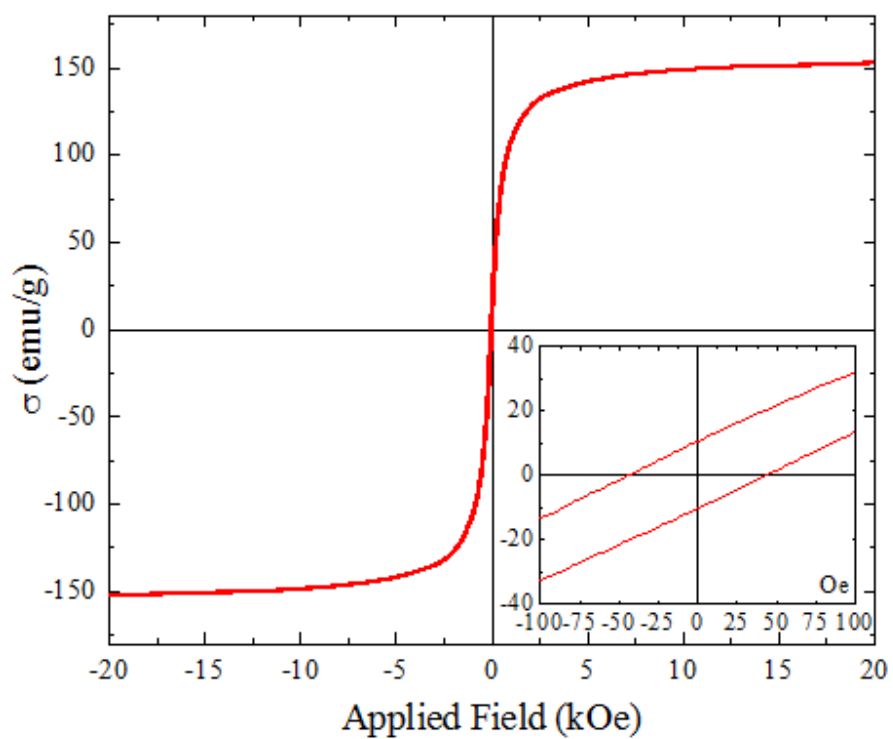


Figure 4.2 Magnetic hysteresis loop of FeCo nanoparticles.

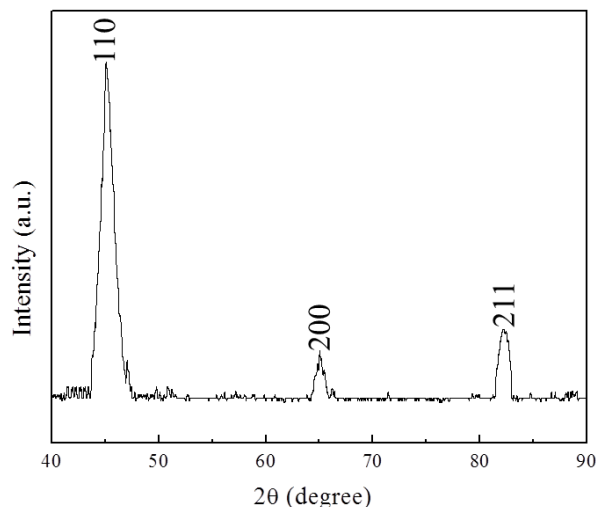


Figure 4.3 Power XRD patterns of FeCo nanoparticles.

4.4. Conclusions

Mono-dispersed FeCo nanoparticles were synthesized by reducing FeCl₂ and CoCl₂ with n-BuLi in diphenyl ether. The mono-dispersion is achieved by using oleic acid as surfactant. The crystal phases were confirmed by XRD, and the average size is 8.9 nm. The magnetization of FeCo nanoparticles is 151 emu/g and the coercivity is 41 Oe.

4.5. References

1. Sun, S. H., Murray, C. B., Weller, D., Folks, L. & Moser, A. Monodisperse FePt Nanoparticles and Ferromagnetic FePt Nanocrystal Superlattices. *Science*, **287**, 1989-1992 (2000).
2. Bader, S. D. Colloquium: Opportunities in Nanomagnetism. *Reviews of Modern Physics*, **78**, 1-15 (2006).
3. Lu, A. H., Salabas, E. L. & Schuth, F. Magnetic Nanoparticles: Synthesis, Protection, Functionalization, and Application. *Angewandte Chemie-International Edition*, **46**, 1222-1244 (2007).
4. Lewin, M. *et al.* Tat Peptide-Derivatized Magnetic Nanoparticles Allow in Vivo Tracking and Recovery of Progenitor Cells. *Nature Biotechnology*, **18**, 410-414 (2000).
5. Zhao, M., Beauregard, D. A., Loizou, L., Davletov, B. & Brindle, K. M. Non-Invasive Detection of Apoptosis Using Magnetic Resonance Imaging and a Targeted Contrast Agent. *Nature Medicine*, **7**, 1241-1244 (2001).
6. Seo, W. S. *et al.* FeCo/Graphitic-Shell Nanocrystals as Advanced Magnetic-Resonance-Imaging and near-Infrared Agents. *Nature Materials*, **5**, 971-976 (2006).

7. Peng, S., Wang, C., Xie, J. & Sun, S. H. Synthesis and Stabilization of Monodisperse Fe Nanoparticles. *Journal of the American Chemical Society*, **128**, 10676-10677 (2006).
8. Sun, C., Lee, J. S. H. & Zhang, M. Q. Magnetic Nanoparticles in Mr Imaging and Drug Delivery. *Advanced Drug Delivery Reviews*, **60**, 1252-1265 (2008).
9. Cullity, B. D. & Graham, C. D. *Introduction to Magnetic Materials*. (Wiley, 2009).
10. Kodama, D. *et al.* Synthesis of Size-controlled Fe-Co Alloy Nanoparticles by Modified Polyol Process. *Journal of Magnetism and Magnetic Materials*, **310**, 2396-2398 (2007).
11. Carroll, K. J. *et al.* Annealing of Amorphous Fe_xCo_{100-x} Nanoparticles Synthesized by a Modified Aqueous Reduction Using NaBH₄. *Journal of Applied Physics*, **107** (2010).
12. Glavee, G. N., Klabunde, K. J., Sorensen, C. M. & Hadjipanayis, G. C. Chemistry of Borohydride Reduction of Iron(ii) and Iron(iii) Ions in Aqueous and Nonaqueous Media - Formation of Nanoscale Fe, FeB, and Fe₂B Powders. *Inorganic Chemistry*, **34**, 28-35 (1995).
13. Glavee, G. N., Klabunde, K. J., Sorensen, C. M. & Hadjipanayis, G. C. Borohydride Reduction of Cobalt Ions in Water - Chemistry Leading to Nanoscale Metal, Boride, or Borate Particles. *Langmuir*, **9**, 162-169 (1993).
14. Wang, C., Peng, S., Lacroix, L. M. & Sun, S. H. Synthesis of High Magnetic Moment CoFe Nanoparticles Via Interfacial Diffusion in Core/Shell Structured Co/Fe Nanoparticles. *Nano Research*, **2**, 380-385 (2009).
15. Chaubey, G. S. *et al.* Synthesis and Stabilization of FeCo Nanoparticles. *Journal of the American Chemical Society*, **129**, 7214-7216 (2007).
16. Poudyal, N., Chaubey, G. S., Rong, C. B., Cui, J. & Liu, J. P. Synthesis of Monodisperse FeCo Nanoparticles by Reductive Salt-Matrix Annealing. *Nanotechnology*, **24**739-745 (2013).
17. Bondi, J., Oyler, K. D. & Schaak, R. E. Chemical Synthesis of Air-Stable Manganese Nanoparticles. *Abstracts of Papers of the American Chemical Society*, **238** (2009).
18. Wang, B. D., Wang, B. G., Wei, P. F., Wang, X. B. & Lou, W. J. Controlled Synthesis and Size-Dependent Thermal Conductivity of Fe₃O₄ Magnetic Nanofluids. *Dalton Transactions*, **41**, 896-899 (2012).
19. Weiss, P. & Forrer, R. La saturation absolue des ferromagnétiques et les lois d'approche en fonction du champ et de la température, *Ann. Phys.*, **12**, 279-374 (1929).

CHAPTER 5 SrFe₁₂O₁₉/FeCo CORE/SHELL PARTICLES

5.1. SrFe₁₂O₁₉/pSiO₂/Co Particles

5.1.1. Introduction

Rare-earth permanent magnets have wide applications in modern life, especially for power generation and consumption, such as power generators and electrical motors (except induction motors). However, the supply of rare-earth elements is facing a lot of crisis. For example, the current main supply country of China is not going to increase the export even though the international consumption is increasing, and the refining processes of rare-earth elements usually bring serious environment pollutions. Therefore, to develop rare-earth-free permanent magnets has been a great interest of materials scientists [1-5]. Different from traditional permanent magnets that only contain one hard phase, one of the solutions of rare-earth-free permanent magnets may contain both hard and soft phases with magnetic exchange coupling between them. The exchange coupled hard/soft magnets make use of high magnetization of soft phase and high coercivity of hard phase, and their energy product can be increased from single phase hard magnet [6,7]. Even though the theory and experiment of exchange coupling have been developed for over 20 years, and some exchange coupled magnets with increased energy products have been successfully synthesized, there are still a lot of challenges remaining.

One of effective methods to synthesize exchange coupled magnets is to combine hard soft materials into core/shell structure. Epitaxial growth is a general way to synthesize core/shell materials. However, lattice mismatch between hard and soft materials has been a great technical barrier to prevent epitaxial growth [8-11]. The failure of epitaxial growth has stimulated discov-

ery of other alternative methods, such as nonepitaxial growth [12] and anion coordination [13]. So far there is still no general method reported for the synthesis of core/shell-structured materials.

We reported a wet chemistry synthesis method beyond epitaxial growth to synthesize spherical hexagonal strontium ferrite (S-SrFe₁₂O₁₉ or S-SrM)/porous silica (pSiO₂)/cobalt (Co) core/shell particles, with magnetically hard S-SrM and soft Co exchange coupling with each other. The S-SrM was first coated with a layer of condensed SiO₂ with Stöber process, and the SiO₂ layer was etched into porous structure with surface-protected etching. The porous SiO₂ surface was further decorated with a monolayer of coupling agent of polyethyleneimine (PEI). Co²⁺ ions were then adsorbed onto SiO₂ surface as the result of the strong chemical affinity between Co²⁺ and amines (-NH₂) from PEI. The ions of Co²⁺ were further reduced into Co nanoparticles by NaBH₄. The S-SrM/pSiO₂/Co core/shell/shell structure is confirmed by TEM image, and the magnetic exchange coupling between SrM and Co particles is demonstrated by smooth magnetic hysteresis loop of SrM/pSiO₂/Co particles.

5.1.2. Experimental

S-SrFe₁₂O₁₉ particles synthesis: spherical SrM particles are synthesized with a spray pyrolysis method, as described in Chapter 3.

S-SrFe₁₂O₁₉/SiO₂ core/shell particles: The S-SrM/SiO₂ core/shell particles are synthesized through a modified Stöber process [14]. Specifically, 0.1 g S-SrM was introduced to a solvent mixture of 80 mL ethanol and 20 mL DI H₂O, and ultrasonicated for 10 min to disperse S-SrM in the solvent. Aqueous ammonia (28% VOL, 5 mL) was introduced to the system with vigorous mechanical stirring, followed by injecting tetraethylorthosilicate (TEOS, 0.5 mL) with a 1 mL syringe. After mechanical stirring for 2 hours, the particles were washed with ethanol and separated with a rare-earth magnet.

S-SrFe₁₂O₁₉/porous SiO₂ core/shell particles: S-SrM/porous SiO₂ (pSiO₂) core/shell particles were obtained by chemically etching the SiO₂ layer of S-SrM/SiO₂ core/shell particles. The etching process was based on a report [15] with little modification. Polyvinylpyrrolidone (PVP, M_w ~ 55000, 1 g) and S-SrM/SiO₂ core/shell particles (0.05 g) were dissolved and dispersed into 20 mL DI H₂O by mechanical stirring. After refluxing at 100 °C for 3 hours, the solution was cooled down to room temperature by removing the heating source. NaOH solution (5 mL, 0.16 g/mL) was added to the system with mechanical stirring to start SiO₂ etching. The reaction was finished after 10 min stirring, and the products were washed with DI H₂O and collected by a rare-earth magnet.

S-SrFe₁₂O₁₉/pSiO₂/Co core/shell/shell particles: S-SrM/pSiO₂ particles (0.05 g) and polyethyleneimine (PEI) (1 g) were introduced to DI H₂O (100 mL) and mechanically stirred for 1 hour, to functionalize the silica surface with amino groups(-NH₂) based on a report [16]. The -NH₂ terminated S-SrM/pSiO₂ colloids were washed with isopropanol and then dispersed in CoCl₂ solution (20 mL, 0.1 g/mL), and mechanically stirred for 30 min to make Co²⁺ adsorbed on -NH₂ functionalized S-SrM/pSiO₂ colloids. Co²⁺ decorated S-SrM/pSiO₂ were washed with DI H₂O one and then re-dispersed in 20 mL DI H₂O with mechanical stirring. NaBH₄ solution (5 mL, 0.1g/mL) was injected into S-SrM/pSiO₂/Co²⁺ dispersion with N₂ protection and mechanical stirring. After 10 min stirring, the products were washed with DI H₂O, and separated with a rare-earth magnet.

5.1.3. Results and discussion

Sol-gel derived silica is well-known for coating materials and forming a core/shell structure [14,17,18]. The surface of S-SrM was coated with a condensed layer of SiO₂ through a Stöber process, and the corresponding surface conditions of S-SrM particle before and after SiO₂

coating are shown in Fig. 5.1a and Fig. 5.1b. The thickness of SiO₂ layer is ~ 20 nm. Co nanoparticles were chemically attached to SiO₂ surface to achieve the exchange coupling between magnetically hard S-SrM and soft Co. To improve the amount of attached Co nanoparticles on SiO₂ surface, the condensed SiO₂ layer is converted into porous structure by a NaOH etching process, with PVP as surface protecting agent [19]. During the refluxing of PVP and SiO₂ in aqueous solution, the strong hydrogen bonds can be readily formed between carbonyl group in PVP and hydroxyls on silica surface [20-23]. The presence of hydrogen bonds in the SiO₂ surface dramatically increases the stability of SiO₂ shell against etching by NaOH solution [19], leading to a porous SiO₂ layer, as shown in Fig. 5.1c. The processes of PVP adsorption and NaOH etching on SiO₂ layer is simplified in Fig. 5.2.

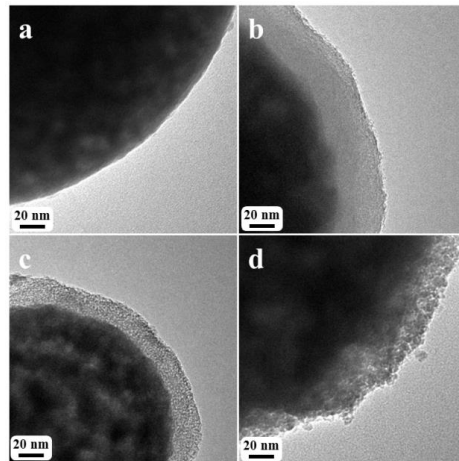


Figure 5.1 TEM of particle surface: (a) S-SrFe₁₂O₁₉ particle; (b) S-SrFe₁₂O₁₉/SiO₂ particle; (c) S-SrFe₁₂O₁₉/pSiO₂ particle; (d) S-SrFe₁₂O₁₉/SiO₂/Co particle.

The porous SiO₂ surface is functionalized with -NH₂ groups by immersing S-SrM/pSiO₂ particles in polyethyleneimine (PEI) aqueous solution. PEI is a typical water-soluble polyamine, and there are large quantities of -NH₂ groups on the macromolecular chains [16]. PEI was chemically grafted onto the surface of SiO₂ via the chemical coupling effect of γ -chloropropyl trimethoxysilane [24-26]. The strong chelation of PEI towards transition-metal ions was combined

with the high specific area of porous SiO₂ [27-29]. Therefore, the novel chelating adsorption material of SiO₂/PEI was prepared. -NH₂ groups possess excellent adsorption properties for Co²⁺ [30]. When S-SrM/pSiO₂/PEI particles are immersed into CoCl₂ aqueous solutions, large amount of Co²⁺ ions are attached to particles surface due to the porous structure of SiO₂. These Co²⁺ ions are further reduced by NaBH₄ into Co nanoparticles with N₂ protection, and the TEM image of S-SrM/pSiO₂/Co core/shell/shell particle is shown in Fig. 5.1d. The processes of PEI and Co²⁺ decoration on SiO₂ surface and Co²⁺ reduction are simplified in Fig. 5.3.

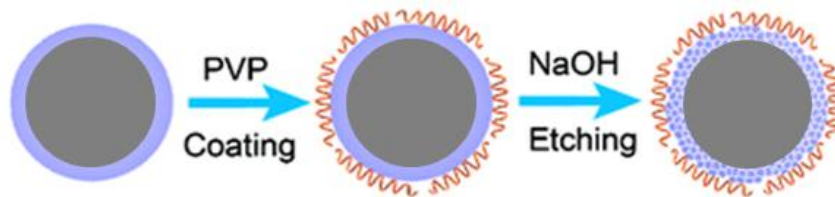


Figure 5.2 A schematic of PVP protected SiO₂ surface etching [19].

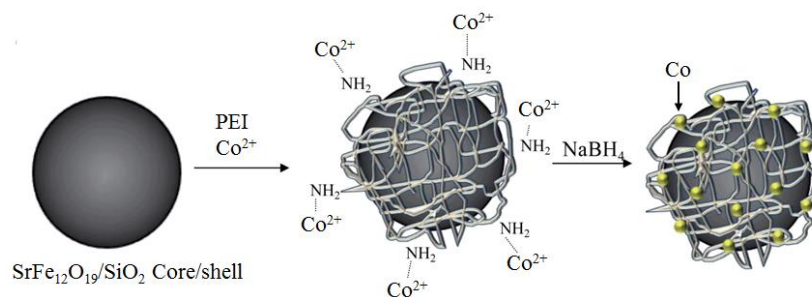


Figure 5.3 A schematic of SiO₂ surface decoration of PEI and Co²⁺ ions and Co²⁺ reduction.

Figure 5.4 shows the VSM loops of S-SrM, S-SrM/pSiO₂ core/shell and S-SrM/pSiO₂/Co core/shell/shell particles. The magnetization of S-SrM/pSiO₂ is reduced to 31.5 emu/g from 38.1 emu/g of S-SrM, while the coercivity keeps almost constant. The decreased magnetization is attributed to the introduction of non-magnetic phase of SiO₂. After Co coating, the magnetization slightly increases to 33.2 emu/g, still lower than pure S-SrM particles of 38.1 emu/g. Even though porous structure of SiO₂, the amount of attached Co nanoparticles is limited, leading to little increase in magnetization. The smooth magnetic hysteresis loop of S-SrM/pSiO₂/Co

core/shell/shell particles indicates an exchange coupling between magnetically hard SrM and soft Co.

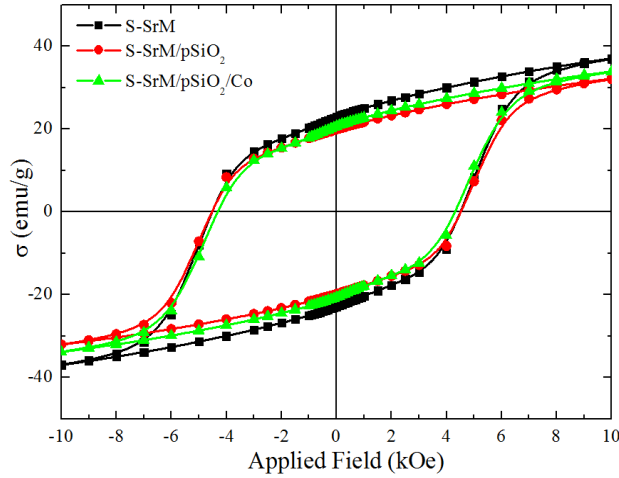


Figure 5.4 The VSM loops of S-SrM, S-SrM/pSiO₂ and S-SrM/pSiO₂/Co particles.

The XRD patterns of S-SrM, S-SrM/pSiO₂ core/shell and S-SrM/pSiO₂/Co core/shell/shell particles are shown in Fig. 5.5. It shows that there is little difference among the XRD patterns of three samples. Neither diffraction peaks of SiO₂ nor Co are shown in corresponding XRD patterns. This could be attributed to amorphous phases of SiO₂ layer and Co nanoparticles formed from their synthesis methods [31,32].

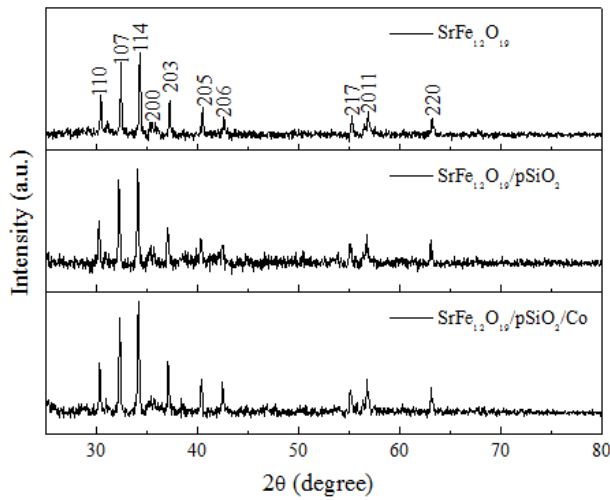


Figure 5.5 The XRD patterns of S-SrM, S-SrM/pSiO₂ core/shell and S-SrM/pSiO₂/Co core/shell/shell particles.

5.1.4. Conclusions

Spherical SrFe₁₂O₁₉/pSiO₂/Co core/shell/shell particles were synthesized through wet chemistry methods. The condensed SiO₂ layer was coated with a Stöber process and etched into porous structure with a PVP protected etching. PEI was chemically attached to porous SiO₂ surface to provide –NH₂ sites for Co²⁺ ions adsorption. Co²⁺ ions were further reduced into Co, forming SrFe₁₂O₁₉/SiO₂/Co core/shell/shell structured particles, which were confirmed by TEM images. The smooth hysteresis loop of SrFe₁₂O₁₉/SiO₂/Co core/shell/shell particles confirmed the exchange coupling between SrFe₁₂O₁₉ and Co.

5.2. SrFe₁₂O₁₉/FeCo Core/shell Particles

5.2.1. Introduction

Core/shell hetero-structured materials with modulated composition have been of great interest because of their novel magnetic [33], catalytic [34], optical [35] and electronic properties [36]. Currently, most core/shell-structured materials are synthesized by epitaxial growth [8,11,37]. Unfortunately, differences in lattice constant, crystal structure and bonding between core and shell materials, limit the application of epitaxial growth [10,37,38]. The failure of epitaxial growth has stimulated discovery of other alternative methods, such as nonepitaxial growth [12] and anion coordination [13]. So far there is still no general method reported for the synthesis of core/shell-structured materials.

The above synthetic methods can be used to synthesize magnetically hard/soft core/shell materials. This structure combines the large coercivity of the magnetically hard core and the large magnetic moment of the magnetically soft shell by exchange coupling [6,7,39], giving excellent magnetic properties. These have potentials to replace rare-earth (RE) permanent magnets such as Nd₂Fe₁₂B and SmCo₅ with common, inexpensive materials. RE elements have limited

accessibility, relatively high cost, and unacceptable environmental hazard in the extraction processes [40]. Herein, we present a new coating concept of magnetic self-assembly and report a novel route to achieve magnetically hard/soft core/shell structured particles. The concept and approach are demonstrated through the synthesis of SrFe₁₂O₁₉/FeCo core/shell submicron particles.

5.2.2. Experimental

Hexagonal strontium ferrite (SrFe₁₂O₁₉ or SrM) particles were synthesized by a traditional ceramic method [41] by firing a mixture of Fe₃O₄ [42] and SrCO₃ [43] nanoparticles. SrFe₁₂O₁₉ particles (0.1 g) were dispersed into 60 mL EG (ethylene glycol) under ultrasonication for 30 min. Sodium acetate (NaOAc, 1 g), sodium hydroxide (NaOH, 4 g), iron (II) chloride tetrahydrate (FeCl₂·4H₂O, 0.4 g) and cobalt chloride hexahydrate (CoCl₂·6H₂O, 0.1 g) were introduced into another 60 mL EG. The two aliquots of EG were mixed and vigorously stirred in a three-neck flask with a magnetic stir bar. The reaction mixture was at first heated to 100 °C for 30 min to completely dissolve all of the chemicals, then increased to 180 °C with average heating rate of 2 °C/min, and finally kept for 30 min to reduce Fe and Co salts into FeCo alloy. After the reaction, the heating source was removed and solution was cooled down to room temperature. The products were separated with a rare-earth magnet and washed with ethanol for 3 times. To protect the products from oxidation, the processes of chemicals introduction and mixing, chemical reaction, solvent cooling and products washing were conducted under a N₂ atmosphere.

5.2.3. Results and discussion

5.2.3.1. SrFe₁₂O₁₉/FeCo core/shell and SrFe₁₂O₁₉/FeCo/SiO₂ core/shell/shell particles

Two steps are involved in the synthesis of SrM/FeCo core/shell particles: i) FeCo alloy nanoclusters are synthesized by wet chemical reduction of their chloride salts; ii) as-synthesized FeCo nanoclusters self-assemble on the SrM surface by magnetic attraction. However, SrM can

be reduced and decomposed by the reducing agent. The challenge here is to reduce iron and cobalt salts into an FeCo alloy, and at the same time, protect SrM from reduction. EG was chosen as the solvent and reducing agent [44-46]. Typically, FeCo particle synthesis by EG reduction is conducted at its boiling point (~ 200 °C) [44-46]. However, our experiments showed that EG can also reduce SrM at the boiling temperature. The reduction potential of EG can be regulated by controlling the reaction temperature [47]. Therefore, after all the chemicals (NaOH, NaOAc, FeCl₂ and CoCl₂) were introduced into a dispersion of SrM particles in EG, the reaction temperature was kept at 180 °C for 30 minutes. It was confirmed that an FeCo nanoparticle alloy was formed and less than 10% of SrM was lost under this reaction condition.

It was reported that FeCo particles over 30 nm were formed without NaOAc [48]. As soon as the FeCo nucleus is formed in the solvent, NaOAc is assumed to adhere to the surface of FeCo nucleus, thereby inhibiting nucleus growth. This results in formation of FeCo nanoclusters of 2-3 nm, which is a precondition for the formation of magnetically self-assembled SrM/FeCo core/shell particles. Our experimental results also showed that when the FeCo particle size was over 50 nm, the magnetic attraction was not strong enough for them to self-assemble on the SrM surface to form a shell.

Figure 5.6a shows a TEM image of an as-prepared SrM particle. For effective exchange coupling to occur between hard and soft phases, the dimension of the soft phase should be smaller than twice the domain wall thickness of the hard phase [6,7,39], less than 28 nm in the case of SrM [49]. A TEM image of a SrM/FeCo core/shell particle is shown in Fig. 5.6b. The surface of the SrM is decorated with FeCo nanoclusters with thickness of ~ 15 nm. A representative TEM image of several SrM/FeCo core/shell particles in lower magnification is also shown Fig. 5.7. The surface is not uniformly covered as confirmed by tilt-angle TEM images, as shown in Fig.

5.8 and may be a result of the uneven magnetic field distribution. Energy dispersive X-ray (EDX) spectrometry of SrM/FeCo core/shell particles was checked by TEM and the results were shown in Fig. 5.9. The line scan across a particle shows that the Sr signal was almost zero and the Fe and Co signals were relatively high at both ends of the selected particle. This result indicates the existence of FeCo nanoclusters on the surface of SrM.

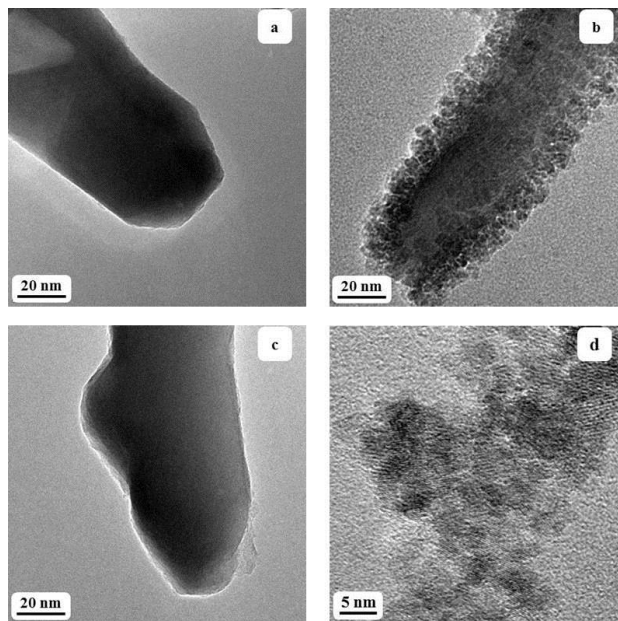


Figure 5.6 TEM images of SrM and SrM/FeCo core/shell and FeCo particle: (a) as-prepared SrM particle; (b) SrM/FeCo core/shell particle; (c) SrM particle (after demagnetization of core/shell particles); (d) FeCo nanoclusters (after demagnetization of core/shell particles).

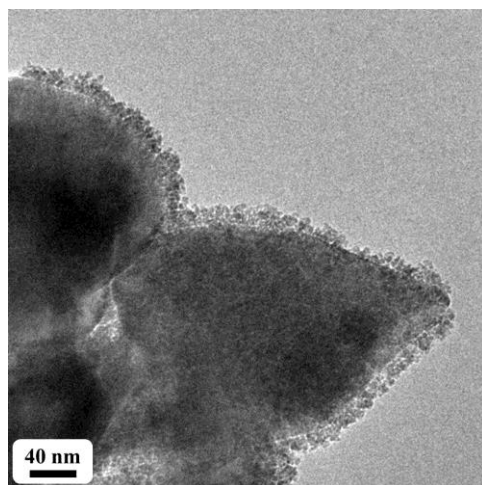


Figure 5.7 TEM image of SrM/FeCo core/shell nanoparticle.

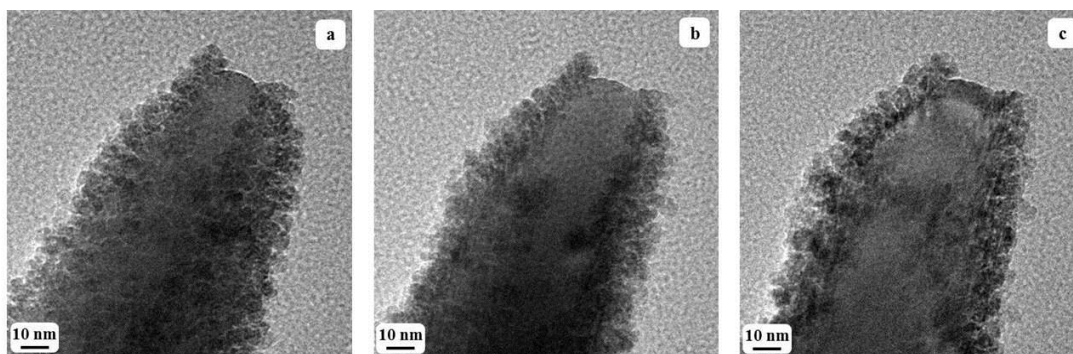


Figure 5.8 Tilt-angle TEM images. (a) $\theta = 0^\circ$. (b) $\theta = 30^\circ$. (c) $\theta = 60^\circ$.

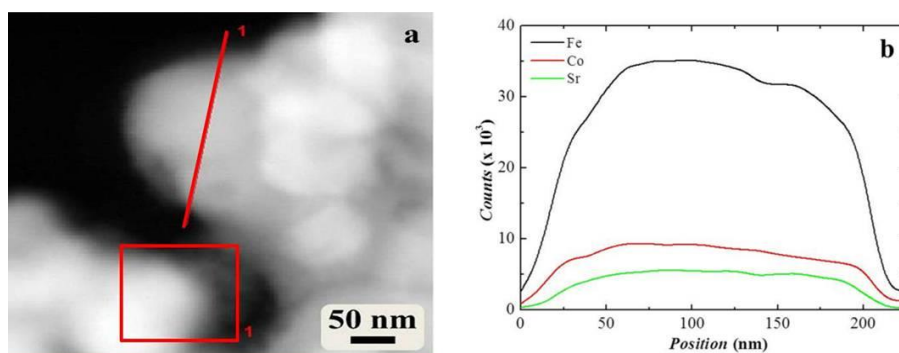


Figure 5.9 The line scan of energy dispersive X-ray (EDX) spectrometry for SrM/FeCo core/shell particles: (a) Scanning transmission electron microscopy (STEM) image (the line shows the scanning area, and the square is located to prevent electron beam shifting); (b) Elemental analysis for the EDX line scan.

Alternating current (AC) demagnetization was applied to the core/shell particles using a vibrating sample magnetometer (VSM), and TEM images were taken after that. After demagnetization, the SrM surface became bare as shown in Fig. 5.6c. Isolated FeCo nanoclusters, formerly attached to the SrM core particles, are shown in Fig. 5.6d. The demagnetization test confirms that the magnetic attraction between the magnetically hard SrM and soft FeCo is the origin for the formation of core/shell structured nanoparticles, rather than epitaxial growth or some other process. To better explain the formation process of magnetically self-assembled core/shell structured particles, a schematic diagram is shown in Fig. 5.10. As soon as randomly distributed FeCo nanoclusters are formed in the solvent, they are magnetically attracted to nearby SrM particles. This interaction leads to the formation of core/shell structured particles. It is unnecessary for the

magnetically attracted soft phase to be a single layer of nanoclusters. The thickness of the attracted soft phase is assumed to be determined by the remanent magnetization of the hard phase. A higher remanent magnetization of the hard phase will result in a thicker layer of the soft phase nanoclusters.

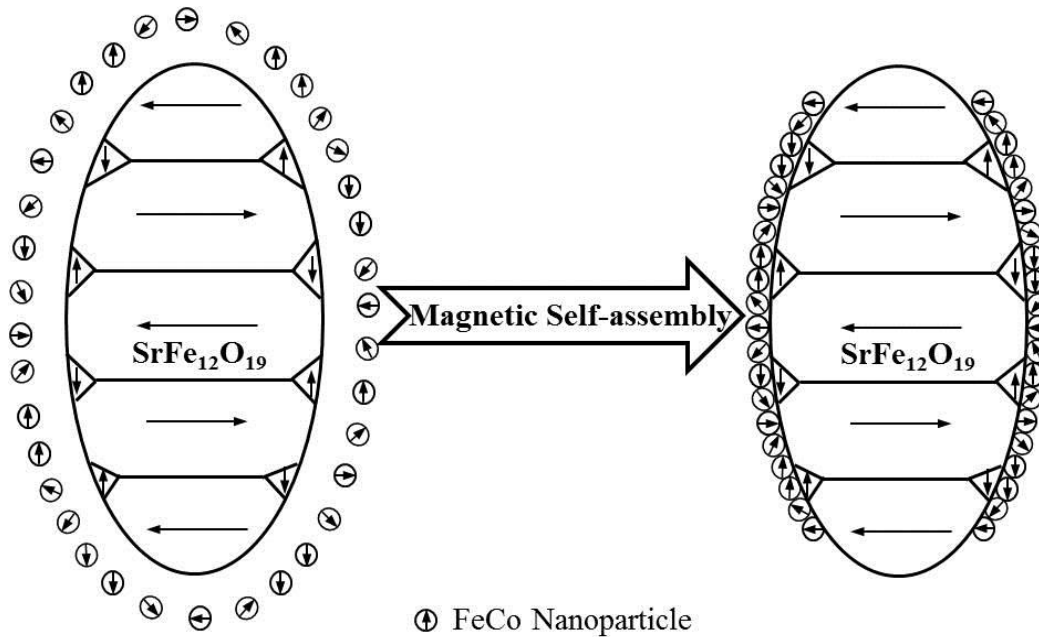


Figure 5.10 The schematic of the formation process of $\text{SrFe}_{12}\text{O}_{19}/\text{FeCo}$ core/shell nanoparticles by magnetic self-assembly.

Powder X-ray diffraction (XRD) patterns were used to determine the phase of both core and core/shell particles. Figure 5.11a shows the XRD pattern of pure SrM core particles. The XRD pattern of SrM/FeCo core/shell particles is presented in Fig. 3.6b and the peaks for SrM in Fig. 5.11b match well with those in Fig. 5.11a. This indicates that the SrM phase is well maintained during the reduction reaction. At the same time, an FeCo peak was also detected in Fig. 5.11b, which confirms the existence of the soft phase in the core/shell particles. The broader peak from FeCo compared to those from SrM is attributed to the small FeCo particle size [50].

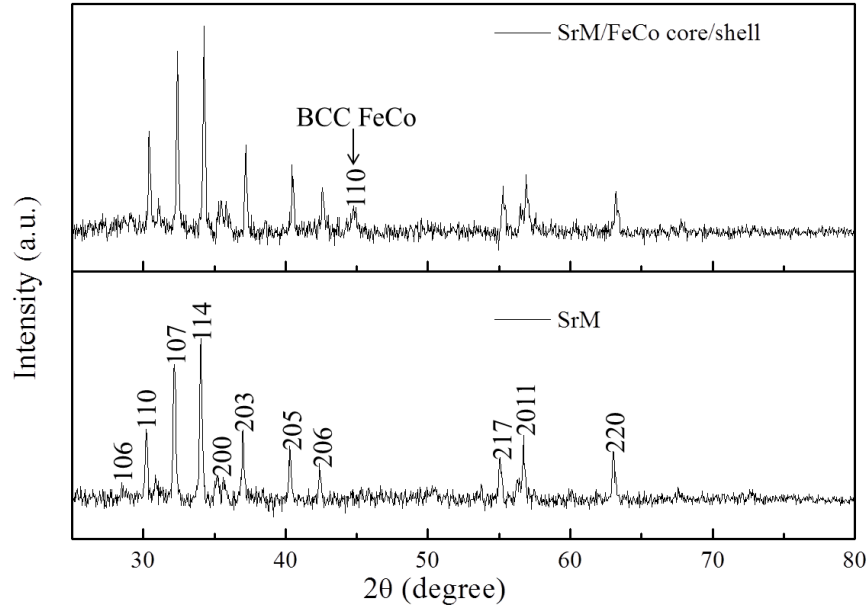


Figure 5.11 Powder X-ray diffraction patterns of SrM core and SrM/FeCo core/shell particles: (a) XRD pattern of SrM particles; (b) XRD pattern of SrM/FeCo core/shell particles.

Figure 5.12a shows magnetic hysteresis loops for SrM core and SrM/FeCo core/shell particles. The saturation magnetization of SrM/FeCo core/shell particles increased from 65.3 emu/g to 80.5 emu/g, while the coercivity decreased from 5.75 kOe to 3.81 kOe compared to the SrM core particles. The magnetic hysteresis loop of the core/shell particles shows a negligible kink, and generally follows the Stoner-Wohlfarth model [51] for uniaxial, isotropic, non-interacting particles, which suggests exchange coupling exists between the magnetically hard phase of SrM and soft phase of FeCo. The B-H curves of SrM core and SrM/FeCo core/shell particles are shown in Fig. 5.12b, and the corresponding $(BH)_{max}$ is 0.86 and 1.04 MGOe. The increased $(BH)_{max}$ in SrM/FeCo core/shell particles could be attributed to exchange coupling SrM and FeCo particles.

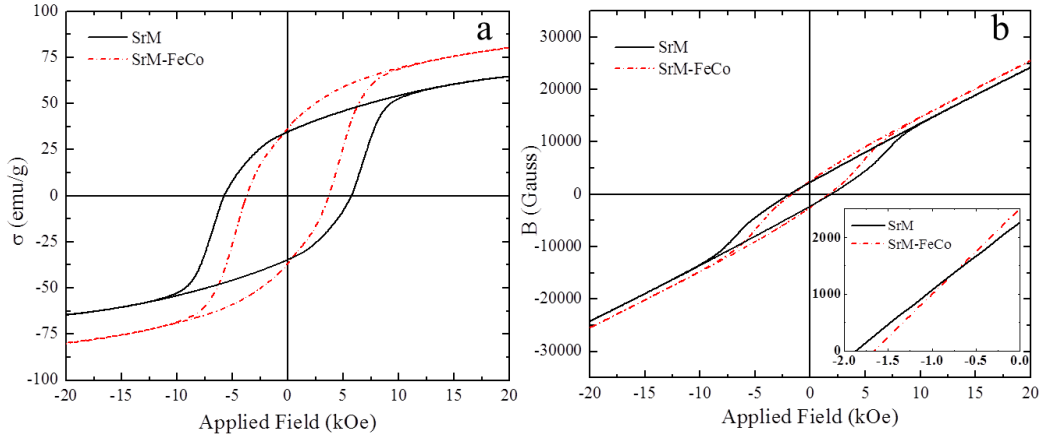


Figure 5.12 (a) M-H curves and (b) B-H curves of SrM core and SrM/FeCo core/shell particles.

Nanoparticles of FeCo are unstable in air due to oxidation [52]. To improve their stability, the surface of SrM/FeCo core/shell particles is coated with a thin layer of SiO₂ with stöber process. The TEM of images of SrM/FeCo core/shell and SrM/FeCo/SiO₂ core/shell/shell particles are shown in Fig. 5.13, and the thickness of the SiO₂ shell is around 10 nm. Due to the introduction of non-magnetic phase of SiO₂, the magnetization of SrM/FeCo/SiO₂ core/shell/shell particles is decreased to 64.1 emu/g from 70.3 emu/g in SrM/FeCo core/shell particles, while still higher than 55.5 emu/g in SrM particles, as shown in Fig. 5.14a. Due to the amorphous state of coated SiO₂ [31], there is no obvious difference between XRD patterns of SrM/FeCo core/shell and SrM/FeCo/SiO₂ core/shell/shell particles, as shown in Fig. 5.14b.

To investigate the stability of SrM/FeCo core/shell and SrM/FeCo/SiO₂ core/shell/shell particles, both of them are exposed in air for 2 hours after synthesis. The magnetic hysteresis loops of particles of as-synthesized states and exposed in air for 2 hours are shown in Fig. 5.15. For uncoated particles, the magnetization is decreased to 66 emu/g from 71 emu/g after exposing in air for 2 hours, as shown in Fig. 5.15a. However, there is negligible change on magnetization for the SiO₂ coated particles, as shown in Fig. 5.15b. The magnetization decrease in uncoated parti-

cles could be attributed to the oxidation of FeCo nanoparticles exposed in air, while SiO₂ coated particles are protected from oxidation and show higher stability.

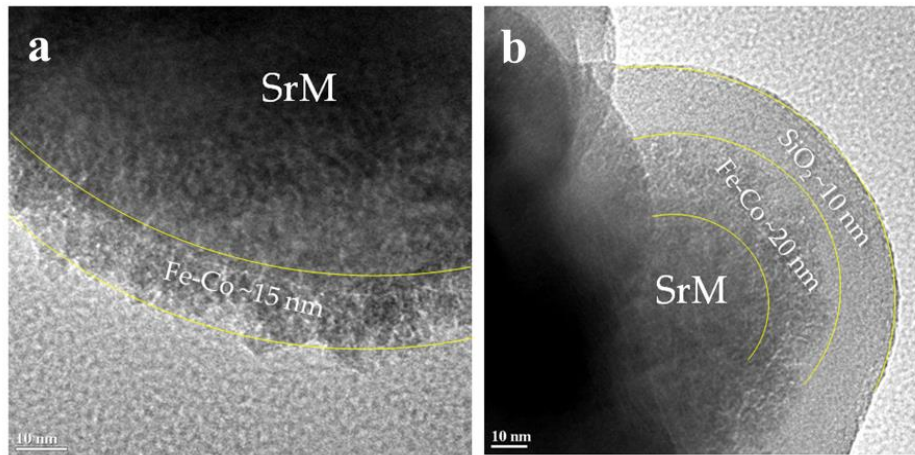


Figure 5.13 TEM images of (a) SrM/FeCo core/shell particles; (b) SrM/FeCo/SiO₂ core/shell/shell nanoparticles.

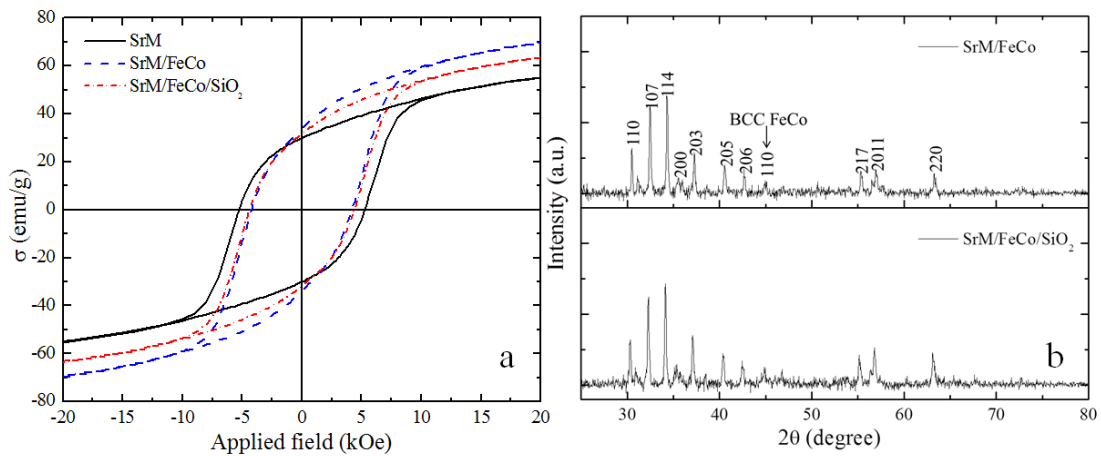


Figure 5.14 (a) The VSM loops of SrM, SrM/FeCo core/shell and SrM/FeCo/SiO₂ core/shell/shell particles; (b) The XRD patterns of SrM/FeCo and SrM/FeCo/SiO₂ particles.

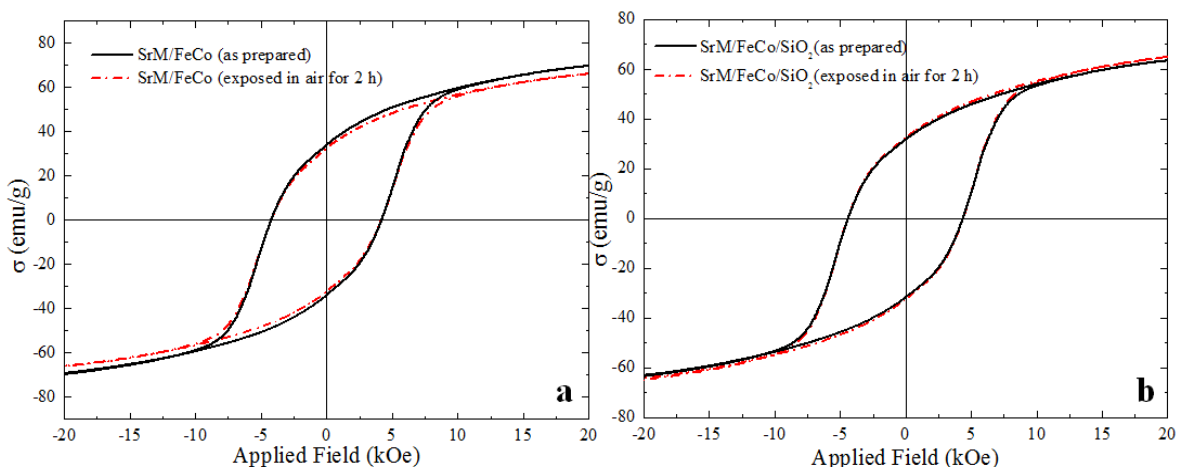


Figure 5.15 (a) the VSM loops of SrM/FeCo core/shell particles in as-prepared state and exposed in air for 2 hours; (b) the VSM loops of SrM/FeCo/SiO₂ core/shell/shell particles in as-prepared state and exposed in air for 2 hours.

5.2.3.2. SrFe₁₂O₁₉/FeCo core/shell particles with various shell thickness

Within the range of magnetic attraction, the shell thickness of SrM/FeCo core/shell particles can be regulated by controlling the concentrations of Fe and Co precursors. Four different concentrations of Fe and Co precursors are investigated in this section. The specific parameters are listed in Tab. 5.1, and the molar ratio of Fe to Co is controlled to 2. With concentration increasing, samples are noted as SrM/FeCo-1, SrM/FeCo-2, SrM/FeCo-3 and SrM/FeCo-4, respectively, and the pure SrM is noted as SrM-0. All the experimental operations and other parameters keep the same as described above in Experimental Part.

Table 5.1 Four concentrations of Fe and Co precursors in synthesis of SrM/FeCo core/shell particles.

Materials	SrM (g)	FeCl ₂ ·4H ₂ O (mmol)	CoCl ₂ ·6H ₂ O (mmol)
SrM-0	0.1	0	0
SrM/FeCo-1	0.1	0.5	0.25
SrM/FeCo-2	0.1	1	0.5
SrM/FeCo-3	0.1	1.5	0.75
SrM/FeCo-4	0.1	2	1

Figure 5.16 shows the TEM images of different shell thickness of SrM/FeCo core/shell particles originated from different concentrations of Fe and Co precursors. FeCo nanoparticles are not uniformly attracted on SrM surface, and this was explained by uneven distributed magnetic field of SrM particles in the part of 5.2.1 this chapter. With precursor concentration increasing, the shell thickness increases in the samples of SrM/FeCo-1, SrM/FeCo-2 and SrM/FeCo-3, from ~5 nm, to ~10 nm and ~15 nm. This is because more FeCo particles are formed at with higher concentration. However, when the precursor concentration further increases in sample SrM/FeCo-4, the shell thickness keeps at ~ 15 nm, and extra FeCo nanoparticles are shown around core/shell nanoparticle. Due to the limited magnetization of SrM, there is a critical thickness of FeCo layer in magnetically self-assembled SrM/FeCo core/shell particles. When the distance between SrM and FeCo particles is larger than the critical thickness, the magnetic attraction between them will be very weak, and FeCo nanoparticles can not be further attracted by SrM. Therefore, after the saturation of SrM surface attraction, FeCo nanoparticles agglomerate on SrM/FeCo core/shell nanoparticle surface, instead of forming a thicker FeCo shell.

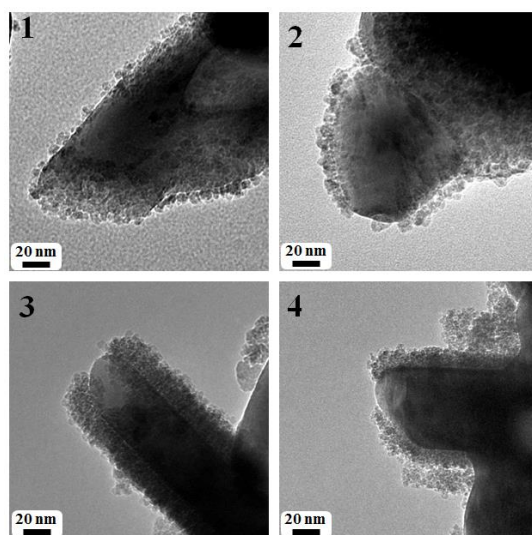


Figure 5.16 The TEM images of SrM/FeCo core/shell particles with different concentration of FeCo precursors: (1) $\text{FeCl}_2 \cdot 4\text{H}_2\text{O}$: 0.5 mmol, $\text{CoCl}_2 \cdot 6\text{H}_2\text{O}$: 0.25 mmol; (2) $\text{FeCl}_2 \cdot 4\text{H}_2\text{O}$: 1 mmol, $\text{CoCl}_2 \cdot 6\text{H}_2\text{O}$: 0.5 mmol; (3) $\text{FeCl}_2 \cdot 4\text{H}_2\text{O}$: 1.5 mmol, $\text{CoCl}_2 \cdot 6\text{H}_2\text{O}$: 0.75 mmol; (4) $\text{FeCl}_2 \cdot 4\text{H}_2\text{O}$: 2 mmol, $\text{CoCl}_2 \cdot 6\text{H}_2\text{O}$: 1 mmol.

Figure 5.17 shows the VSM loops of SrM and four samples of SrM/FeCo particles with different concentrations of Fe and Co precursors. Single-phase SrM has the highest coercivity but lowest magnetization. With soft phase amount increasing, the magnetization increases and coercivity decreases step by step in SrM/FeCo particles, this matches well with exchange coupling theory proposed by Skomski et al [7]. The hysteresis loops of SrM/FeCo-1, SrM/FeCo-2 and SrM/FeCo-3 samples are smooth and kink-free, show single-phase-like magnetic behaviors, and indicate effective exchange coupling between magnetically hard SrM and soft FeCo particles. The exchange coupling can be further explained by their TEM images that all FeCo nanoparticles are attracted on SrM surface, and their thickness is less than 20 nm, which is a critical thickness of soft phase exchange coupled with SrM. However, there is an obvious kink in the sample of SrM/FeCo-4, showing two-phase magnetic behaviors and indicating the existence of unexchange coupled soft phase. This could be confirmed by its TEM image in Fig. 5.16d that besides ~ 15 nm shell of FeCo nanoparticles, extra FeCo nanoparticles agglomerate on SrM/FeCo core/shell nanoparticle surface. This makes the overall FeCo layer thickness larger than 20 nm, beyond the critical thickness soft phase that could be exchange coupled with SrM.

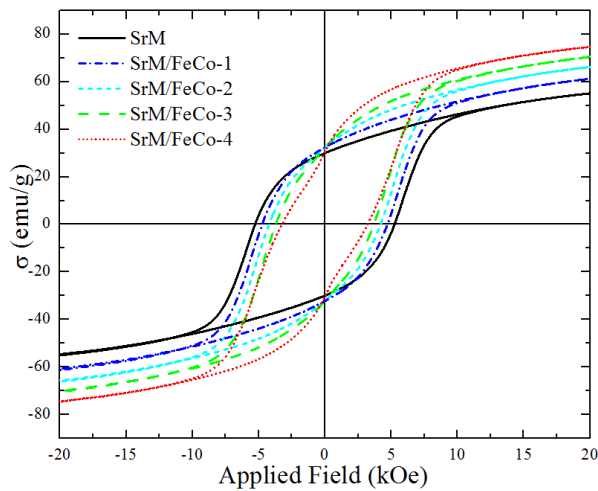


Figure 5.17 The VSM loops of SrM particles and SrM/FeCo core/shell particles with different concentrations of Fe and Co precursors.

Figure 5.18 shows the XRD patterns of SrM and SrM/FeCo core/shell particles with different concentrations. FeCo diffraction peak can not be found in the sample of SrM/FeCo-1, this could be attributed to the low concentration of FeCo precursors, and the amount of FeCo formed is beyond the detection limit of X-ray diffractometer. With concentrations of Fe and Co precursors increasing in samples of SrM/FeCo-2, SrM/FeCo-3 and SrM/FeCo-4, more FeCo nanoparticles form, leading to stronger peak intensity.

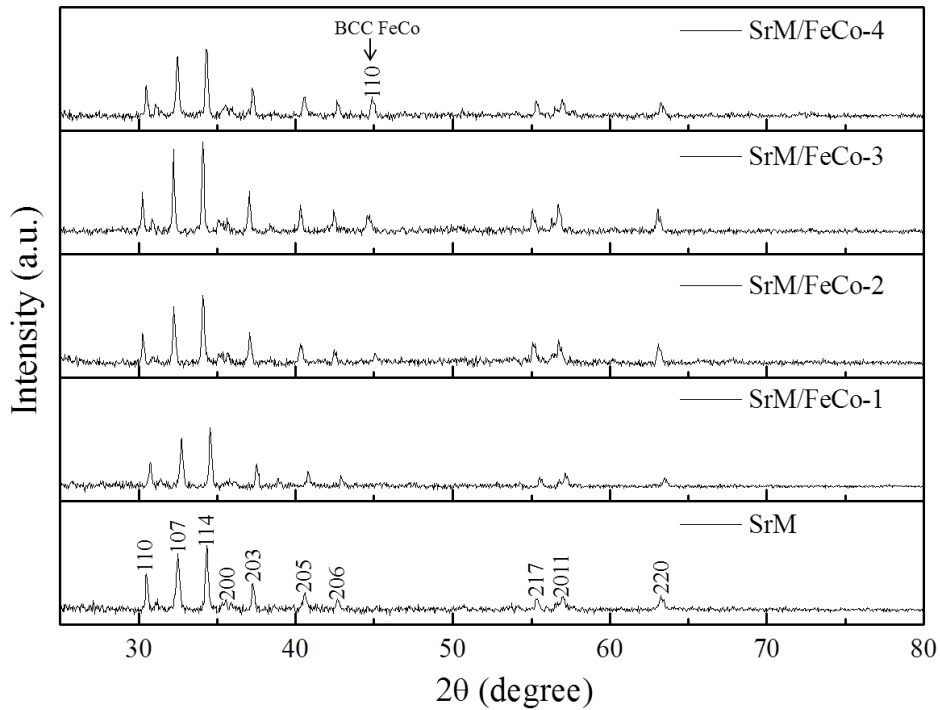


Figure 5.18 The XRD patterns of SrM/FeCo core/shell particles with different concentration of FeCo precursors.

5.2.3.3. SrFe₁₂O₁₉/FeCo core/shell particles and SrFe₁₂O₁₉/FeCo particle mixture

To further investigated the magnetic exchange coupling between SrM and FeCo particles, SrM/FeCo nanoparticle mixture is synthesized and its magnetic properties are compared with SrM/FeCo core/shell particles. The SrM/FeCo nanoparticle mixture is obtained by pestle grinding SrM and FeCo particles in a mortar. FeCo nanoparticles synthesis process is the same as that in SrM/FeCo core/shell particles, but without adding SrM. The mass ratio of soft phase is con-

trolled to be the same in both samples. The as-synthesized FeCo nanoparticles are characterized and the results are shown in Fig. 5.19. FeCo nanoparticles show typical soft magnetic behavior in Fig. 5.19a, with magnetization of 169 emu/g and coercivity of 83 Oe. The crystal structure is confirmed by XRD patterns in the inset of Fig. 5.19a, and only 110 peak is shown, as the intensity of other two peaks of 200 and 220 are too weak to be distinguished from noise. TEM image in Fig. 5.19b shows that FeCo nanoparticles agglomerate together and form secondary structure of clusters.

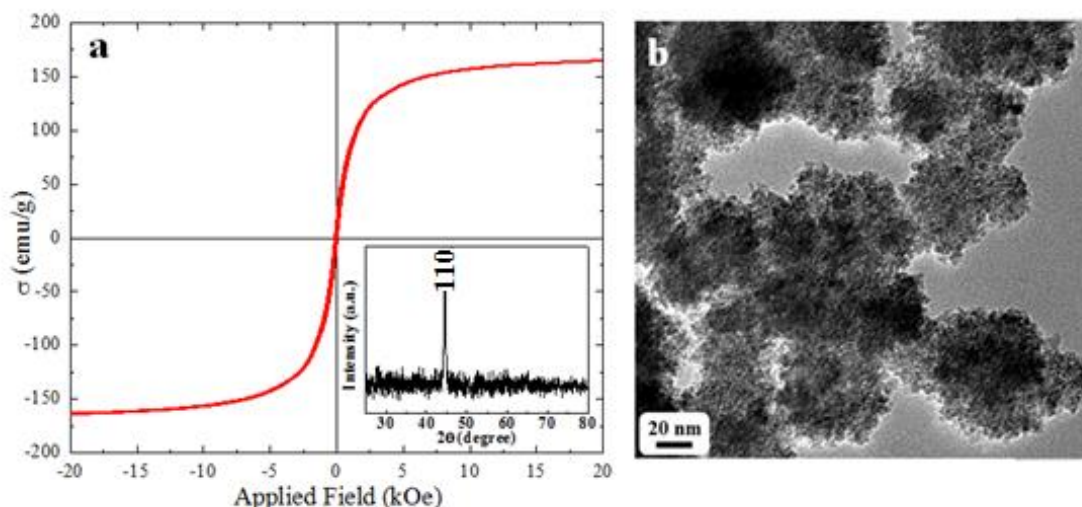


Figure 5.19 FeCo nanoparticles: (a) VSM loop, inset: XRD patterns; (b) TEM image.

The magnetic hysteresis loops of SrM particles, SrM/FeCo core/shell particles and SrM/FeCo nanoparticle mixture are shown in Fig. 5.20a. The magnetic hysteresis loop of SrM/FeCo core/shell particles is smooth, shows single-phase-like magnetic behaviors, and indicates an effective exchange coupling between magnetically hard SrM and soft FeCo phases. However, there is a kink in the magnetic hysteresis loop of SrM/FeCo nanoparticle mixture. This two-phase magnetic behavior reveals a weak or no exchange coupling between hard and soft phases.

The smoothness of VSM loops can be further analyzed by their derivative curves, as shown in Fig. 5.20b. As a comparison, the derivative curve of single hard phase SrM magnetic hysteresis loop is also presented. There is a negligible kink in derivative curve of SrM/FeCo core/shell particles hysteresis loop, which is similar to single hard phase of SrM particles. However, there is an obvious peak in the hysteresis loop derivative curve of SrM/FeCo nanoparticle mixture at around 0 kOe. This could be attributed to the uneven distribution between FeCo and SrM particles, and there are unexchange coupled FeCo nanoparticles remaining in the mixture.

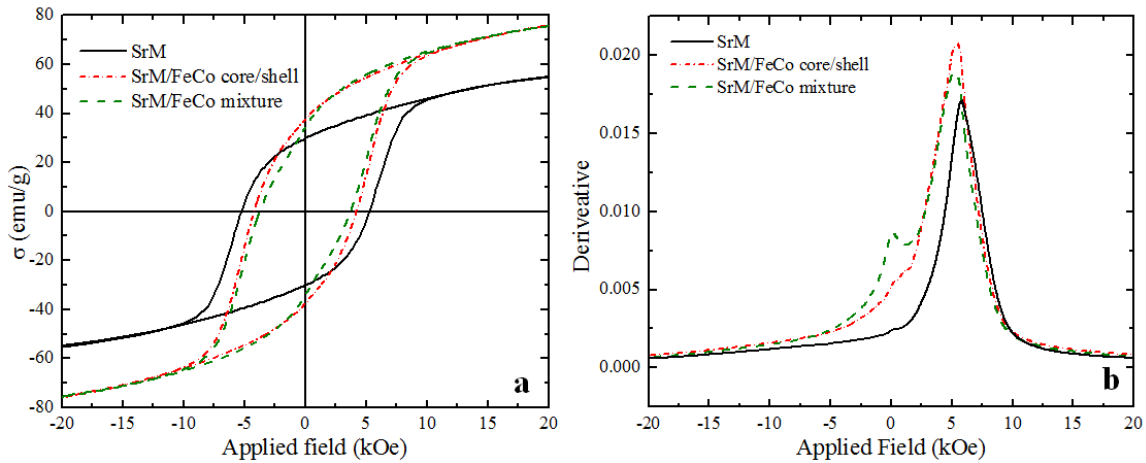


Figure 5.20 (a) the VSM loops of SrM particles, SrM/FeCo core/shell particles and SrM/FeCo particles mixture; (b) derivative curve of SrM/FeCo core/shell particles and SrM/FeCo particles mixture.

The TEM image of SrM/FeCo nanoparticle mixture is shown in Fig. 5.21. It shows that FeCo nanoparticles are self-agglomerated, the surface of SrM particles is clear, and FeCo and SrM particles are separated from each other. During the FeCo synthesis, as soon as nanoparticles are formed, they tend to agglomerate with each other, instead of attracted by SrM and forming core/shell structure in SrM/FeCo core/shell particles synthesis process. The grinding process on SrM and FeCo particles can not redisperse FeCo nanoparticles. The large size of FeCo nanoparticle clusters leads to a low efficiency of exchange coupling between SrM and FeCo particles.

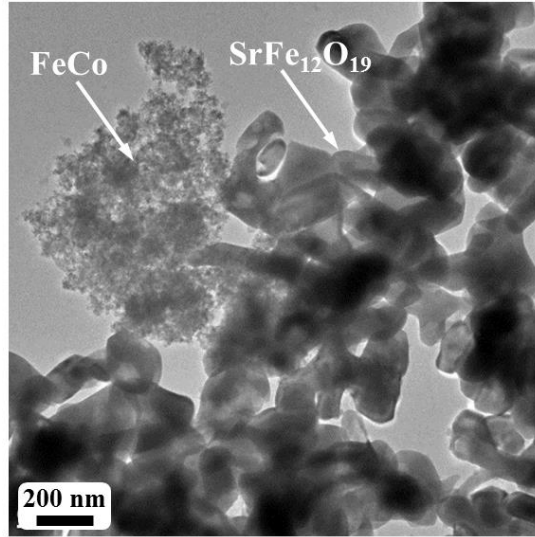


Figure 5.21 TEM image of SrFe₁₂O₁₉/FeCo nanoparticle mixture.

5.2.4. Conclusions

We have reported a new method to synthesize core/shell structured particles by magnetic self-assembly. By combining two materials in this way, the lattice mismatch that prevents epitaxial growth can be overcome, the size of hard phase and soft phase can be separately controlled and the mass diffusion between two phases does not happen. These core/shell-structured particles have better magnetic properties because of exchange coupling [6,7,39], making them excellent candidates for RE-free permanent magnets made from abundant and inexpensive elements. Moreover, this method might also be employed to fabricate completely new architectures for other applications [53-55]. The SiO₂ coating on SrM/FeCo core/shell particles is proven to be effective to protect the particles from oxidation. Within the range of magnetic attraction, the shell thickness of SrM/FeCo particles can be controlled by regulating the concentration of Fe and Co precursors. Compared with SrM/FeCo core/shell particles, SrM/FeCo nanoparticle mixture is proven to be less effective on magnetic exchange coupling between SrM and FeCo particles.

5. 3. References

1. Cui, J. *et al.* Thermal Stability of Mnbi Magnetic Materials. *Journal of Physics-Condensed Matter*, **26** (2014).
2. Poudyal, N. & Liu, J. P. Advances in Nanostructured Permanent Magnets Research. *Journal of Physics D-Applied Physics*, **46** (2013).
3. Liu, Y., George, T. A., Skomski, R. & Sellmyer, D. J. Aligned and Exchange-Coupled Fept-Based Films. *Applied Physics Letters*, **99** (2011).
4. Rong, C. B. *et al.* Bulk Fept-Based Nanocomposite Magnets with Enhanced Exchange Coupling. *Journal of Applied Physics*, **102** (2007).
5. Zeng, H., Sun, S. H., Li, J., Wang, Z. L. & Liu, J. P. Tailoring Magnetic Properties of Core/Shell Nanoparticles. *Applied Physics Letters*, **85**, 792-794 (2004).
6. Kneller, E. F. & Hawig, R. The Exchange-Spring Magnet - A New Material Principle for Permanent-Magnets. *IEEE Transactions on Magnetics*, **27**, 3588-3600 (1991).
7. Skomski, R. & Coey, J. M. D. Giant Energy Product in Nanostructured 2-Phase Magnets. *Physical Review B*, **48**, 15812-15816 (1993).
8. Habas, S. E., Lee, H., Radmilovic, V., Somorjai, G. A. & Yang, P. Shaping Binary Metal Nanocrystals through Epitaxial Seeded Growth. *Nature Materials*, **6**, 692-697 (2007).
9. Chambers, S. A. Epitaxial Growth and Properties of Thin Film Oxides. *Surface Science Reports*, **39**, 105-180 (2000).
10. Palmstrom, C. J. Epitaxy of Dissimilar Materials. *Annual Review of Materials Science*, **25**, 389-415 (1995).
11. Jin, M. S. *et al.* Copper Can Still Be Epitaxially Deposited on Palladium Nanocrystals to Generate Core-Shell Nanocubes Despite Their Large Lattice Mismatch. *ACS Nano*, **6**, 2566-2573 (2012).
12. Zhang, J. T., Tang, Y., Lee, K. & Min, O. Y. Nonepitaxial Growth of Hybrid Core-Shell Nanostructures with Large Lattice Mismatches. *Science*, **327**, 1634-1638 (2010).
13. Serpell, C. J., Cookson, J., Ozkaya, D. & Beer, P. D. Core@Shell Bimetallic Nanoparticle Synthesis Via Anion Coordination. *Nature Chemistry*, **3**, 478-483 (2011).
14. Graf, C., Vossen, D. L. J., Imhof, A. & van Blaaderen, A. A General Method to Coat Colloidal Particles with Silica. *Langmuir*, **19**, 6693-6700 (2003).
15. Ge, J. P., Zhang, Q., Zhang, T. R. & Yin, Y. D. Core-Satellite Nanocomposite Catalysts Protected by a Porous Silica Shell: Controllable Reactivity, High Stability, and Magnetic Recyclability. *Angewandte Chemie-International Edition*, **47**, 8924-8928 (2008).
16. An, F. Q., Gao, B. J. & Feng, X. Q. Adsorption and Recognition Properties of Ionic Imprinted Polyamine IIP-PEI/SiO₂ Towards Pb²⁺ Ion. *Journal of Applied Polymer Science*, **112**, 2241-2246 (2009).

17. Ohmori, M. & Matijevic, E. Preparation and Properties of Uniform Coated Colloidal Particles Silica on Hematite. *Journal of Colloid and Interface Science*, **150**, 594-598 (1992).
18. Philipse, A. P., Nechifor, A. M. & Patmamanoharan, C. Isotropic and Birefringent Dispersions of Surface-Modified Silica Rods with a Boehmite-Needle Core. *Langmuir*, **10**, 4451-4458 (1994).
19. Zhang, Q., Zhang, T. R., Ge, J. P. & Yin, Y. D. Permeable Silica Shell through Surface-Protected Etching. *Nano Letters*, **8**, 02867-2871 (2008).
20. Belyakova, L. A., Varvarin, A. M., Lyashenko, D. Y. & Roik, N. V. Adsorption of Poly(1-Vinyl-2-Pyrrolidone) on the Surface of Highly Disperse Amorphous Silica. *Russian Journal of Physical Chemistry*, **77**, 270-274 (2003).
21. Otsuka, H., Esumi, K., Ring, T. A., Li, J. T. & Caldwell, K. D. Simultaneous Adsorption of Poly(N-Vinyl-2-Pyrrolidone) and Hydrocarbon/Fluorocarbon Surfactant from Their Binary Mixtures on Hydrophilic/Hydrophobic Silica. *Colloids and Surfaces a-Physicochemical and Engineering Aspects*, **116**, 161-171 (1996).
22. Gun'ko, V. M. *et al.* Successive Interaction of Pairs of Soluble Organics with Nanosilica in Aqueous Media. *Journal of Colloid and Interface Science*, **300**, 20-32 (2006).
23. Nelson, A., Jack, K. S., Cosgrove, T. & Kozak, D. Nmr Solvent Relaxation in Studies of Multicomponent Polymer Adsorption. *Langmuir*, **18**, 2750-2755 (2002).
24. An, F. Q. & Gao, B. J. Chelating Adsorption Properties of PEI/SiO₂ for Plumbum Ion. *Journal of Hazardous Materials*, **145**, 495-500 (2007).
25. An, F. Q., Gao, B. J. & Li, G. Studies on Preparation of Ion-Imprinted Polyethyleneimine on Silica Gel Particles and Binding Properties for Metal Ions. *Acta Polymerica Sinica*, 366-373 (2007).
26. Gao, B. J., An, F. Q. & Zhu, Y. Novel Surface Ionic Imprinting Materials Prepared Via Couple Grafting of Polymer and Ionic Imprinting on Surfaces of Silica Gel Particles. *Polymer*, **48**, 2288-2297 (2007).
27. Haron, M. J. *et al.* Benzyl and Methyl Fatty Hydroxamic Acids Based on Palm Kernel Oil as Chelating Agent for Liquid-Liquid Iron(iii) Extraction. *International Journal of Molecular Sciences*, **13**, 2148-2159 (2012).
28. Bisset, W., Jacobs, H., Koshti, N., Stark, P. & Gopalan, A. Synthesis and Metal Ion Complexation Properties of a Novel Polyethyleneimine N-Methylhydroxamic Acid Water Soluble Polymer. *Reactive & Functional Polymers*, **55**, 109-119 (2003).
29. Chanda, M. & Rempel, G. L. Polyethyleneimine Gel-Coat on Silica - High Uranium Capacity and Fast Kinetics of Gel-Coated Resin. *Reactive Polymers*, **25**, 25-36 (1995).
30. Kara, M., Yuzer, H., Sabah, E. & Celik, M. S. Adsorption of Cobalt from Aqueous Solutions onto Sepiolite. *Water Research*, **37**, 224-232 (2003).
31. Zhang, Y. W. *et al.* Synthesis and Characterization of a Novel Au Nanocatalyst with Increased Thermal Stability. *Dalton Transactions*, **43**, 1360-1367 (2014).

32. Carroll, K. J. *et al.* Annealing of Amorphous Fe_xCo_{100-x} Nanoparticles Synthesized by a Modified Aqueous Reduction Using NaBH₄. *Journal of Applied Physics*, **107** (2010).
33. Lee, J. H. *et al.* Exchange-Coupled Magnetic Nanoparticles for Efficient Heat Induction. *Nature Nanotechnology*, **6**, 418-422 (2011).
34. Migowski, P. & Dupont, J. Catalytic Applications of Metal Nanoparticles in Imidazolium Ionic Liquids. *Chemistry-a European Journal*, **13**, 32-39 (2007).
35. Zhang, K. *et al.* Enhanced Optical Responses of Au@Pd Core/Shell Nanobars. *Langmuir*, **25**, 1162-1168 (2009).
36. Daniel, M. C. & Astruc, D. Gold Nanoparticles: Assembly, Supramolecular Chemistry, Quantum-Size-Related Properties, and Applications toward Biology, Catalysis, and Nanotechnology. *Chemical Reviews*, **104**, 293-346 (2004).
37. Fan, F. R. *et al.* Epitaxial Growth of Heterogeneous Metal Nanocrystals: From Gold Nano-Octahedra to Palladium and Silver Nanocubes. *Journal of the American Chemical Society*, **130**, 6949-6955 (2008).
38. Wang, Z. L. Transmission Electron Microscopy of Shape-Controlled Nanocrystals and Their Assemblies. *Journal of Physical Chemistry B*, **104**, 1153-1175 (2000).
39. Schrefl, T., Kronmuller, H. & Fidler, J. Exchange Hardening in Nano-Structured 2-Phase Permanent-Magnets. *Journal of Magnetism and Magnetic Materials*, **127**, L273-L277 (1993).
40. Okabe, T. H. Current Status and Problems on Rare Earth Metals. *Journal of Japanese Society of Tribologists*, **56**, 460-465 (2011).
41. Liu, Y., Drew, M. G. B. & Liu, Y. Optimizing the Methods of Synthesis for Barium Hexagonal Ferrite-an Experimental and Theoretical Study. *Materials Chemistry and Physics*, **134**, 266-272 (2012).
42. Sugimoto, T. & Matijevic, E. Formation of Uniform Spherical Magnetite Particles by Crystallization from Ferrous Hydroxide Gels. *Journal of Colloid and Interface Science*, **74**, 227-243(1980).
43. Kompany, A. Preparation and Characterization of Barium Carbonate Nanoparticles. *International Journal of Chemical Engineering and Applications-IJCEA* (2011).
44. Zhu, Y. F., Zhao, W. R., Chen, H. R. & Shi, J. L. A Simple One-Pot Self-Assembly Route to Nanoporous and Monodispersed Fe₃O₄ Particles with Oriented Attachment Structure and Magnetic Property. *Journal of Physical Chemistry C*, **111**, 5281-5285 (2007).
45. Deng, H. *et al.* Monodisperse Magnetic Single-Crystal Ferrite Microspheres. *Angewandte Chemie-International Edition*, **44**, 2782-2785 (2005).
46. Huba, Z. J., Carroll, K. J. & Carpenter, E. E. Synthesis of High Magnetization Feco Alloys Prepared by a Modified Polyol Process. *Journal of Applied Physics*, **109** (2011).
47. Bonet, F. *et al.* Electrochemical Reduction of Noble Metal Species in Ethylene Glycol at Platinum and Glassy Carbon Rotating Disk Electrodes. *Solid State Ionics*, **126**, 337-348 (1999).

48. Kodama, D. *et al.* Synthesis of Size-Controlled Fe-Co Alloy Nanoparticles by Modified Polyol Process. *Journal of Magnetism and Magnetic Materials*, **310**, 2396-2398 (2007).
49. Ziese, M. & Thornton, M. J. *Spin Electronics*. (Springer, 2001).
50. Patterson, A. L. The Scherrer Formula for X-Ray Particle Size Determination. *Physical Review*, **56**, 978-982 (1939).
51. Cullity, B. D. & Graham, C. D. *Introduction to Magnetic Materials*. (Wiley, 2009).
52. Chaubey, G. S. *et al.* Synthesis and Stabilization of FeCo Nanoparticles. *Journal of the American Chemical Society*, **129**, 7214-7218 (2007).
53. He, Z. R., Chen, J. H., Keum, J. K., Szulczewski, G. & Li, D. W. Improving performance of TIPS pentacene-based organic thin film transistors with small-molecule additives. *Organic Electronics* **15**, 150-155, (2014).
54. Chen, J. H. *et al.* Conjugated Polymer-Mediated Polymorphism of a High Performance, Small-Molecule Organic Semiconductor with Tuned Intermolecular Interactions, Enhanced Long-Range Order, and Charge Transport. *Chemistry of Materials* **25**, 4378-4386, (2013).
55. He, Z. R., Li, D. W., Hensley, D. K., Rondinone, A. J. & Chen, J. H. Switching phase separation mode by varying the hydrophobicity of polymer additives in solution-processed semiconducting small-molecule/polymer blends. *Applied Physics Letters* **103**, 113301, (2013).

CHAPTER 6 MnBi/FeCo COMPOSITES

6.1. MnBi/FeCo Composites

6.1.1. Introduction

Rare-earth (RE) free permanent magnets have been of great research interest due to RE elements' restricted accessibility, relatively high cost, and their environmental hazard in extraction processes. Low temperature phase (LTP) MnBi has a high magnetocrystalline anisotropy (1.6×10^6 J/m³ at 300 K) [1], large coercivity (1.7 T at 300 K) [2] and a positive temperature coefficient of coercivity (between 150 and 550 K) [3], making it a potential material for a RE free permanent magnet [4]. All of the MnBi used in this dissertation research is in LTP phase. Cui and his coworkers prepared MnBi powders by arc melting with a maximum energy product ($(BH)_{\max}$) of 11.9 MGOe, and bulk MnBi of 7.8 MGOe at room temperature [5]. Exchange coupled hard/soft magnetic materials can further improve the $(BH)_{\max}$, by taking advantage of high magnetization of the soft phase and large coercivity of the hard phase [6-8].

High energy ball milling is a popular method to mix magnetically hard and soft phases for exchange coupling. The size of the soft phase can be effectively decreased to below twice the domain wall thickness of the hard phase (< 20 nm for MnBi) and exchange coupling between the hard and soft phases is demonstrated [9,10]. The hard phase is preferred to be of single domain size (~500 nm) for maximum coercivity [11]. However, the size of hard phase can be over reduced in the strong milling process, leading to a low coercivity, and therefore a low $(BH)_{\max}$ of exchange coupled products. In this part, we report a synthesis of an exchange coupled MnBi

(hard)/FeCo (soft) composites, in which the size of the MnBi and FeCo phases can be controlled separately, preventing a size over reduction of MnBi.

6.1.2. Experimental

The MnBi particles used for MnBi/FeCo composite synthesis were received from Pacific Northwest National Laboratory (PNNL). MnBi was prepared by arc melting followed by grinding, annealing and ball milling to get raw particles (~50 microns) [5]. To further decrease the particle size and increase the coercivity, MnBi raw particles were mechanically ground in hexane. The FeCo nanoparticles were synthesized from oleic acid assisted reduction following reference [12] by replacing MnCl₂ with FeCl₂ and CoCl₂ and the molar ratio of Fe to Co was controlled at 65/35, and synthesis details were discussed in Chapter 4. As-synthesized FeCo nanoparticles were dispersed in hexane. MnBi raw particles were added to the dispersion and ground with pestle and mortar inside an Ar atmosphere glove box. The mass of MnBi+FeCo was controlled at 0.1 g, hexane volume was 20 mL, and grinding time was 5 min. The hexane evaporated during the grinding, leaving the MnBi/FeCo composites. There are two functions for the grinding: 1) decreasing the size of MnBi raw particles to increase their coercivity; 2) homogeneously mixing FeCo and MnBi particles. The mass percentage of FeCo was controlled at 5% and 10%, respectively. For comparison, pure MnBi raw particles were also ground under the same condition.

6.1.3. Results and discussion

The XRD pattern of as-received MnBi in Fig. 6.1 confirms the LTP MnBi phase mixed with little Bi phase. The SEM image of as-received MnBi in Fig. 6.2a shows that the particle size ranges from around 10 to 50 μm . Because the particles are in random shape, and Sherrer Equation for calculating crystalline size does not work when the particle size is over 100 nm [13], it is

hard to statistically determine the particle size and size distribution from SEM image and XRD patterns.

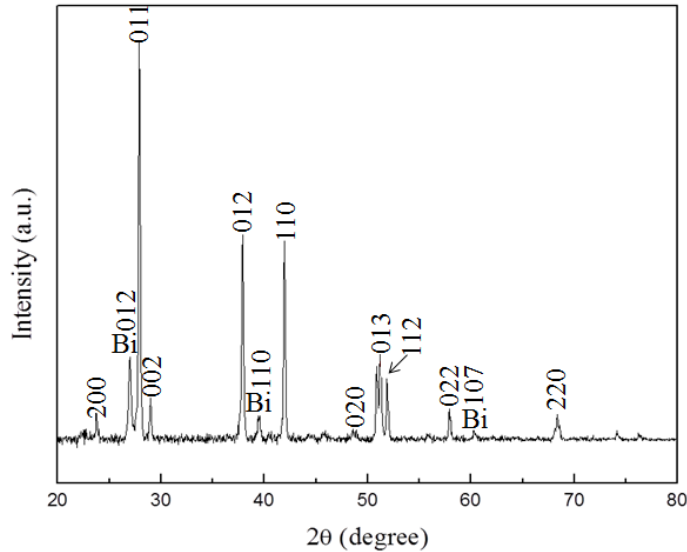


Figure 6.1 XRD patterns of as-received MnBi particles.

Highest coercivity of magnetic particles is obtained when their size is of single domain [11]. Magnetic coercivity decreases as particle size increases if the particles are larger than single domain (multi-domain). The single domain size of LTP MnBi is around 500 nm [14]. Therefore, the size of as-received MnBi needs to be decreased to increase its coercivity. Mortar and pestle grinding of MnBi in hexane is applied inside an Ar environment glove box to decrease the particle size. The as-received MnBi particles were gently ground for 5 min, 7 min and 10 min, respectively. These ground particles were characterized with VSM, TEM and SEM for magnetic properties and morphology. The SEM images in Fig. 6.2 show that, the particle size dramatically decreased to less than 10 μm after 5 min grinding, as shown in Fig. 6.2b. However, further extending the grinding time did not lead to an obvious size reduction, as shown in Figs. 6.2c and d. The magnetic hysteresis loops of ground MnBi particles are shown in Fig. 6.3. It can be seen that,

with increased grinding time, there is little difference in the magnetization, while coercivity continuously and dramatically increases.

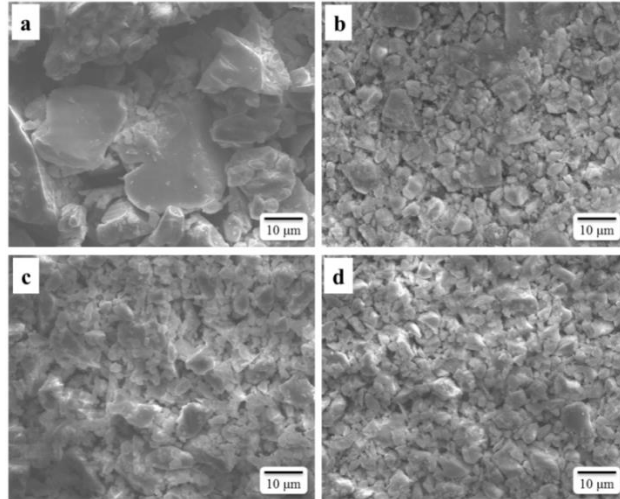


Figure 6.2 SEM images of (a) as received MnBi; (b) 5 min; (c) 7 min; (d) and 10 min grinding of the MnBi particles.

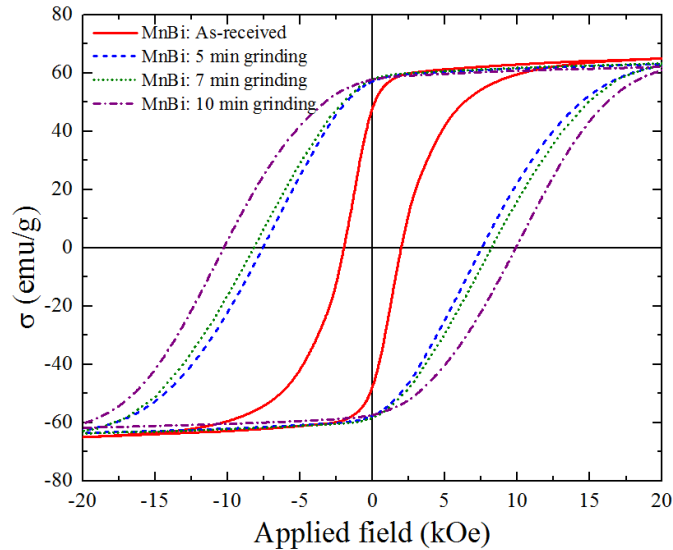


Figure 6.3 Magnetic hysteresis loops of as-received MnBi, 5 min ground MnBi, 7 min ground MnBi and 10 min ground MnBi particles. These particles were aligned in a 16 kOe magnetic field before VSM characterization.

The corresponding characterization results of as-synthesized FeCo nanoparticles are shown in Fig. 6.4. The magnetization is 151 emu/g and coercivity is 41 Oe, with typical soft magnetic behavior. The transmission electron microscopy (TEM) sample was prepared by dropping hex-

ane dispersed FeCo nanoparticles onto a copper TEM sample grid with a carbon substrate. The surfactant oleic acid used in the synthesis adheres to the surface of the fine ferromagnetic nanoparticles by electrostatic attraction [15], making them well dispersed in hexane. The FeCo nanoparticles are around 10 nm and mono-dispersed, as shown in Fig. 6.4 top inset. The crystal phases were confirmed by powder X-ray diffraction (XRD, Cu-K α radiation) patterns shown in Fig. 6.4 bottom inset.

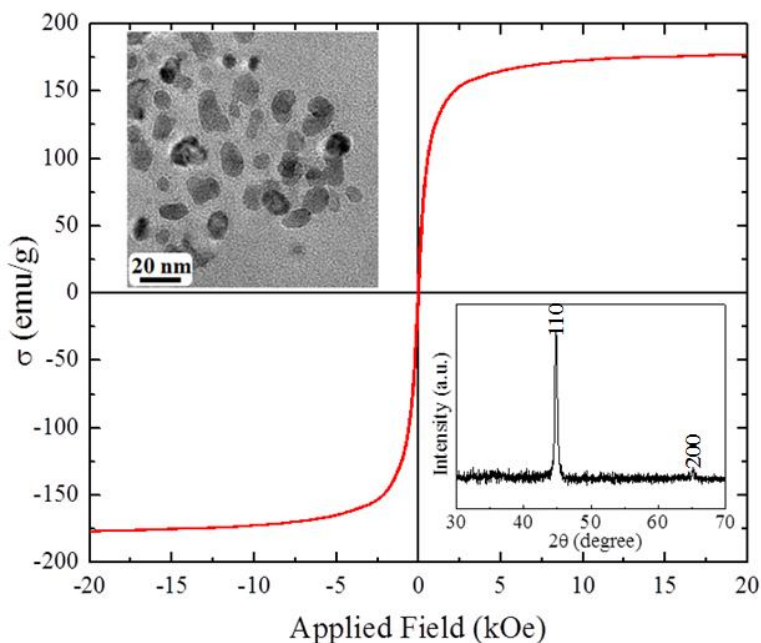


Figure 6.4 Hysteresis loop of the FeCo nanoparticles. The top inset shows TEM image, and bottom inset shows XRD patterns.

Figure 6.5 shows the magnetic hysteresis loops of MnBi particles and MnBi/FeCo (95/5 wt% and 90/10 wt%) composites. These particles were aligned in a magnetic field of 16 kOe before characterization by vibrating sample magnetometry (VSM). Pure MnBi particles show highest coercivity (8189 Oe), but lowest magnetization (59 emu/g). With increasing FeCo percentage, the magnetization increases and coercivity decreases in both MnBi/FeCo composites, and their smooth magnetic hysteresis loops indicate single-phase-like magnetic behaviors. Compared with pure MnBi particles, the MnBi/FeCo (95/5 wt%) composites show an increased remanent mag-

netization, indicating effective exchange coupling, while MnBi/FeCo (90/10 wt%) composites show a decreased remanent magnetization, indicating weak exchange coupling [7]. The corresponding B-H curves of pure MnBi particles, the MnBi/FeCo (95/5 wt%) and MnBi/FeCo (90/10 wt%) composites are showing in Fig. 6.5b. Their $(BH)_{max}$ was calculated to be 5.21, 4.47 and 2.47 MGOe, respectively.

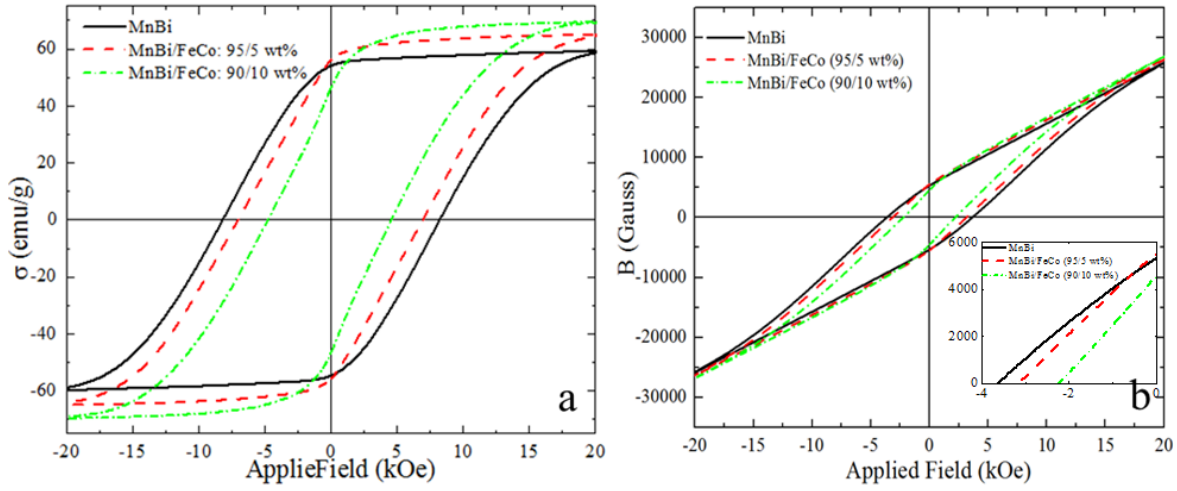


Figure 6.5 (a) M-H curves and (b) B-H curves of MnBi particles and MnBi/FeCo (95/5 wt% and 90/10 wt%) composites.

One of the methods to understand the magnetic coupling between grains is so-called Delta M (ΔM) method. The ΔM is defined as $\Delta M = M_d(H) - [1-2M_r(H)]$, where M_d is the normalized demagnetization remanence, M_r is the normalized isothermal magnetization remanence, and H is the applied magnetic field[16,17]. In this study, the ΔM curves for the three samples were measured in the field up to 20 kOe. The result is shown in Fig. 6.5. It is of interest to note that the ΔM curve for the MnBi is negative over the entire field range, whereas, that for the MnBi/FeCo (90/10 wt%) is positive except for the high field region beyond 10 kOe. This result indicates that the magneto-static coupling among the grains is dominant for MnBi particles, whereas the exchange coupling for MnBi (90/5 wt%). The magnetic coupling between grains for MnBi/FeCo (90/10 wt%) is, on the other hand, rather complicated, since it depends largely on applied field.

The present results of ΔM measurements suggest that FeCo shell plays a key role for the magnetic exchange coupling between the composite particles.

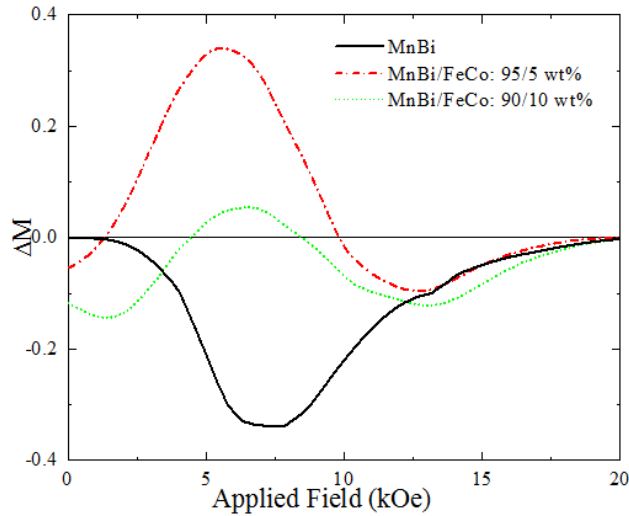


Figure 6.6 ΔM curves of MnBi particles and MnBi/FeCo (95/5 wt% and 90/10 wt%) composites.

XRD patterns of MnBi particles and MnBi/FeCo (95/5 wt% and 90/10 wt%) composites are shown in Fig. 6.7. It can be seen that the MnBi particles are mainly LTP MnBi phase mixed with a small amount of Bi phase. The FeCo peak presents in both samples of MnBi/FeCo (95/5 wt% and 90/10 wt%) composites, and higher mass percentage leads to a higher peak intensity.

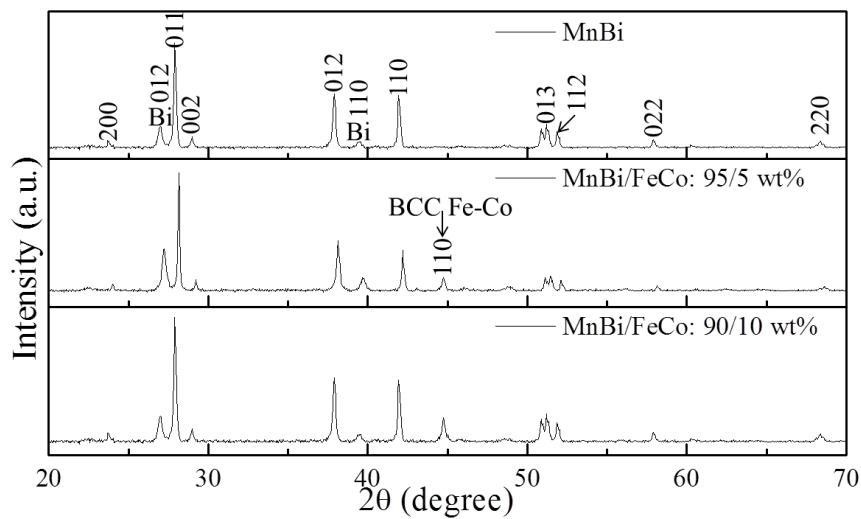


Figure 6.7 Powder XRD patterns of MnBi particles and MnBi/FeCo(95/5 wt% and 90/10 wt%) composites.

The morphology and elemental distributions of MnBi/FeCo (95/5 wt%) composites were investigated by both TEM and SEM. The SEM image of the composites is shown in Fig. 6.8a and detail of its surface condition is shown in the TEM image in Fig. 6.8b. The surface of MnBi is decorated with a layer (~20 nm) of FeCo nanoparticles. To show the core/shell structure more distinctly, the hard/soft boundary is marked with a white line. The decoration by FeCo nanoparticles is attributed to the magnetic attraction between FeCo and MnBi particles because the FeCo layer disappeared from the MnBi surface after the demagnetization of the MnBi/FeCo composites (not shown here, but similar to TEM images of demagnetized SrM/FeCo particles in Fig. 5.6). The SEM elemental mappings of Fig. 6.8a for Bi, Mn, Co, and Fe are shown in the Figs. 6.8c, d, e and f. It can be seen that FeCo are homogeneously mixed with MnBi, which contributes to the effective exchange coupling. The homogeneous mixing benefits from the hexane assisted grinding. When grinding MnBi together with the FeCo nanoparticles dispersed in hexane, the solvent gradually vaporized due to its low vapor pressure, and FeCo nanoparticles were magnetically attracted to the surface of MnBi particles forming the core/shell structure seen in Fig. 6.8b, preventing the self-agglomeration of FeCo nanoparticles.

These results show that the MnBi/FeCo composites with 5 wt% FeCo shows better exchange coupling effects than 10 wt%. It needs to be noted that the optimum amount of FeCo in MnBi/FeCo exchange coupled composites is determined by the size of MnBi. Smaller MnBi particles provide a bigger surface area to be exchange coupled with FeCo nanoparticles, therefore a larger amount of FeCo nanoparticles can be added with effective exchange coupling. However, the smaller size also leads to lower stability, making them easily oxidized with loss of magnetic properties. The single domain size of MnBi is ~500 nm with maximum coercivity of ~17 kOe [2].

The size of MnBi under our experimental conditions remains in microns, as shown in Fig. 6.8a, with coercivity of ~ 8 kOe to balance stability with magnetic properties.

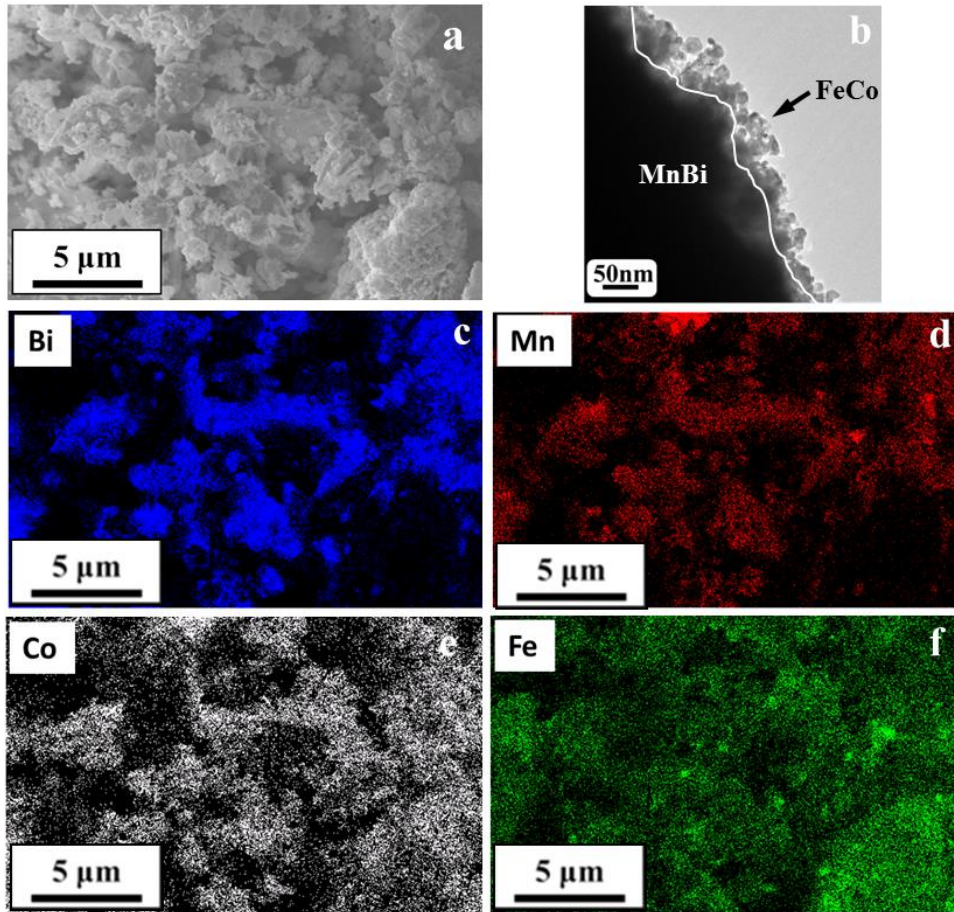


Figure 6.8 (a) SEM and (b) TEM images, and elemental mappings of (c) Bi, (d) Mn, (e) Co and (f) Fe for MnBi/FeCo (95/5 wt%) composites.

The virgin curves of MnBi particles and MnBi/FeCo (95/5 wt%) composites are shown in Fig. 6.9. It can be shown that the coercivity mechanism of both samples is nucleation effects [18], and the FeCo coating on MnBi particles does not change the coercivity mechanism.

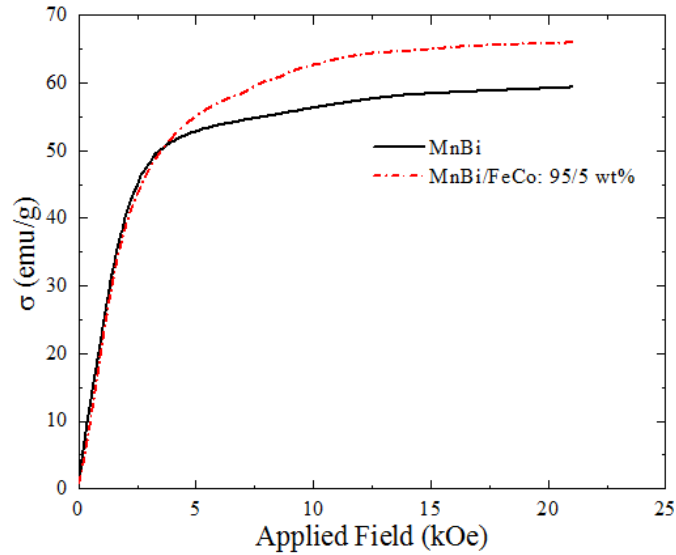


Figure 6.9 Virgin curves of MnBi particles and MnBi/FeCo (95/5 wt%) composites.

6.1.4. Conclusions

In summary, the synthesis and characterization of core/shell structured MnBi/FeCo composites are reported in this paper. The size of FeCo and MnBi is determined by oleic acid assisted wet chemistry synthesis and mechanical grinding process, respectively. The homogenous mixing of MnBi and FeCo is attributed to hexane dispersion of FeCo nanoparticles and magnetic attraction between MnBi and FeCo. It is found, based on the ΔM curves that the FeCo plays a key role in controlling the magnetic exchange coupling between the hard and soft particles.

6.2. Thermal Stability of MnBi/FeCo Composites

6.2.1. Introduction

Rare-earth-free exchange coupled hard/soft magnet has attracted lots of attention as an alternative for rare-earth permanent magnet [19-22]. The exchange coupled magnet requires the size of soft phase to be less than twice domain wall thickness of hard phase, usually no larger than 20 nm. It well known that the thermal stability of nanomaterials decreases dramatically from its bulk case. This brings new challenges to the exchange coupled hard/soft magnets, as

these exchange coupled magnets will be used inside electric motors, whose operating temperature can be as high as 200 °C [23].

The thermal stability of exchange coupled magnets, such as FePt/Fe were investigated and reported before [24,25]. However, the thermal stability of exchange coupled MnBi/FeCo composites has never been reported. In this part, the thermal stability of as-synthesized FeCo nanoparticles and exchange coupled MnBi/FeCo composites is investigated by annealing them in a N₂ environment. The morphology, magnetic properties and crystal phases of the annealed particles were characterized and compared with the particles before annealing.

6.2.2. Experimental

FeCo nanoparticles were synthesized with the method described in Chapter 4. MnBi/FeCo (m(FeCo)/m(MnBi)=5/95) composites were synthesized with the method discussed in Chapter 6.1. Both as-synthesized FeCo nanoparticles and MnBi/FeCo composites were annealed at 250 °C for 2 hours, and then cooled down to room temperature. To prevent the oxidation, the whole process was protected with N₂.

The measurement of X-ray diffraction (XRD) patterns was carried out by a Bruker D8 diffractometer using Cu-K α radiation ($\lambda= 1.54 \text{ \AA}$). TEM (TECNAI FEI 20) and SEM (JEOL 7000) were used to analyze the particle size and morphology. Magnetic properties were checked at room temperature with a VSM (Microsense 3473-70) in an applied field up to 2 T.

6.2.3. Results and discussion

Figures 6.10a and b show the morphology of as-synthesized and annealed FeCo particles. The as-synthesized FeCo nanoparticles are mono-dispersed, while the annealed ones are sintered and agglomerated. This could be attributed to the low thermal stability of FeCo nanoparticles,

and particles diffuse into each other at annealing temperature, and the mono-dispersion is destroyed.

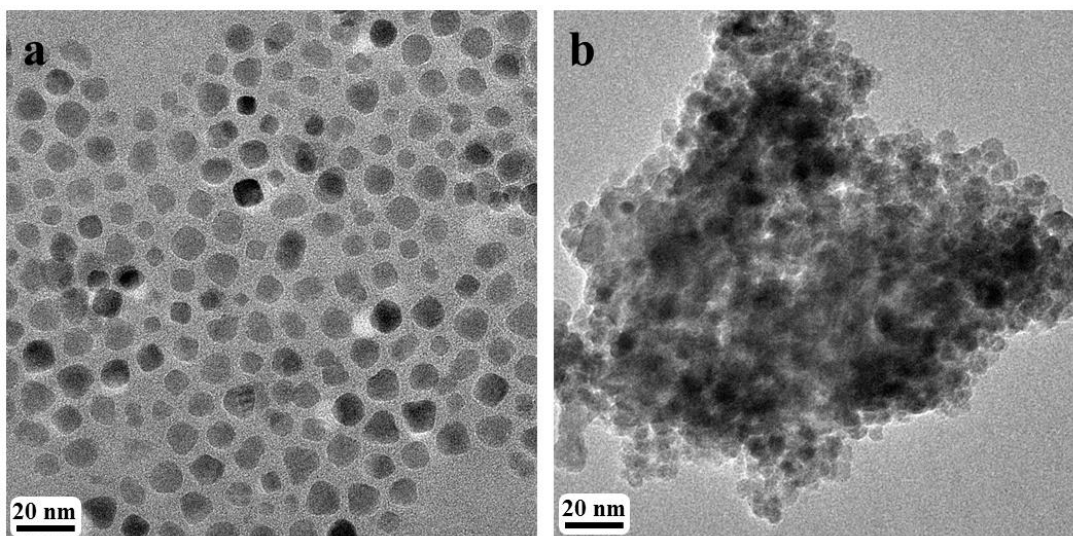


Figure 6.10 TEM images of FeCo nanoparticles: (a) As synthesized; (b) Annealed at 250 °C for 2 hours.

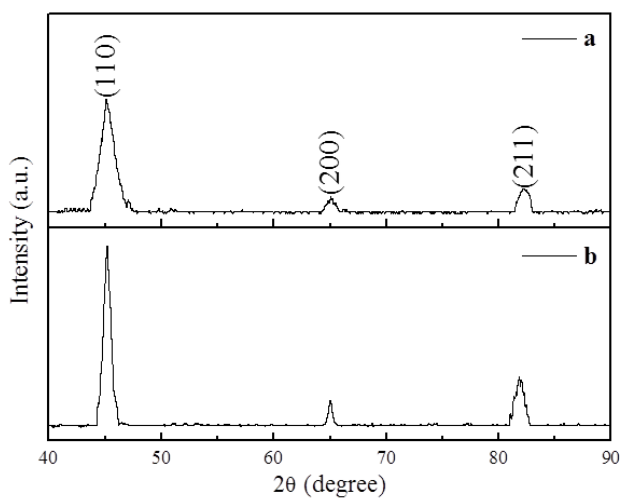


Figure 6.11 Powder XRD patterns of FeCo nanoparticles: (a) as synthesized; (b) annealed at 250 °C for 2 hours.

The powder XRD patterns of as-synthesized and annealed FeCo particles are shown in Fig. 6.11. After annealing, the XRD peak intensity increases and peak width decreases. The increased intensity could be attributed to particles' further crystallization during the annealing process. Ac-

According to Scherrer Equation, the decreased peak width indicates an increased particle size, which could be attributed to particle sintering during annealing. The mean crystallite size of the as-synthesized and annealed FeCo particles was calculated from Fig. 6.11 using the Scherrer Equation to be 11.2 nm and 83.6 nm, respectively.

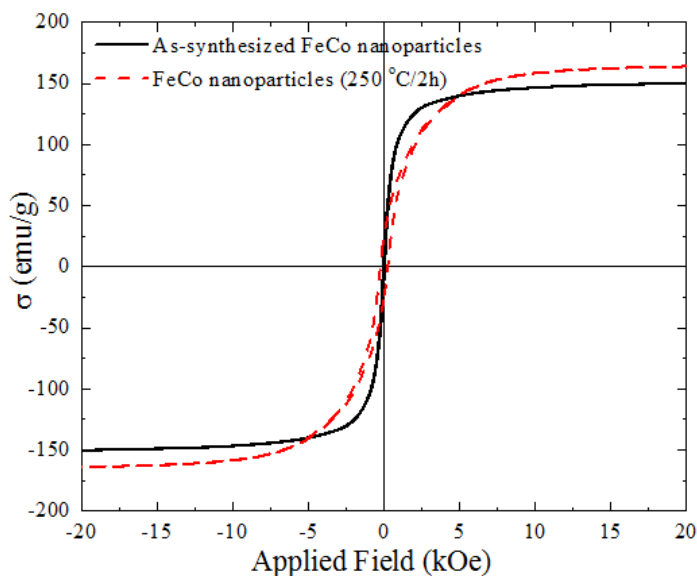


Figure 6.12 Magnetic hysteresis loops of FeCo nanoparticles: (a) as synthesized; (b) annealed at 250 °C for 2 hours.

The magnetic hysteresis loops of as-synthesized and annealed FeCo particles are shown in Fig. 6.12. It can be seen that after annealing, the magnetization is increased from 151 emu/g to 167 emu/g and the coercivity is increased from 41 Oe to 253 Oe. The increased magnetization could be attributed to better crystallization, as shown in Fig. 6.11, and the increased coercivity could be attributed to increased particles, as shown in Fig. 6.11.

TEM images of as-synthesized and annealed MnBi/FeCo (95/5 wt%) composites are shown in Fig. 6.13. MnBi surface is decorated with a thin layer of FeCo nanoparticles in as-synthesized MnBi/FeCo composites. However, after annealing, FeCo nanoparticles disappeared from MnBi surface, shown in Fig. 6.13c, or sintered on MnBi surface, shown in Fig. 6.13d, and the size of sintered FeCo nanoparticles is over 100 nm.

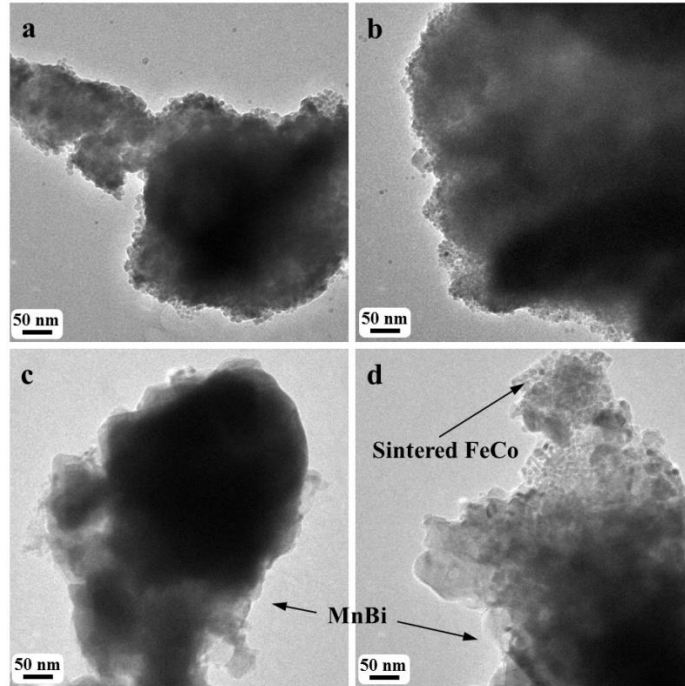


Figure 6.13 TEM images of MnBi/FeCo composites: (a) as synthesized; (b) annealed at 250 °C for 2 hours.

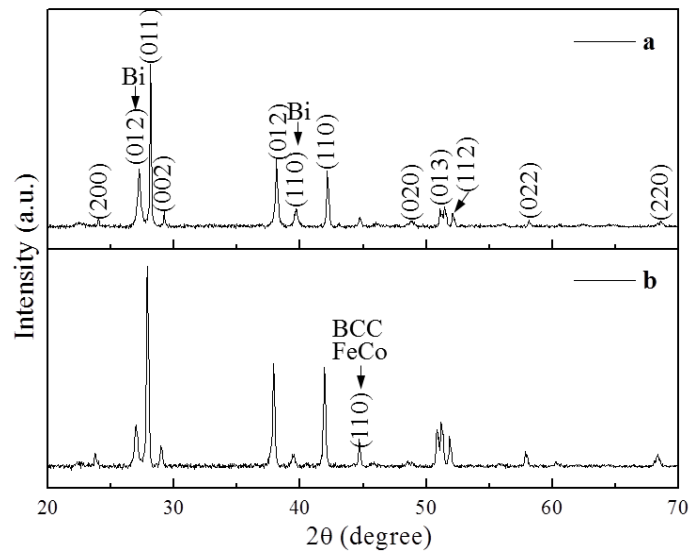


Figure 6.14 Powder XRD patterns of MnBi/FeCo composites: (a) as-synthesized; (b) annealed at 250 °C for 2 hours.

Powder XRD patterns of as-synthesized and annealed MnBi/FeCo (95/5 wt%) composites are shown in Fig. 6.14. It can be seen that there is little change in the MnBi peaks between as-synthesized and annealed composites, while the FeCo peak intensity increases after annealing.

The increased intensity could be attributed to better crystallization, which is consistent with XRD patterns of annealed FeCo nanoparticles in Fig. 6.11. The XRD patterns also indicate that the sintering and mass diffusion only happens among FeCo nanoparticles, and does not happen between FeCo and MnBi particles, nor among MnBi particles.

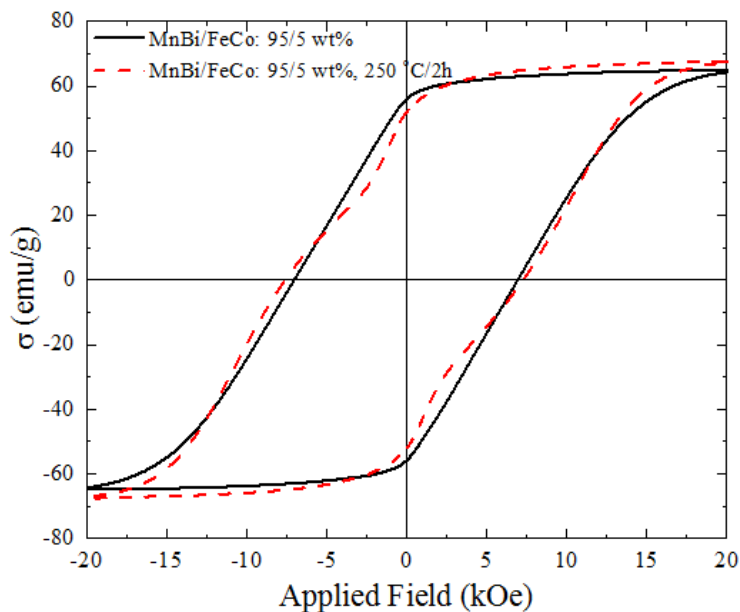


Figure 6.15 Magnetic hysteresis loops of MnBi/FeCo composites: (a) as-synthesized; (b) annealed at 250 °C for 2 hours.

The magnetic hysteresis loops of as-synthesized and annealed MnBi/FeCo (95/5 wt%) composites are shown in Fig. 6.15. The shape of as-synthesized MnBi/FeCo composites is smooth while there are obvious kinks in the annealed composites. These kinks indicate a weak or no exchange coupling between MnBi and FeCo particles. This result can be further explained by TEM image in Fig 6.13d that the FeCo nanoparticles are sintered after annealing to be more than 100 nm, far bigger than the critical size of soft phase (< 20 nm, twice domain wall thickness).

6.2.4. Conclusions

In summary, the synthesis and characterization of core/shell structured MnBi/FeCo composites are reported in this paper. The size of FeCo and MnBi is determined by oleic acid assisted

wet chemistry synthesis and mechanical grinding process, respectively. The homogenous mixing of MnBi and FeCo is attributed to hexane dispersion of FeCo nanoparticles and magnetic attraction between MnBi and FeCo. It is found, based on the ΔM curves that the FeCo plays a key role in controlling the magnetic exchange coupling between the particles.

6.3. References

1. Guo, X., Chen, X., Altounian, Z. & Stromolsen, J. O. Magnetic-Properties of Mnbi Prepared by Rapid Solidification. *Physical Review B*, **46**, 14578-14582 (1992).
2. Kang, K., Lewis, L. H. & Moodenbaugh, A. R. Alignment and Analyses of MnBi/Bi Nanostructures. *Applied Physics Letters*, **87** (2005).
3. Yang, J. B. *et al.* Anisotropic Nanocrystalline MnBi with High Coercivity at High Temperature. *Applied Physics Letters*, **99** (2011).
4. Yang, J. B. *et al.* Magnetic Properties of the Mnbi Intermetallic Compound. *Applied Physics Letters*, **79**, 1846-1848 (2001).
5. Cui, J. *et al.* Thermal Stability of MnBi Magnetic Materials. *Journal of Physics-Condensed Matter*, **26** (2014).
6. Skomski, R. & Coey, J. M. D. Giant Energy Product in Nanostructured 2-Phase Magnets. *Physical Review B*, **48**, 15812-15816 (1993).
7. Kneller, E. F. & Hawig, R. The Exchange-Spring Magnet - A New Material Principle for Permanent-Magnets. *IEEE Transactions on Magnetism*, **27**, 3588-3600 (1991).
8. Schrefl, T., Kronmuller, H. & Fidler, J. Exchange Hardening in Nano-Structured 2-Phase Permanent-Magnets. *Journal of Magnetism and Magnetic Materials*, **127**, L273-L277 (1993).
9. Poudyal, N., Rong, C., Nguyen, V. V. & Liu, J. P. Hard-Phase Engineering in Hard/Soft Nanocomposite Magnets. *Materials Research Express*, **1**, 016103 (2014).
10. Wang, D. P. *et al.* Exchange-Coupled Nanoscale SmCo/NdFeB Hybrid Magnets. *Journal of Magnetism and Magnetic Materials*, **324**, 2836-2839 (2012).
11. Cullity, B. D. & Graham, C. D. *Introduction to Magnetic Materials*. (Wiley, 2009).
12. Bondi, J., Oyler, K. D. & Schaak, R. E. Chemical Synthesis of Air-Stable Manganese Nanoparticles. *Abstracts of Papers of the American Chemical Society*, **238** (2009).
13. Patterson, A. L. The Scherrer Formula for X-ray Particle Size Determination. *Physical Review*, **56**, 978-982 (1939).
14. Dennis, C. L. *et al.* The Defining Length Scales of Mesomagnetism: A Review. *Journal of Physics-Condensed Matter*, **14**, R1175-R1262 (2002).

15. Wang, B. D., Wang, B. G., Wei, P. F., Wang, X. B. & Lou, W. J. Controlled Synthesis and Size-Dependent Thermal Conductivity of Fe₃O₄ Magnetic Nanofluids. *Dalton Transactions*, **41**, 896-899 (2012).
16. Ogrady, K., Elhilo, M. & Chantrell, R. W. The Characterization of Interaction Effects in Fine-Particle Systems. *IEEE Transactions on Magnetics*, **29**, 2608-2613 (1993).
17. Rong, C. B., Zhang, H. W., Shen, B. G. & Liu, J. P. Mechanism of the Anomalous Temperature Dependence of Coercivity in Sm(Co,Fe,Cu,Zr)(Z) High-Temperature Magnets. *Applied Physics Letters*, **88** (2006).
18. Suzuki, T. Coercivity Mechanism in (Co/Pt) and (Co/Pd) Multilayers. *Scripta Metallurgica Et Materialia*, **33**, 1609-1623 (1995).
19. Rai, B. K., Wang, L., Mishra, S. R., Nguyen, V. V. & Liu, J. P. Synthesis and Magnetic Properties of Hard-Soft SrFe₁₀Al₂O₁₉/NiZnFe₂O₄ Ferrite Nanocomposites. *Journal of Nanoscience and Nanotechnology*, **14**, 5272-5277 (2014).
20. Yu, Y. S. *et al.* One-Pot Synthesis of Urchin-Like FePd-Fe₃O₄ and Their Conversion into Exchange-Coupled L1(0)-FePd-Fe Nanocomposite Magnets. *Nano Letters*, **13**, 4975-4979 (2013).
21. Zeng, H., Li, J., Liu, J. P., Wang, Z. L. & Sun, S. H. Exchange-Coupled Nanocomposite Magnets by Nanoparticle Self-Assembly. *Nature*, **420**, 395-398 (2002).
22. Hoque, S. M. *et al.* Exchange-Spring Mechanism of Soft and Hard Ferrite Nanocomposites. *Materials Research Bulletin*, **48**, 2871-2877 (2013).
23. Lee, S. T., Kim, H. J., Cho, J. H., Joo, D. & Kim, D. K. Thermal Analysis of Interior Permanent-Magnet Synchronous Motor by Electromagnetic Field-Thermal Linked Analysis. *Journal of Electrical Engineering & Technology*, **7**, 905-910 (2012).
24. Guo, H. H. *et al.* Thermal Stability of FePt-Based Exchange Coupled Composite Films. *IEEE Transactions on Magnetics*, **49**, 3683-3686 (2013).
25. Florez, S. H. *et al.* Demonstration of the Thermal Stability Advantage of Advanced Exchange Coupled Composite Media. *Journal of Applied Physics*, **115** (2014).

CHAPTER 7 UNDERSTANDING OF EXCHANGE COUPLING

7. 1. Introduction

Since the discovery of exchange coupling in 1989 by Coehoorn and his coworkers from experiments on nanostructured Nd-Fe-B/Fe-B magnets[1], this magnetic phenomena has been extensively investigated on both magnetic particles and thin films [2-10]. There are many challenges to achieve exchange coupling between magnetically hard and soft materials, as it requires that both phases are well distributed with each other at the nano scale, and the dimension of soft phase is no larger than twice of domain wall thickness of the hard phase [11]. Therefore, it is necessary to use effective characterization methods to determine the existence of exchange coupling between hard and soft phases.

Several methods have been proposed to characterize the exchange coupling between magnetically hard and soft phases. The “kink” method is the simplest way to check the inter-phase exchange coupling between hard and soft magnetic phases. If the two phases are not exchange coupled, there will be a kink in the magnetic hysteresis loop, indicating decoupling between the two phases. However, this method cannot distinguish the magnetic hysteresis loops between single hard phase magnet and exchange coupled magnet. Low-temperature magnetic hysteresis loop measurement [12,13] is another method. When the temperature is lowered, the magnetocrystalline anisotropy of the hard magnet will be increased, and the exchange length will be decreased, which results in a decoupling between the hard and soft phases. Recoil loops are measured by removing and reapplying a demagnetizing field on a magnetic material. It is an important method to determine the exchange coupling in hard/soft magnets as recoil characteristics are sensitive to

inter-phase interactions. Open recoil loops will be observed if there is exchange coupling between hard and soft phases. Henkel plot (Delta M plot) can be used to determine the exchange coupling in a magnet. The positive values in the plot indicate magnetic exchange coupling, and the negative values indicate magnetic dipolar interactions. Element-specific measurements can also be used to characterize exchange coupling in hard/soft composites. In this technique, element-specific magnetic hysteresis loops can be obtained from the hard/soft composites, and the exchange coupling effects between thin film layers or particle phases can be speculated by correlating the results with a conventional hysteresis loop [14].

Among the above methods, the “kink” method is regarded as the simplest and most popular one to characterize the exchange coupling in hard/soft magnet because of its easy operation and low cost. The present work was conducted to better understand the phenomena of exchange coupling behaviors by using a kink method.

7. 2. Experimental

FeCo was synthesized based on a previous report [15], and the synthesis details were discussed in Chapter 4.

Synthesis of Composite A and Composite B: As-received MnBi particles (0.085 g, from PNNL) and as-synthesized FeCo nanoparticles (0.015 g) were introduced into a VSM sample holder and separated with a piece of paper between them. This sample is named as Composite A. As-received MnBi (0.085 g, from PNNL) particles and as-synthesized FeCo (0.015 g) particles were introduced to a mortar with hexane, gently ground for 10 min, and then dried to remove the residual hexane. This sample is named as Composite B. As a comparison, pure as-received MnBi was also ground in the same environment for 10 min.

7. 3. Results and discussion

The as-synthesized FeCo particles were characterized with VSM and TEM, and the corresponding results are shown in Fig. 7.1 The magnetization is 171 emu/g and the coercivity is 213 Oe, and the particle size ranges from 50 nm to 100 nm.

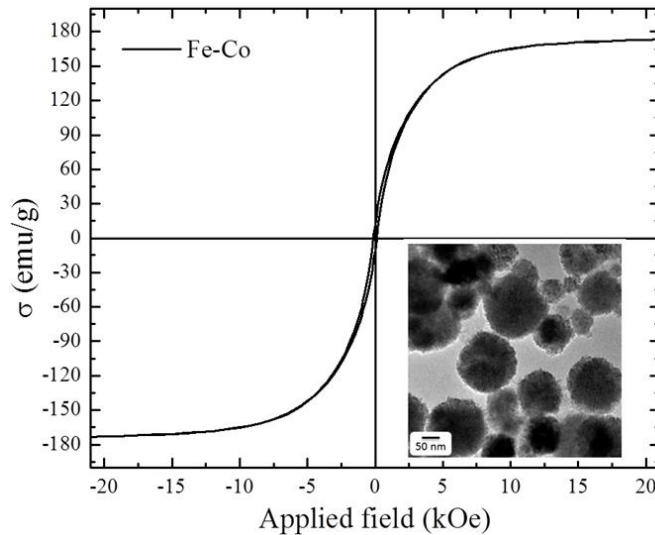


Figure 7.1 Magnetic hysteresis loop of as-synthesized FeCo particles. Inset: TEM image of FeCo particles.

The magnetic hysteresis loops of as-received MnBi particles, as-synthesized FeCo particles and Composite A are shown in Fig. 7.2. The VSM sample with Composite A is shown in the inset of Fig. 7.2. It can be seen that the magnetic hysteresis loop of Composite A is smooth. However, there can be no exchange coupling between MnBi and FeCo particles in Composite A, because: 1) the size of the FeCo particles is larger than the twice domain wall thickness of MnBi (~20 nm); 2) the distance between FeCo and MnBi (paper thickness) is larger than twice domain wall thickness of MnBi. Even though exchange coupling always leads to a smooth hysteresis loop, a smooth hysteresis loop is necessary but not sufficient to confirm the existence of exchange coupling in hard/soft composites.

The magnetic hysteresis loops of 10 min ground MnBi particles, as-synthesized FeCo particles and Composite B are shown in Fig. 7.3. The grinding process is applied to decrease the size of MnBi and achieve good mixing of MnBi and FeCo particles. There is an obvious kink in the magnetic hysteresis loop of Composite B, indicating a decoupling between MnBi and FeCo particles. This could be attributed to the large size of FeCo nanoparticles.

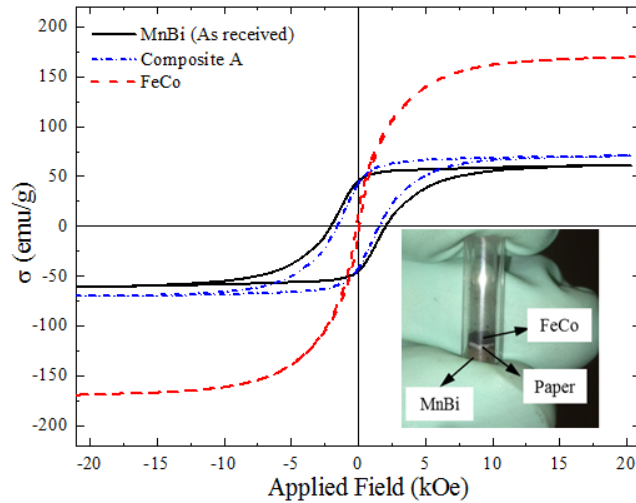


Figure 7.2 The magnetic hysteresis loop of MnBi particles, FeCo particles and Composite A. Inset: VSM sample of Composite A.

Exchange coupling exists in neither samples of Composite A nor Composite B. However, the magnetic hysteresis loop in Composite A is smooth, and there are obvious kinks in Composite B. Therefore, a smooth magnetic hysteresis loop of a hard/soft composites cannot indicate exchange coupling between hard and soft phases. Further investigation is needed to explore the reasons.

The derivative curves of magnetic hysteresis loops in Fig. 7.2 are shown in Fig. 7.4. The peak position indicates the coercivity of particles. Because the coercivities of MnBi (2012 Oe) and FeCo (213 Oe) are similar, their derivative curves overlap. This results in a very small kink in the derivative curve of Composite A hysteresis loop. The small kink in derivative curve makes the hysteresis loop look “smooth”.

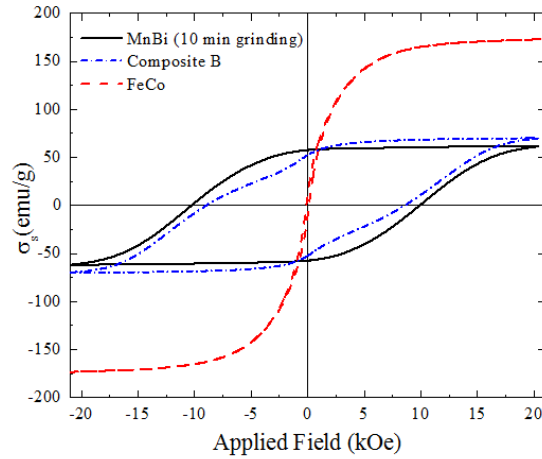


Figure 7.3 The magnetic hysteresis loop of MnBi particles, FeCo particles and Composite B.

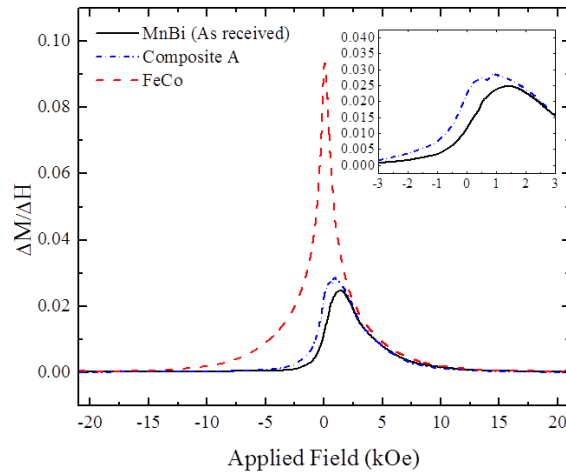


Figure 7.4 Derive curves of magnetic hysteresis loops in Fig. 7.2.

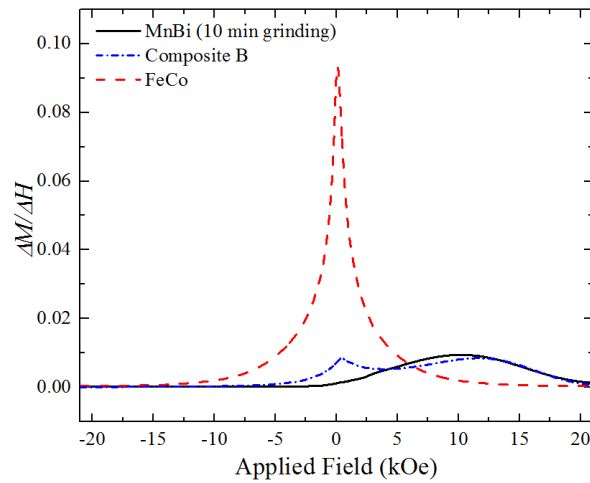


Figure 7.5 Derive curves of magnetic hysteresis loops in Fig. 7.3.

The derivative curves of magnetic hysteresis loops in Fig. 7.3 are shown in Fig. 7.5. Because of the large difference on the coercivity of MnBi (10053 Oe) and FeCo (213 Oe), their peaks in hysteresis loop derivative curves are far away from each other. This results in two obvious peaks in the derivative curves of Composite B hysteresis loop, and big kinks in its hysteresis loop.

7. 4. Conclusions

This report demonstrates that a smooth magnetic hysteresis loop of hard/soft composites is not sufficient to indicate exchange coupling between hard and soft phases. When the coercivities of hard and soft phases are similar, a smooth hysteresis loop of hard/soft composites can be obtained even though two phases are not exchange coupled with each other. The reasons are investigated through the derivative curves of hard phase, soft phase and hard/soft composite hysteresis loops.

7. 5. References

1. Coehoorn, R., Demooij, D. B. & Dewaard, C. Meltspun Permanent-Magnet Materials Containing Fe₃B as the Main Phase. *Journal of Magnetism and Magnetic Materials*, **80**, 101-104 (1989).
2. Skomski, R. & Coey, J. M. D. Exchange Coupling and Energy Product in Random 2-Phase Aligned Magnets. *IEEE Transactions on Magnetics*, **30**, 607-609 (1994).
3. O'Donnell, K. & Coey, J. M. D. Characterization of Hard Magnetic Two-Phase Mechanically Alloyed Sm₂Fe₁₇N₃/α-Fe Nanocomposites. *Journal of Applied Physics*, **81**, 6310-6321 (1997).
4. Yamazaki, Y. *et al.* Magnetic Properties of Sm-Co-Cu and Sm-Co-Cu/Co Exchange-Spring Films with High Coercivity. *Materials Transactions Jim*, **39**, 302-307 (1998).
5. Zeng, H., Li, J., Liu, J. P., Wang, Z. L. & Sun, S. H. Exchange-Coupled Nanocomposite Magnets by Nanoparticle Self-Assembly. *Nature*, **420**, 395-398 (2002).
6. Yan, A., Bollero, A., Gutfleisch, O. & Muller, K. H. Microstructure and Magnetic Properties of Two-Phase Exchange-Coupled SmCo₅/Sm₂(Co, M)₁₇ (M=Fe, Zr, Cu) Nanocomposites. *Journal of Physics D-Applied Physics*, **35**, 835-838 (2002).

7. Li, J., Wang, Z. L., Zeng, H., Sun, S. H. & Liu, J. P. Interface Structures in FePt/Fe₃Pt Hard-Soft Exchange-Coupled Magnetic Nanocomposites. *Applied Physics Letters*, **82**, 3743-3745 (2003).
8. Liu, J. P., Luo, C. P., Liu, Y. & Sellmyer, D. J. High Energy Products in Rapidly Annealed Nanoscale Fe/Pt Multilayers. *Applied Physics Letters*, **72**, 483-485 (1998).
9. Panagiotopoulos, I. & Hadjipanayis, G. C. Thin Film Nanocomposite Nd₂Fe₁₄B/ α -Fe Magnets. *Nanostructured Materials*, **10**, 1013-1022 (1998).
10. Zhang, J., Takahashi, Y. K., Gopalan, R. & Hono, K. Sm(Co,Cu)₅/Fe Exchange Spring Multilayer Films with High Energy Product. *Applied Physics Letters*, **86** (2005).
11. Skomski, R. & Coey, J. M. D. Giant Energy Product in Nanostructured 2-Phase Magnets. *Physical Review B*, **48**, 15812-15816 (1993).
12. Goll, D., Seeger, M. & Kronmuller, H. Magnetic and Microstructural Properties of Nanocrystalline Exchange Coupled PrFeB Permanent Magnets. *Journal of Magnetism and Magnetic Materials*, **185**, 49-60 (1998).
13. Yang, B., Shen, B. G., Zhao, T. Y., Zhang, H. W. & Sun, J. R. Nanocomposite Exchange-Coupled Magnets with Two Hard Phases PrCo₅C(Delta)/Pr₅Co₁₉C(Epsilon). *Journal of Physics D-Applied Physics*, **41** (2008).
14. Srajer, G. *et al.* Advances in Nanomagnetism Via X-Ray Techniques. *Journal of Magnetism and Magnetic Materials*, **307**, 1-31 (2006).
15. Sundar, R. S. & Deevi, S. C. Soft Magnetic FeCo Alloys: Alloy Development, Processing, and Properties. *International Materials Reviews*, **50**, 157-192 (2005).

CHAPTER 8 CONCLUSIONS AND FUTURE WORK

8. 1. Conclusions

Hollow spherical $\text{BaFe}_{12}\text{O}_{19}$ particles were synthesized by spray pyrolysis from different volume concentrations of EG in DI H_2O . Increasing EG concentration leads to bigger primary particle size and more broken particles. Also, the degree of crystallinity and coercivity increase, while the saturation magnetization decreases.

Hollow mesoporous spherical $\text{BaFe}_{12}\text{O}_{19}$ particles were synthesized by a template-free chemical etching process. The hollow particles are synthesized by spray pyrolysis. The mesoporous structure is obtained by exposing hollow $\text{BaFe}_{12}\text{O}_{19}$ spheres to alkaline EG at 185 °C. The porosity can be regulated by heating time, and the magnetic properties and crystal structure are little affected in the etching process. The mechanism is explained by grain boundary etching. The present method and mechanism may be also extended to synthesize a mesoporous structure of other metal ferrites.

Worm-shape $\text{BaFe}_{12}\text{O}_{19}$ is synthesized by a reverse microemulsion method and a post-annealing. Each single worm-shape particle is consisted of 3 to 7 small units. The formation mechanism is explained by a self-assembly process. The magnetization is lower than normal case because of containing $\alpha\text{-Fe}_2\text{O}_3$, which is confirmed by XRD patterns.

Monodispersed FeCo nanoparticles were synthesized by reducing FeCl_2 and CoCl_2 with n-butyllithium in diphenyl ether. The mono-dispersion is achieved by using oleic acid as surfactant. The crystal phases were confirmed by XRD, and the average size is 8.9 nm. The magnetization of FeCo nanoparticles is 151 emu/g and the coercivity is 41 Oe.

Core/shell structured SrFe₁₂O₁₉/FeCo nanoparticles were synthesized through a magnetic self-assembly process. By combining two materials in this way, the lattice mismatch that prevents epitaxial growth can be overcome, the size of hard phase and soft phase can be separately controlled and the mass diffusion between two phases does not happen. These core/shell-structured particles have significantly better magnetic properties because of exchange coupling, making them as excellent candidates for RE-free permanent magnets. The SiO₂ coating on SrFe₁₂O₁₉/FeCo core/shell nanoparticles is proven to be effective to protect the particles from oxidation. Within the range of magnetic attraction, the shell thickness of SrFe₁₂O₁₉/FeCo nanoparticles can be controlled by regulating the concentration of Fe and Co precursors. Magnetic exchange coupling between SrFe₁₂O₁₉ and FeCo nanoparticles is proven to be less effective in SrFe₁₂O₁₉/FeCo nanoparticle mixture than that in SrFe₁₂O₁₉/FeCo core/shell nanoparticles.

The synthesis and characterization of core/shell structured MnBi/FeCo composites are reported. The size of FeCo and MnBi is determined by oleic acid assisted wet chemistry synthesis and mechanical grinding process, respectively. The homogenous mixing of MnBi and FeCo is attributed to hexane dispersion of FeCo nanoparticles and magnetic attraction between MnBi and FeCo particles. The exchange coupling is confirmed by single-phase-like magnetic hysteresis loops and positive values in ΔM curves. The coercivity mechanism of MnBi particles and MnBi/FeCo composite is confirmed to be nucleation effects by magnetic virgin curve. The thermal stability of MnBi/FeCo composite was tested by annealing at 250 °C for 2 hours. The results show that the sintering of FeCo nanoparticles happens during the annealing, and the exchange coupling between MnBi and FeCo is destroyed after annealing.

8. 2. Future work

MnBi is more promising than SrFe₁₂O₁₉ as a RE-free permanent magnet, because of its high magnetocrystalline anisotropy ($1.6 \times 10^6 \text{ J/m}^3$ at 300 K) [1], large coercivity (1.7 T at 300 K) [2] and positive temperature coefficient of coercivity (between 150 and 550 K) [3]. The energy product of MnBi can be further increased by exchange coupling with FeCo nanoparticles. However, there are still many challenges remaining for the synthesis and application of exchange coupled MnBi/FeCo composite:

1. Chemical synthesis of MnBi particles: Currently, all reported MnBi synthesis methods are physical methods, and these methods are complex, mostly starting from arc melting, followed by grinding, sieving, annealing and reducing [1,4-6]. Furthermore, the morphology and size of MnBi particles are hard to be controlled in physical methods. Chemical synthesis is easier to operate and more effective to control the size and morphology of MnBi particles. However, chemical synthesis of MnBi is never reported because of large reduction potential difference between Mn²⁺ and Bi³⁺, as well as the oxophilicity of Mn [7]. Nikles' group [8] tried to synthesize MnBi particles with wet chemistry method, but the magnetic properties of the products are not good. A more reliable and effective wet chemistry method for MnBi synthesis needs to be explored in the further research.

2. Decrease the particle size of MnBi particles and maintain their stability: The single domain size of MnBi is around 500 nm, with coercivity of 1.7 T. The size of MnBi in this research is $\sim 5 \mu\text{m}$ with the coercivity of $\sim 1\text{T}$. Size of MnBi particles can be further reduced to increase the coercivity, as well as surface area, so that a larger amount of FeCo nanoparticles can be attached to the surface. However, the smaller size also leads to lower stability, making them easily oxidized with loss of magnetic properties. To further increase the energy product of MnBi/FeCo

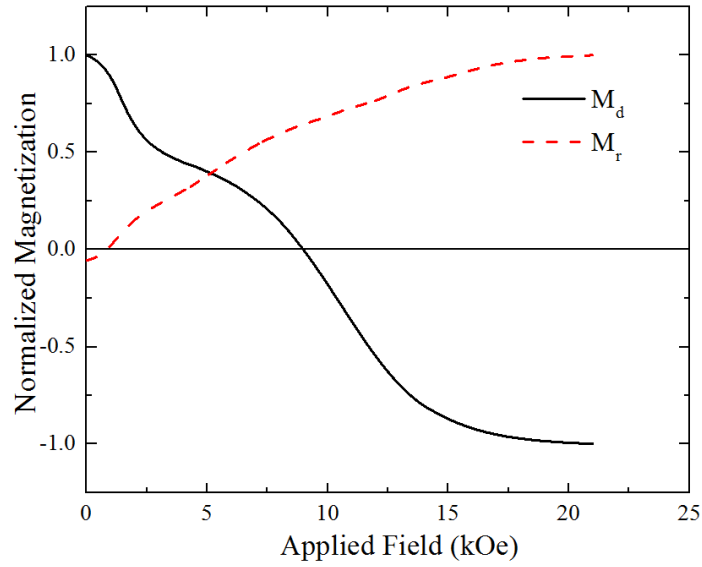
composites, it is necessary to explore new methods to further decrease the size MnBi particles to single domain size and at the same time maintain their stability in the future research.

3. Improve the thermal stability of MnBi/FeCo composites: Current research shows that exchange coupled MnBi/FeCo composites has low thermal stability due to sintering of FeCo nanoparticles at high temperature. As a RE-free permanent magnet potentially used in electrical motors, it should show long-term thermal stability at temperature of ~200 °C. Therefore, further research should solve this problem.

8. 3. References

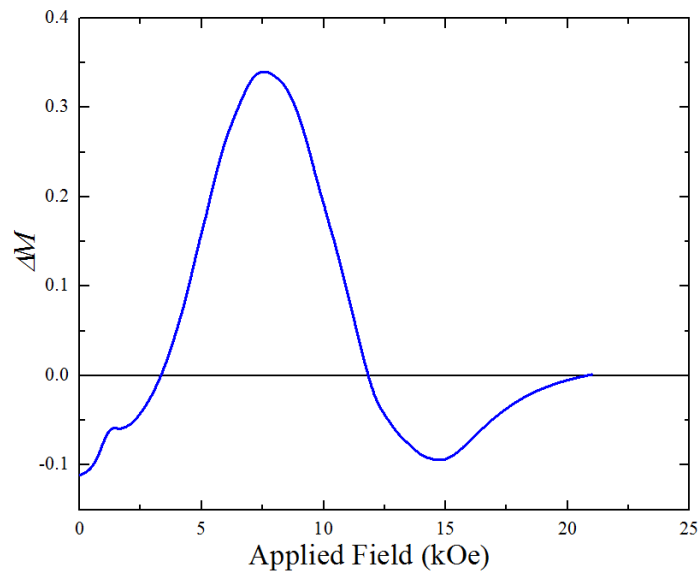
1. Guo, X., Chen, X., Altounian, Z. & Stromolsen, J. O. Magnetic-Properties of MnBi Prepared by Rapid Solidification. *Physical Review B*, **46**, 14578-14582 (1992).
2. Kang, K., Lewis, L. H. & Moodenbaugh, A. R. Alignment and Analyses of MnBi/Bi Nanostructures. *Applied Physics Letters*, **87** (2005).
3. Yang, J. B. *et al.* Anisotropic Nanocrystalline MnBi with High Coercivity at High Temperature. *Applied Physics Letters*, **99** (2011).
4. Yang, J. B. *et al.* Crystal Structure, Magnetic Properties and Electronic Structure of the MnBi Intermetallic Compound. *Journal of Physics-Condensed Matter*, **14**, 6509-6519 (2002).
5. Kharel, P., Shah, V. R., Skomski, R., Shield, J. E. & Sellmyer, D. J. Magnetism of MnBi-Based Nanomaterials. *IEEE Transactions on Magnetics*, **49**, 3318-3321 (2013).
6. Cui, J. *et al.* Thermal Stability of MnBi Magnetic Materials. *Journal of Physics-Condensed Matter*, **26** (2014).
7. Bondi, J., Oyler, K. D. & Schaak, R. E. Chemical Synthesis of Air-Stable Manganese Nanoparticles. *Abstracts of Papers of the American Chemical Society*, **238** (2009).
8. Zhang, L. On the Chemical Synthesis of Manganese-based High Magnetocrystalline Anisotropy Energy Density Magnetic Nanoparticles. Ph.D. Dissertation, the University of Alabama, 2013.

APPENDIX I: ΔM Calculation



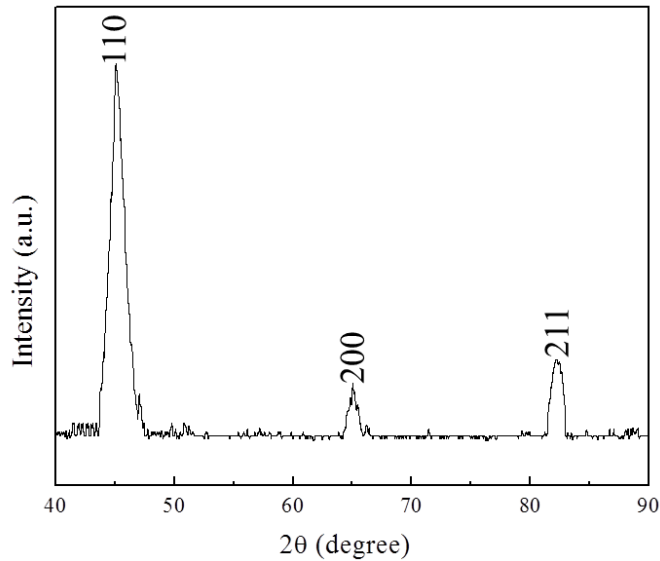
Appendix Figure 1. Normalized demagnetization remanence (M_d) and isothermal magnetization remanence (M_r) curves of MnBi/FeCo: 95/5 wt% composites.

$$\Delta M = M_d(H) - [1 - 2M_r(H)]$$



Appendix Figure 2. ΔM curve of of MnBi/FeCo: 95/5 wt% composites.

APPENDIX II: The Composition of FeCo Nanoparticles



Appendix Figure 3. Power XRD patterns of Fe-Co nanoparticles in Fig. 4.3.

The error of XRD data can be larger at a larger θ angle. To make the results more accurate and reliable, the lattice constant (a) calculation in this part will be based on the peaks of (110) and (200).

$$2\theta (110) = 45.0^\circ \qquad 2\theta (200) = 65.0^\circ$$

$$\theta(110) = 22.5^\circ \qquad \theta (200) = 32.5^\circ$$

$$d = \lambda/2\sin\theta$$

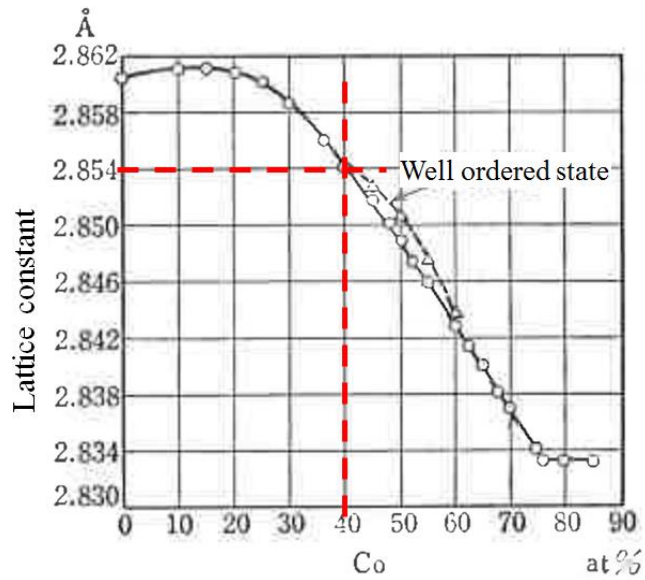
$$\lambda = 0.154 \text{ nm (Cu K}\alpha \text{ radiation)}$$

$$d (110) = 2.01 \text{ \AA} \qquad d (200) = 1.433 \text{ \AA}$$

$$a = d\sqrt{h^2 + k^2 + l^2}$$

$$a (110) = 2.842 \text{ \AA} \qquad a (200) = 2.866 \text{ \AA}$$

$$\tilde{a} = 2.854 \text{ \AA}$$



Appendix Figure 4. Fe-Co ally lattice constant [1].

Based on above graph, when lattice constant $a = 2.854 \text{ \AA}$, the atomic percentage of Co in Fe-Co alloy is 40%. Considering the errors in the measuring and calculating processes, the real atomic percentage of Co in Fe-Co alloy could be $40\% \pm 10\%$.

[1] Bozorth, R. M. *Ferromagnetism*. (Van Nostrand-Reinhold, New York, 1951), P192.

APPENDIX III: The Prediction of the Size of Superparamagnetic FeCo Nanoparticles

$$r_0^{1\text{year}} \approx \left(\frac{10\kappa_B T}{K_u} \right)^{1/3}$$

$r_0^{1\text{year}}$: superparamagnetic particle radius T: temperature

κ_B : boltzmann constant

K_u : anisotropy constant

$\kappa_B = 1.38 \times 10^{-16}$ erg/K

$K_u(\text{FeCo}) = 5 \times 10^5$ erg/cc

T = 300 K

$\rightarrow r_0^{1\text{year}} \approx 9.4$ nm

$d_0 = 18.8$ nm

APPENDIX IV: The Prediction of the Size of Superparamagnetic SrFe₁₂O₁₉ and BaFe₁₂O₁₉ Nanoparticles

$$r_0^{1\text{ year}} \approx \left(\frac{10\kappa_B T}{K_u} \right)^{1/3}$$

$r_0^{1\text{ year}}$: superparamagnetic particle radius T: temperature

κ_B : boltzmann constant

K_u : anisotropy constant

$\kappa_B = 1.38 \times 10^{-16}$ erg/K

K_u (SrFe₁₂O₁₉) = 3.5 x 10⁶erg/cc

K_u (BaFe₁₂O₁₉) = 3.3 x 10⁶erg/cc

T = 300 K

$\rightarrow r_0^{1\text{ year}}$ (SrFe₁₂O₁₉) \approx 4.9 nm

d_0 (SrFe₁₂O₁₉) = 9.8 nm

$\rightarrow r_0^{1\text{ year}}$ (BaFe₁₂O₁₉) \approx 5.0 nm

d_0 (BaFe₁₂O₁₉) = 10.0 nm

APPENDIX V: The Repeatability of Experiments

The synthesis of hollow mesoporous $\text{BaFe}_{12}\text{O}_{19}$ spheres (Chapter 3.1), hollow $\text{BaFe}_{12}\text{O}_{19}$ spheres (Chapter 3.2), FeCo nanoparticles (Chapter 4.1), $\text{SrFe}_{12}\text{O}_{19}/\text{FeCo}$ core/shell particles (Chapter 5) and MnBi/FeCo (Chapter 6) composites has a high repeatability. The morphology of these products can be well repeated. Due to the experiment conditions (temperature control, washing process, glove box environments and etc.) control, VSM and analytical balance errors, the magnetization and coercivity change within 10% in different batches.

The synthesis of worm-shape $\text{BaFe}_{12}\text{O}_{19}$ nanoparticles was only achieved once, and the results are shown in Chapter 3.3. The results were never repeated after tens of times trials. The details are well recorded in Chapter 3.3, and dissertation readers may find ideas to repeat the results after reading the experiment details.

APPENDIX VI: List of Publications and Patents

Journal Papers

1. **X. Xu**, J. Park, Y. K. Hong, A. M. Lane. Synthesis and Characterization of Hollow Mesoporous BaFe₁₂O₁₉ Spheres, *J. Solid. State. Chem.*, 222, 84-89 (2015).
2. **X. Xu**, J. Park, Y. K. Hong, A. M. Lane. Magnetically Self-assembled SrFe₁₂O₁₉/FeCo Core/shell Nanoparticles, *Mater. Chem. Phys.*, 152, 9-12 (2015).
3. **X. Xu**, J. Park, Y. K. Hong, A. M. Lane. Ethylene Glycol Assisted Spray Pyrolysis for the Synthesis of Hollow BaFe₁₂O₁₉ Spheres, *Mater. Lett.*, 144, 119-122 (2015).
4. **X. Xu**, Y. K. Hong, J. Park, A. M. Lane. Exchange Coupled SrFe₁₂O₁₉/FeCo Core/shell Composites with Different Shell Thickness, *Electro. Mater. Lett.*, accepted, (2015).
5. **X. Xu**, Y. K. Hong, J. Park, A. M. Lane. Magnetic Self-Assembly for the Synthesis of Magnetic Exchange Coupled MnBi/Fe-Co Composites, *J. Solid. State. Chem.*, in revision, (2015)
6. **X. Xu**, Y. K. Hong, J. Park, A. M. Lane. Thermal Stability of FeCo Nanoparticles and Exchange Coupled MnBi/FeCo Composites, *Mater. Lett.*, in preparation, (2015).
7. **X. Xu**, Y. K. Hong, J. Park, A. M. Lane. Derivative Curve Analysis of Magnetic Hysteresis Loops for Hard/soft Magnetic Composites, *Electro. Mater. Lett.*, in preparation, (2015).
8. **X. Xu**, Y. K. Hong, J. Park, A. M. Lane. Monodispersed FeCo Nanoparticles from n-Butyllithium reduction, in preparation, (2015).
9. **X. Xu**, A. M. Lane. Water-treated Rh/ γ -Al₂O₃ Catalyst for Methane Partial Oxidation, in preparation, (2015)
10. Y. Luo, D. Zhang, **X. Xu**. Precise Cutting Micro Grooved Super-hydrophobic Surface, *Surf. Eng*, accepted, (2015)
11. J. Park, Y. K. Hong, J. Lee, W. Lee, **X. Xu**, A. M. Lane. Magnetization and intrinsic coercivity for τ -phase Mn₅₄Al₄₆/ α -phase Fe₆₅Co₃₅ composite, *J. Mag.* 19, 55 (2014).
12. Y. Luo, **X. Xu**, D. Li, S. Wen. Recent Developments of Fabricating Drag Reduction Surfaces Covering Biological Sharkskin Morphology, *Rev. Chem. Eng*, under review (2015)

Patents (Provisional)

1. Y. K. Hong, **X. Xu**, J. Park, A. M. Lane. Manufacturing Method for Hard Magnetic Metal/Soft Magnetic Metal Alloy Composite (Exchange Coupled) Magnets. UAIPD14-0041, (2014).
2. Y. K. Hong, **X. Xu**, A. M. Lane, J. Park. Remanent Magnetization Assisted Self-assembled Core-shell Magnets for Magnetic Exchange Coupling. UAIPD14-0002, (2013).